A Multi-Step Self-Assembly Route to Three-Dimensional Block Copolymer-Semiconducting Nanoparticle Photonic Arrays with Structural Hierarchy

By

Huda Yusuf
B.Sc., University of Ottawa, 2003

A Thesis Submitted in Partial Fulfillment of the
Requirements for the Degree of

MASTER of SCIENCE

in the Department of Chemistry

A Multi-Step Self-Assembly Route to Three Dimensional Block Copolymer-Semiconducting Nanoparticle Photonic Arrays with Structural Hierarchy

By

Huda Yusuf
M. Sc. University of Victoria, 2006

Supervisory Committee

Dr. M. G. Moffitt, (Department of Chemistry)

Supervisor

Dr. F. van Veggel, (Department of Chemistry)

Departmental Member

Dr. A. Brolo, (Department of Chemistry)

Departmental Member

Supervisory Committee

Dr. M. G. Moffitt, (Department of Chemistry)

Supervisor

Dr. F. van Veggel, (Department of Chemistry)

Departmental Member

Dr. A. Brolo, (Department of Chemistry)

Departmental Member

ABSTRACT

A new multi-step self-assembly route to polymer-semiconducting nanoparticle photonic structures is described. The multi-step self-assembly strategy targets complex hierarchical structures in which organization of cadmium sulfide (CdS) nanoparticles on progressively longer length scales is introduced via a series of three self-assembly steps, each involving building blocks of increasing structural complexity. Each self-assembly step can be described as follows: 1) SA1: self-assembly of PS-*b*-PAA to form block ionomer reverse micelles, followed by synthesis of a single CdS semiconducting nanoparticle in each core, forming the hybrid building blocks PS-CdS; 2) SA2: self-assembly of blends of PS-CdS and PS-*b*-PAA stabilizing chains in DMF/water mixtures by addition of water to form spherical nanoparticle assemblies, termed large compound micelles (LCMs); 3) SA3: self-assembly of LCMs into ordered close packed arrays by slow water evaporation. The kinetic freezing of building blocks at each stage offers the potential for unique control of nanoparticle self-assembly step since each step is "locked in", allowing structural features determined by the subsequent step to be independently tuned through a new set of experimental variables. Chapter 2 and 3 of this thesis investigate aspects of size and polydispersity control of spherical nanoparticle assemblies in the SA2 self-assembly step. Chapter 4 demonstrates that LCMs can be further assembled (SA3 step) to form three-dimensional hierarchical arrays.

Acknowledgements

First, I would like to thank God for his blessings and guidance in every aspect of my life.

I would like to take this opportunity to thank my supervisor, Dr. Matt Moffitt, for his guidance and direction in every step of this work. To my group members, past and present, thanks for giving me help whenever the time called for it. I would also like to thank the Department of Chemistry for all their help in the past few years.

To my dear family, I want to thank you for being there for me and being the most understanding and loving family any scientist can ever dream of. To my husband, thank you for giving me the support that I needed when the going got tough and for your unconditional love.

To my friends, near and far, I want you to know that your support does not go unnoticed and especially to my friends in Victoria: thank you for making me feel like I'm home in this city. Special thank you to Tamara Pace, you truly are a wonderful friend.

Finally, a big thank you to Brent Gowen for all his support.

Table of Contents

List of Schemes and Figures

List of Tables

CHAPTER 1

General Introduction

1.1. General Introduction

In this day and age, new materials are required to satisfy the need for computer data storage and information transfer which has created a field of research studying the possibilities of tuning material properties at the nano-scale. Specifically, metallic and semiconducting nanoparticles (NP), which show quantum confinement and surface effects, offer appealing size-tunable properties (e.g. photoluminescence, non-linear optical properties, surface plasmon resonances) that make them candidates for structural elements in photonic devices. However, if one wants to apply nanoparticles as "building blocks" in real device applications, it is of importance to establish control of nanoparticle (NP) organization on multiple length scales[1-4], since the collective optical properties of self-assembled materials will be dependent on effects operating on different length scales. For example, dipole-dipole interactions between semiconducting nanoparticles are operative for interparticle spacings less than ~ 10 nm[5], and can result in enhanced optical nonlinearities and an overall red-shift in absorption and fluorescence spectra relative to dilute solutions of independent nanoparticles (NPs). Control of interparticle spacing within nanoparticle (NP) assemblies is therefore a critical issue for certain potential applications.

A different optical effect that has been demonstrated within nanoparticles in certain assemblies is operative on much longer length scales, on the order of optical wavelengths--the so called photonic band gap effect. This effect is due to a modulation of the refractive index with a period on the order of hundreds of nanometers. The most prominent feature of such structures is that they present iridescence as a result of the diffraction of light. Photonic bandgap (PBG) crystals have periodic dielectric structures

with periodicities comparable to the wavelength of light, resulting in a stop-band for specific frequencies and wave vectors in which the photonic density of states is reduced. A PBG material is therefore a powerful way to control, imprison, and manipulate photons in all three dimensions of space: for example, by blocking the spread of photons, by localizing photons to a specific area at limited frequencies, and by serving as a lossless waveguide to direct the propagation of photons along a specific direction[6]. PBG crystals containing non-linear optical and light-emitting materials such as semiconducting NPs have been studied with a view to photonic devices based on the interactions between a periodic dielectric medium and the optical properties of an active dopant[6, 7].

This thesis describes a new and innovative approach to the multi-scale ordering of inorganic nanoparticles (quantum dots) for the synthesis of photonic materials with specific optical properties. The innovation of this approach lies in the use of stable polymer-brush coated nanoparticles as "hybrid building blocks" to produce hierarchical structures via a three-step self-assembly route. Unlike existing routes to ordered nanoparticle assemblies, in which various mechanisms of self-assembly are used to form complex structures in a single step, this thesis proposes three separate self-assembly steps to impart order on progressively longer length scales, allowing unprecedented control of ordering on each length scale.

The introductory chapter will be divided as follows: first a general description of polymers and anionic polymerization will be given. Then the micellization of diblock copolymers in selective solvents, amphiphilic diblock copolymers in aqueous solutions, and ionic diblock copolymers in organic solvents will be described. Next semiconducting nanoparticles and the quantum confinement effect will be discussed,

followed by a description of various strategies for nanoparticles self-assembly. Finally, specific targets of this thesis will be outlined in detail.

1.2. Polymers and Anionic Polymerization

1.2.1. Polymers:

A polymer is a large molecule built up from many smaller molecules. Polymers are formed by a process known as polymerization in which monomer molecules are linked together through a chemical reaction. The types of polymers vary depending on their structure: there are linear, branched and network polymers. Linear polymers, as the name implies, have a skeletal structure that is linear. A branched polymer's skeleton has side chains, or branches, which are bonded to the main chain at branch points, also known as junction points. They are characterized by the number and size of the branches. Finally, network polymers have three-dimensional structures where chains are interconnected via many junction points. These can also be called crosslinked polymers and they are characterized by their crosslink density, or degree of crosslinking, which describes the number of junction points per unit volume[8-10].

Polymers can also be defined by the number of types of monomers that are used. If only a single type of monomer is polymerized, the resulting polymer is called a homopolymer. If two or more monomers are used, the polymer is called a copolymer. Copolymers can be divided into four main categories: statistical copolymers, alternating copolymers, block copolymers and graft copolymers, depending on how the polymerized monomers, or repeat units are distributed along the chain. Statistical copolymers are also called random copolymers, as the distribution of the repeat units along the chain is

random. Alternating copolymers have only two different types of repeat units and these are arranged in an alternating fashion. Block copolymers are linear copolymers in which repeat units of one type exist in long sequences or blocks covalently connected to blocks of another type of repeat unit. Finally, graft copolymers are branched copolymers that consist of blocks of one type of repeat unit grafted onto a backbone of another type of repeat unit[8-10].

AAABABAABBAABABBBAAAABBABABA Random Copolymers

ABABABABABABABABABABABABABA Alternate Copolymers

AAAAAAAAAAAAAAABBBBBBBBBBBB Block Copolymers

B
B
B
B
AAAAAAAAAAAAAAAAAAAAAAAAA Graft Copolymers

The size of a polymer chain is a very important factor in determining the properties of the polymer sample. Unlike many small molecules, polymers do not have a discrete molecular mass, but rather a distribution of sizes that arise from the different chain lengths that make up the polymer sample[8]. The size of a polymer is characterized by its average molar mass *(M)* (units of g $mole^{-1}$)[10]. The average molar mass of a homopolymer is related to its average degree of polymerization, x, which is the average number of repeat units in a polymer chain. This relationship is shown as:

$$M = xM_0 \qquad (1)$$

where M_0 is the molar mass of the repeat unit.

There are two common averages generally used to report the average molar mass of a polymer[8]. These values differ in the way that they average the distribution of polymer chains: M_n, which is called the number-average molar mass, is sensitive to the number of each species present and is defined by the following equation:

$$M_n = \frac{\sum N_i M_i}{\sum N_i} \qquad (2)$$

where N_i is the number of molecules of species i of molar mass M_i. This value is often obtained using colligative methods, such as osmotic pressure, which count the number of molecular species in solution[8].

The other average value used to report the molar mass of the polymer is sensitive to the sizes of the various species in the distribution and is generally measured via light scattering techniques: M_w, which is the weight-average molar mass is defined by the following equation:

$$M_w = \frac{\sum W_i M_i}{\sum W_i} = \frac{\sum N_i M_i^2}{\sum N_i M_i} \qquad (3)$$

where W_i is the weight of all molecules of species i with molar mass M_i[8]. These two averages are used hand in hand to determine information on the distribution of molar mass.

To characterize the width of the molar mass distribution for a polymer sample, the ratio of the weight-average molar weight *(M_w)* and the number-average molar mass *(M_n)* is taken. This ratio is known as the polydispersity index, P.I., where a monodisperse sample is characterized by P.I. = 1[8]:

$$\text{P.I.} = \frac{M_w}{M_n} \qquad (4)$$

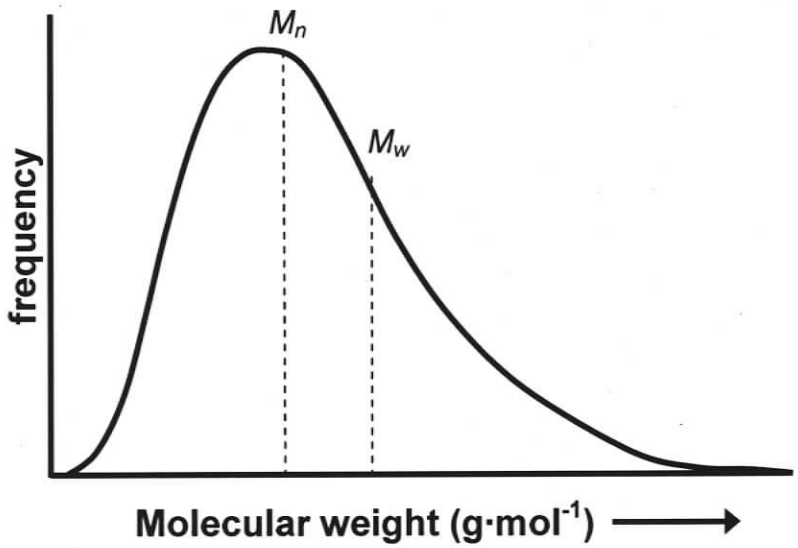

Figure 1.1. Molar mass distribution of a theoretical polymer sample highlighting the positions of the defined average molar mass.

1.2.2. Anionic Polymerization

There are different ways of classifying methods for forming polymers. In condensation polymerization, the resulting polymers have repeat units with a lower molar mass than the starting monomers, indicating that a small molecule or molecules are

released in the polymerization reaction. In contrast, addition polymerization polymers have repeat units with the same molar mass as the starting monomer. A different, but related, classification scheme is based on the polymerization mechanism and is divided into step-growth polymerization and chain-growth polymerization. In step-growth polymerization, the polymer grows in a step-wise manner by reactions that occur between any two molecular species in the reaction mixture. For chain-growth polymerization, a polymer chain can only grow by reaction of a monomer with a reactive end-group on the growing chain[8-10].

One example of a chain-growth polymerization reaction is free radical polymerization. In free radical polymerization, the reactive end-group of growing chains, or active center, possesses an unpaired electron that reacts with an olefinic monomer and regenerates a free radical in a chain reaction[8]. Therefore, once the active center is produced a kinetic chain is propagated which can only be stopped via a termination reaction, where the radical is no longer active. This can be done in several ways: (1) the interaction of two active chain ends; (2) the reaction of an active chain end with an initiator radical; (3) termination by transfer of the active center to another molecule which may be solvent, initiator, or monomer; (4) interaction with impurities or inhibitors[8].

The type of polymerization used in this study was anionic polymerization, which is another type of chain-growth polymerization. The active centre in anionic polymerization is a carbanion, unlike the active centre in free radical polymerization which is a radical. This is a living polymerization reaction, meaning that the polymer molecules retain their active centers and can polymerize until the reaction is terminated

by adding an agent such as methanol to stop the polymerization. This is possible because, unlike free radical polymerization, anionic polymerization lacks the presence of an intrinsic termination step. Termination by ion-pair rearrangement does not occur because it requires the highly unfavorable elimination of a hydride ion. In addition, the alkali metal (or alkaline earth metal) counter-ions used have no tendency to combine with the carbanionic active centers to form unreactive covalent bonds. Anionic polymerization is a technique used to synthesize block copolymers because the molar mass distributions of the block copolymers are usually narrow, and sequential addition of monomers to the living chains allows control over the molar mass and relative lengths of the various blocks[11].

Before any further discussion on the self-assembly of block copolymers, the anionic polymerization of the type of block copolymers used in this thesis, polystyrene-*b*-poly(*tert*-butylacrylate) (PS-*b*-PtBA), will be outlined. Impurities such as water and oxygen are extremely detrimental to anionic polymerization because they kill the reaction via termination reaction with carbanion living chains, which causes unwanted homopolymers to be present in the system. To eliminate this inherent difficulty, the synthesis was performed using rigorous Schlenk line techniques under nitrogen atmosphere and vacuum.

The anionic polymerization of PS-*b*-PtBA is carried out using tetrahydrofuran (THF) as a solvent, with α-methylstyrene and LiCl, which is used as a capping agent for the living chains[11-13]. To initiate the reaction, *sec*-butyllithium (*sec*-BuLi) is added to a solution of α-methylstyrene and LiCl in THF at room temperature until a red colour is achieved. The sec-BuLi first eliminates any impurities such as water from the mixture

and then it activates the α-methylstyrene to produce short polycarbanions, **1**, of a deep red colour (Scheme 1.1).

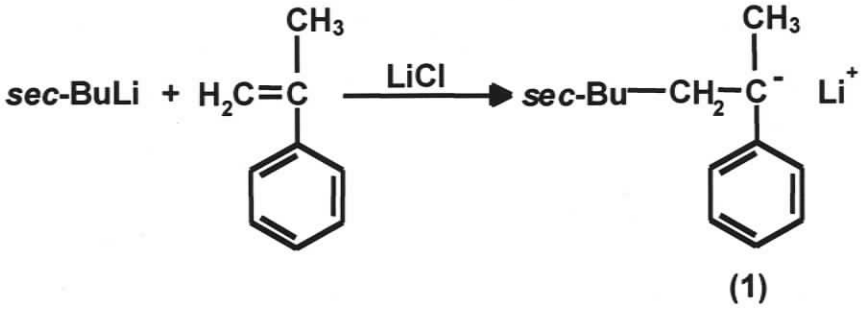

(1)

Scheme 1.1. Initiation of styrene with *sec*-butyllithium.

The propagation step follows this initiation step. This is achieved by cooling the mixture to -78°C and then adding the styrene monomer. The colour of the solution changes from deep red to a deep orange-yellow colour indicating that styrene has been activated[11-13]. As the polymerization continues, the active centers of the styrene are regenerated at the chain ends. This continues until all of the styrene has been used up. Once all the styrene has been consumed, the colour of the solution goes back to deep red as the leftover α-methylstyrene "caps" the end of the living chain ends forming **2** (scheme 1.2).

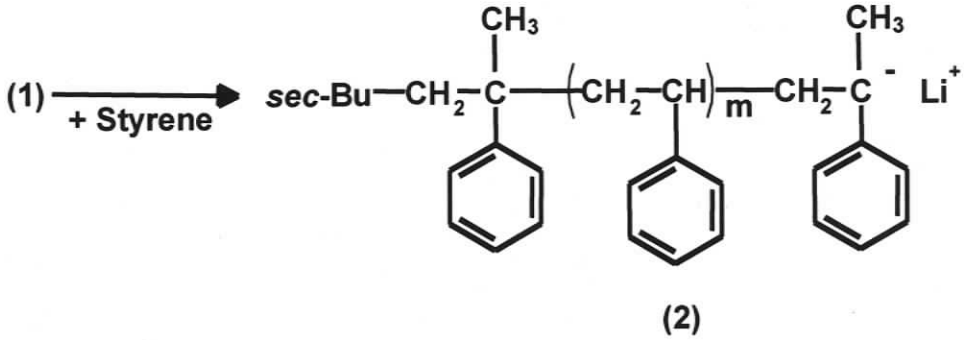

Scheme 1.2. Addition of styrene to activated complex (**1**), where *m* refers to the number of styrene repeat units.

To synthesize the second block of the diblock copolymer PS-*b*-PtBA, the second monomer, *tert*-butylacrylate, is added to the reaction mixture. Once the *tert*-buytlacrylate monomer is added, the deep red colour disappears quickly as **3** is formed, since activated PtBA, is colourless (Scheme 1.3). The presence of LiCl prevents undesired side reactions, such as reactions with the ester functional group or chain transfer reactions, by associating with the living chain ends, thus lowering their reactivity.

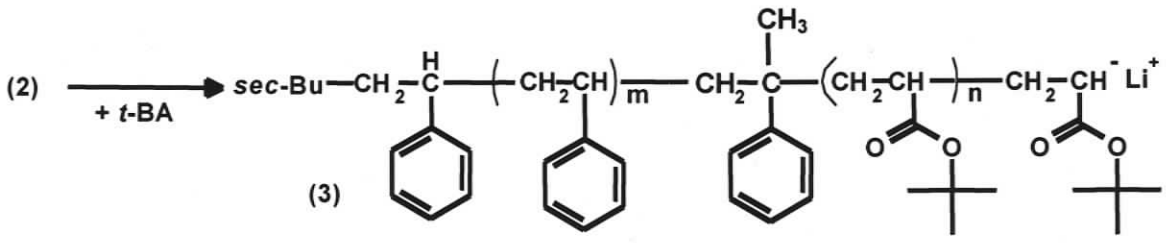

Scheme 1.3. Polymerization of the PtBA block via addition of *tert*-butylacrylate (*t*-BA) to yield polystyrene-*block*-poly(*tert*-butylacrylate) (PS-*b*-PtBA) with *m* average PS units, and *n* average PtBA repeat units.

Finally, the reaction is terminated by adding a small amount of methanol, and the final PS-*b*-PtBA diblock copolymer is recovered by precipitation into methanol. The experimental details of this sequential anionic polymerization will be described in chapters two and three of this thesis.

1.3. Micellization of Diblock Copolymers in Selective Solvents

When a diblock copolymer is dissolved in a solvent that is a thermodynamically good solvent for one of the blocks and a poor solvent for the other block, the insoluble blocks will strive to minimize unfavorable enthalpic interactions with the organic solvent by self-assembling to form block copolymer micelles, which consist of a core of the insoluble blocks and a surrounding corona of the soluble blocks. This process occurs when the concentration of block copolymers in the selective solvent is above the critical micelle concentration (CMC). In the specific case of amphiphilic diblock copolymers, in which one block is hydrophilic and the other block is hydrophobic, two possible classes of micelles can form, depending on the solvent. If the micelles are formed in an organic solvent, with a hydrophilic core and a hydrophobic corona, they are known as reverse micelles. If the micelles form in an aqueous media, with a hydrophobic core and a hydrophilic corona, they are referred to as regular micelles. Additionally, if the corona-forming block is large with respect to the core-forming block, the micelle is called "star-like", and if the reverse is true they are described as "crew-cut" micelles. These classification schemes are represented pictorially in Figure 1.2. As represented in this figure, spherical micelle morphologies are most common, although a wide range of non-

spherical morphologies have been observed in "crew-cut" systems in water, in which the hydrophilic blocks are relatively short.

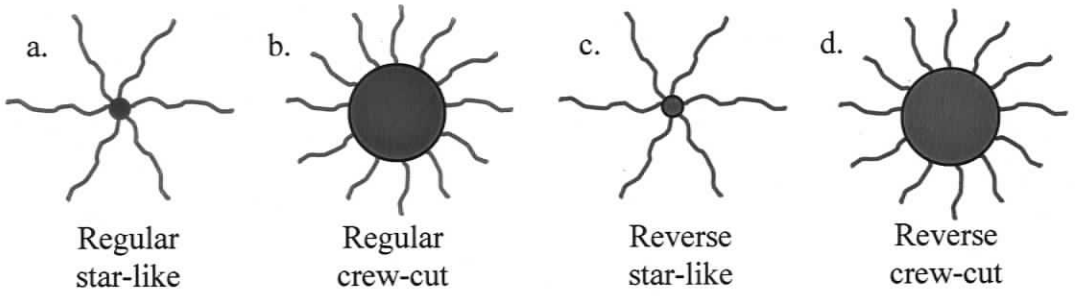

Figure 1.2. Illustrations of the various definitions of amphiphilic diblock copolymer micelles in aqueous solvent (a, b), and organic solvent (c, d). Red indicates hydrophobic and blue represents the hydrophilic blocks.

1.4. Micellization of Amphiphilic Diblock Copolymers in Aqueous Solutions

Many efforts have been invested into the study of micellization of amphiphilic block copolymers in aqueous solutions. As mentioned earlier, micellization is thermodynamically favourable when the concentration of block copolymers in the solution reaches a certain level, known as the critical micelle concentration (CMC).

There are many factors that affect the CMC of certain amphiphilic diblock copolymers in aqueous media: among these factors are pH, ionic strength and lengths of both the insoluble and soluble blocks.

In a study by Khougaz *et al*[14], the effect of ionic strength on the CMC of poly(styrene)-*b*-poly(sodium acrylate) (PS-*b*-PANa) copolymers in aqueous media was studied. For salt concentrations of 0.10 - 2.5 M NaCl, it was found that the CMC generally decreases linearly with the square root of the salt concentration[14]. The

polymers in this study were prepared via anionic polymerization. In this study, the CMC was determined using static light scattering (SLS), by dissolving various copolymer samples in deionized water and heating at 100°C, thus inducing the formation of star-like micelles.

Astafieva *et al*[14] also investigated the effect of the length of the insoluble polystyrene block on the CMC. They found that as the length of the polystyrene chain increased, the CMC decreased, for example, when the polystyrene block length is changed from 6 to 110 units and the soluble block length is kept constant, the CMC decreased from 1.6×10^{-5} to 5×10^{-8} M. However, the effect of increasing the soluble block length, PANa, on the CMC is not as clear-cut as increasing the insoluble block length. If the soluble block is really short, increasing its length leads to an increase in the CMC because more water is required for the system to micellize due to more soluble chains being present. However, there is a point when a maximum is reached. Once the soluble block lengths are longer, increasing their length results in a decrease of the CMC. This phenomenon can be explained by understanding the effect the conformation of the chains has on the CMC: when the PANa chains are short in length they are not as extended as longer blocks of PANa chains would be and thus having longer PANa chains decreases the amount of water needed to reach micellization.

Whereas the aqueous micelles in the studies described above were star-like and spherical, Zhang *et al.*[15-20] investigated multiple micelle morphologies of poly(styrene)-*b*-poly(acrylic acid) (PS-*b*-PAA) crew-cut micelles, prepared by dissolving the copolymers in DMF which is a favourable solvent for both the polystyrene and poly(acrylic acid) blocks. Then, water was slowly added to the system, making the solvent more

thermodynamically unfavourable for the polystyrene blocks. For a particular copolymer concentration, the thermodynamic critical point for micelle formation by this method is the critical water content (CWC), defined as the water concentration in solvent above which micelles are detected. Just above the CWC, the micelles existed in dynamic equilibrium with single copolymer chains, since swelling of the PS cores with DMF provided sufficient mobility, via plasticization, for copolymer chains to escape from the micelle. However, with continued water addition, DMF was progressively leached out of the cores, decreasing the mobility of PS chains until above a certain water content the micelles become kinetically frozen on the time scale of further water addition. Once water had been added to well above this "freezing point" the frozen aggregates were dialyzed against deionized water to remove residual organic solvent, then the structures were investigated by TEM. In the crew-cut composition regime, the insoluble block content (in this case PS) was varied from 80 - 98 wt%. As the PAA content decreased (PS content increased), the morphology changed from spheres to cylinders to vesicles and finally to large compound micelles consisting of an assembly of inverted micelles surrounded by a hydrophilic surface[16]. Though these various aggregate morphologies in pure water were not equilibrium structures, they can be regarded as kinetically frozen "snap shots" of earlier thermodynamic states in DMF/water mixtures when a dynamic equilibrium existed between micelles and copolymer chains.

In another study, Zhang *et al.*[19] investigated the effect of the copolymer concentration and molar mass on the CWC for PS-*b*-PtBA crew-cut micelles formed in DMF/water mixtures by water addition. Using static light scattering (SLS) to detect the onset of micellization with water addition, they determined that as the polymer

concentration or molar mass increased the CWC decreased[19] For example, the measured CWCs ranged ~4-5 wt% for PS(500)-*b*-PAA(60) and ~3-4 wt% for PS(1140)-*b*-PAA(165)[19]. In the same study, the rate of chain exchange between micelles above the CWC was also investigated as a function of water content, by mixing different sized micelle solutions and monitoring changes in size distribution over time by transmission electron microcopy (TEM). It was determined that for water contents up to 6 wt%, chain exchange between micelles was significant on a time scale of 1 day. However, at 11 wt% water, the micelles were determined to be kinetically frozen, with no significant chain exchange between micelles on a reasonable time scale.

Zhang *et al.*[18] further investigated the thermodynamic and kinetic aspects of PS-*b*-PAA micellization in DMF/water mixtures of different water contents. In this study, micellization of PS(190)-*b*-PAA(20) was induced by two different methods: either by adding the water dropwise to a solution of block copolymer and DMF or by direct dissolution of the block copolymer in a DMF/water mixture. It was found that as the block copolymer concentration was increased, the morphology changed from spheres, to rod-like micelles, to interconnected rods, and then finally to bilayers, with morphological boundaries shifting to lower polymer concentration as the water was increased. The relative importance of thermodynamics and kinetics in determining the morphologies was studied by varying the amount of added water and also the method the water was added: when the water content was lower than 6.5 wt%, the kinetics of chain exchange were fast on an experimental time scale, and micellization was controlled by thermodynamics only, with reversible morphological transitions. However, when the water content was increased to between 7.5 and 9.5 wt% the morphological reversibility of the micelles

decreased significantly, indicating that kinetic aspects became more important as the solvent swelling of the cores decreased. In particular, when the water was added dropwise, the morphological changes from spheres to rods and finally to bilayers were not achieved within several days due to the slow polymer chain exchange and the strong repulsive interactions among the micelles, but the morphology changes in the opposite direction were possible since chains within the aggregates were significantly mobile to achieve structural fission and rearrangement[18]. As will be described in a later chapter, these issues of the polymer concentration effect on the CWC and kinetic aspects of micelle formation in DMF/water mixtures are of central importance to the strategy of size control of large compound micelles (LCMs) demonstrated in this thesis.

1.5. Micellization of Ionic Diblock Copolymers in Organic Solvents

Ionic block copolymers are defined as block copolymers that carry charge on one of the blocks. The large incompatibility between the ionic and hydrophobic blocks provides a strong driving force for microphase separation and micelle formation. It is beneficial to differentiate between two classes of ionic block copolymers: block polyelectrolytes and block ionomers. Eisenberg and Rinaudo differentiate the two classes by the effect of the ionic groups on the properties[21]. From their definition, block polyelectrolytes have properties that are defined by electrostatic interactions over the relatively large distances within the micelle corona and between the aggregates, whereas block ionomers are defined by their strong, short-range electrostatic relations within ionic microdomains. Block polyelectrolytes and block ionomers can therefore often be distinguished by the medium in which the ionic copolymer is dispersed, with aqueous

solutions resulting in block polyelectrolytes and organic solvents resulting in block ionomers. For the present work, block ionomer micelles (i.e. in organic solvents) were employed to template the synthesis of inorganic nanoparticles (NP), using the metal counterions of a negatively-charged polyacrylate core as precursors in the reaction. This specific example is discussed below.

Polystyrene-*block*-poly(acrylic acid) (PS-*b*-PAA) is soluble in a mixed benzene/methanol solvent system at low pH; however, upon addition of a base ($Cd(CH_3COO)_2$ in the present case), the labile proton on the carboxylic acid group can be removed, thus creating a negatively-charged ionic block. This simple procedure will induce micellization due to extremely unfavorable interactions between the apolar organic solvent and the charged block, forming a block ionomer micelle with a poly(cadmium acrylate) (PACd) core and a polystyrene (PS) corona. This process is schematically illustrated in scheme 1.3, and has been shown to be extremely useful in the synthesis of polymer-stabilized inorganic NPs, as described later in this chapter.

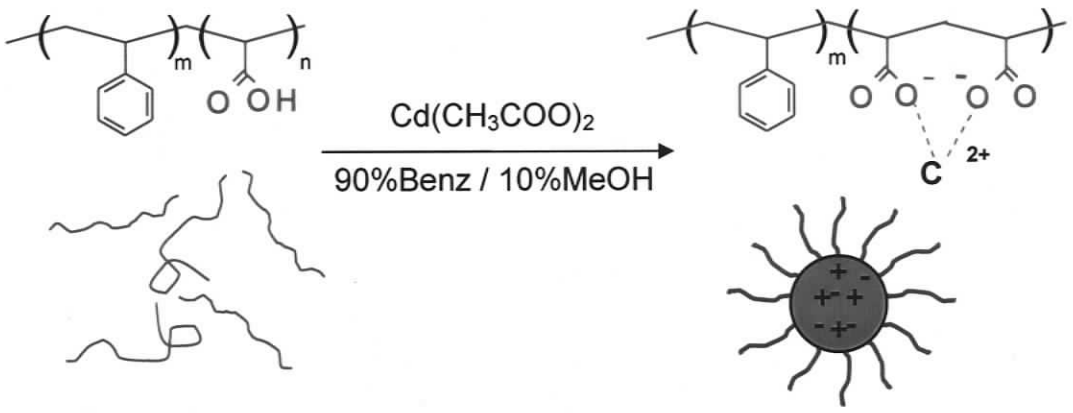

Scheme 1.3. Formation of block ionomer micelles by removing the acidic proton on the poly(acrylic acid) (PAA) chains inducing micellization. Top structures detail the chemical structure before and after addition of $Cd(CH_3COO)_2$ base. Bottom cartoons illustrate the configuration of the diblock copolymers (ionomers) before and after base addition.

1.6. Semiconducting Nanoparticles and the Quantum Confinement Effect

For the past few decades, there has been an increase in the study of nanoparticles. Specifically, the area of semiconducting nanoparticles has been of interest to chemistry and physics research. Nanoparticles are known as a class of materials that fall between the molecular and bulk solid limits and have an average size of 1-10 nm[22]. Inorganic nanoparticles exhibit physical and chemical properties different from either the individual molecules or the bulk solids. The properties of semiconducting nanoparticles are size-dependent due to an increase in the surface-to-volume ratio compared to the bulk material and to changes in the electronic structure due to quantum confinement effects[22]. An example of the former effect is seen in the differing melting point of cadmium sulfide (CdS) depending on whether it is in bulk or nanocrystal form: CdS in the bulk has a melting point of ~1600°C, whereas a 2.5 nm CdS nanocrystal has a melting point ~400°C[23]. The reason for this dramatic change in melting point temperature is due to the

higher surface energy of the nanoparticles compared to the bulk. Apart from such effects of large surface areas, semiconducting nanoparticles undergo changes in their optical and electronic properties as a function of size, which is attributed to the quantum confinement effect described below.

When a semiconductor is excited by light of sufficient energy, an electron is promoted from its valence band to its conduction band. What is left in the valence band is a hole, of positive charge, creating an electron-hole pair termed an exciton, which has a size characterized by the Bohr excitonic radius[24]. In a semiconducting nanoparticle (also termed a quantum dot), the particle size is on the order of the Bohr excitonic radius, giving rise to a confinement energy which raises the energy of the exciton relative to the bandgap of the bulk semiconductor. Brus[25] explained this situation as a particle (the electron) in a spherical box (the nanoparticle), where the movement of the electron is confined by an infinitely high potential at the surface. As a result, there is a confinement energy associated with the electron, and the exciton energy for semiconducting nanoparticles can be described by the following equation:

$$E^* \cong E_g + \frac{\hbar^2 \pi^2}{2R^2}\left[\frac{1}{m_e} + \frac{1}{m_h}\right] - \frac{1.8e^2}{\varepsilon R} + \ldots \qquad (5)$$

where E^* is the energy of the exciton, E_g is the energy of the band-gap, R is the radius of the particle, m_e and m_h are the masses of the electrons and holes in the lattice, e is the charge of an electron and ε is the permittivity. The second term on the right-hand-side is the confinement energy arising from the "particle-in-a-box" model, and shows that the energy of the exciton increases as the size of the nanoparticle decreases[25].

A clear demonstration of the quantum confinement effect is seen in the absorption spectra of semiconducting nanoparticles of different average sizes. The absorption spectra of CdS nanoparticles of different mean sizes in aqueous solution is shown in Figure 1.3[22]. The particles that are larger than 6 nm, which is larger than the average size of an exciton (~5.8 nm) in the macrocrystalline material, begin to absorb close to 515 nm (or 2.4 eV, which corresponds to the bandgap of bulk CdS). As the nanoparticle size decreases, the absorption shifts to shorter wavelengths, which correspond to higher energies.

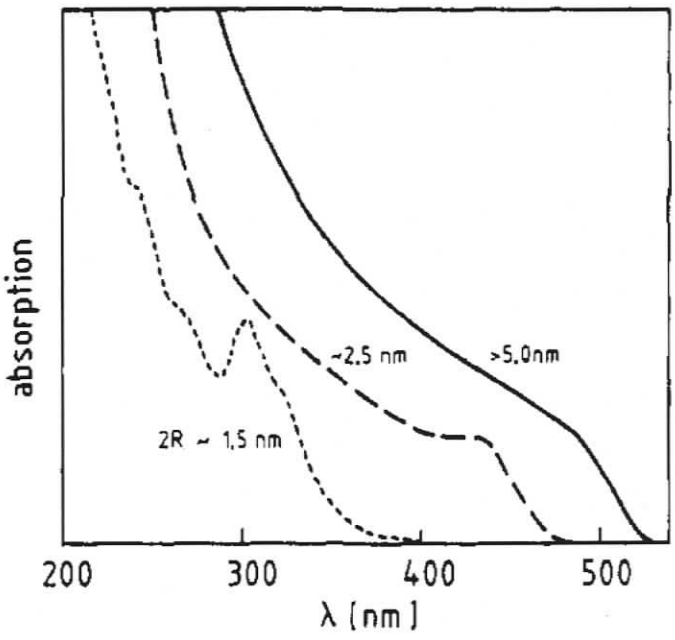

Figure 1.3. UV-Vis absorption spectra of CdS nanoparticles of different mean particle sizes[22].

1.7. Hierarchical Assemblies

Mother Nature has given us many examples of how complex and beautiful self-assembly can be: the structure of a seashell, a protein-aragonite scaffolding, the beautiful colours of certain butterflies, and the highly desirable mechanical properties of natural spider silk are just a few examples[3, 26]. The benefit of chemical self-assembly is that it provides potential routes to the fast and efficient synthesis of highly complex and functional 2D and 3D structures[3, 27-35].

Several approaches to organization of metal and semiconducting nanoparticles on multiple length scales have been investigated[36-55]. Figure 1.4[56] shows an approach by Kumacheva and coworkers. In this strategy, CdS nanoparticles within ordered arrays of polymer spheres (size ~6 nm) were produced by employing several steps: first, in situ synthesis of nanoparticles on the surface of polymer microspheres was carried out followed by organization of these hybrid microspheres into 3D ordered nanocomposite arrays[56]. Figure 1.4 explains the approach in more detail: monodisperse poly(methyl methacrylate)-poly(methacrylic acid), (PMMA-PMAA), latex particles were synthesized via emulsion polymerization. The particles were then treated with KOH followed by treatment with a solution of $Cd(ClO_4)_2$ to initiate ion exchange between the K^+ counterions in the electrical double layer and the Cd^{2+} ions bearing a higher charge. This was followed by treatment with a solution of Na_2S to yield CdS nanoparticles on the surface of PMMA-PMAA beads. In some cases, the beads with CdS were assembled using various methods, for example: evaporative assembly, electrodopesition or oscillatory shear. Kumacheva and co-workers wanted to eliminate the space voids in their material and they accomplished this by synthesizing a polymer shell over their CdS nanoparticles and then annealing it to remove the polymer to get a final matrix with no

space voids. This synthetic approach gives excellent control of the overall size of the polymers beads and therefore control overall lattice periodicity; however, there is not good control of interparticle distances between the nanoparticles inside the beads, which are randomly nucleated on the surface of PMMA-PMAA polymer[56].

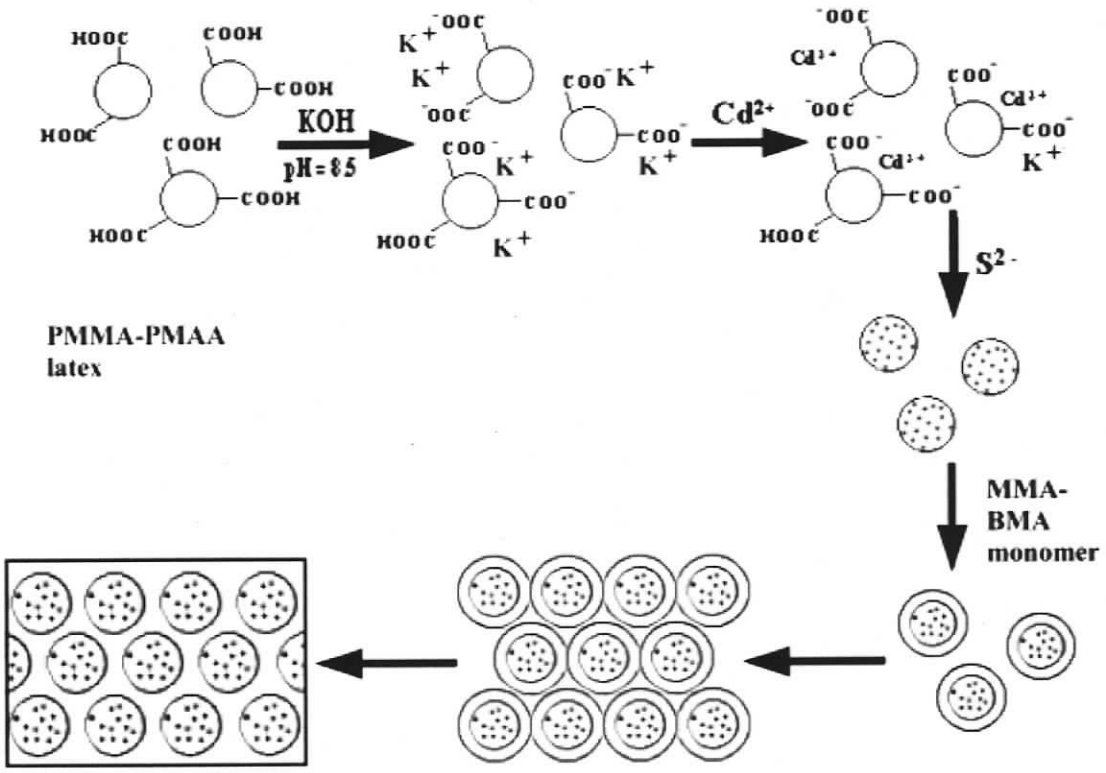

Figure 1.4. Hybrid Nanocomposite Materials with Periodic Structure[56].

Another approach to multi-scale organization of nanoparticles employs micron-sized inorganic cores that are coated with hybrid shells of varying composition using layer-by-layer assembly (LbL)[44-48, 50,57-61] The approach of LbL readily allows control over the shell composition, structure, and thickness at the nanometer level and it uses the stepwise adsorption of preformed inorganic materials and oppositely charged polymers on colloidal templates. Biological macromolecules, multivalent dyes, silicate sheets, or

nanoparticles and polymers are all examples that take advantage of the layer-by-layer technique [56-60]. Caruso *et al*[62] used the LbL assembly to build colloidal crystals that are made up of colloidal spheres coated with a hybrid shell of semiconductor nanocrystals and polyelectrolytes as building blocks. This approach gives them a route to form core-shell particles with excellent control of the hybrid shell thickness and composition, and of the final particle diameter. In this particular study, Caruso *et al*[62] used submicrometer-sized polystyrene colloidal spheres that were coated with hybrid films that consist of HgTe semiconductor NPs and polyelectrolyte (PE) multilayers. By using the LbL technique, the coated spheres were crystallized and formed composite colloidal crystals. Caruso *et al* found that increasing the number of the HgTe NP layers deposited on the colloidal spheres led to an increase in both the diameter and the effective refractive index of the spheres, and a red shift of the stop bands of the composite colloidal crystals was observed.

Supramolecular approaches toward colloidal nanoparticle organization are exemplified by the "bricks and mortar"[51-55, 62-65] strategy. This polymer-mediated technique offers control over the ordering of the nanoparticles due to specific recognition between functional groups. In this strategy, as seen in Figure 1.5, colloidal gold particles functionalized with recognition elements (thymine-functionalized mixed-monolayer protected gold clusters) serve as the bricks, while the polymers bearing complementary functionalities (diamintroizine-functionalized polymer) serve as mortar that hold together the assemblies of colloidal particles via supramolecular interactions[65]. In this model, in non-polar solvents, the polymer folds into a highly compact structure owing to intramolecular hydrogen bonds between the triazines. Multivalent interactions between

the polymer and the Thy-Au induce the unfolding of the compact structure, which exposes further triazine recognition units. This allows the polymer to further interact with the Thy-Au units which propagates the assembly process[65]. Self-assembly processes are sensitive to entropic and enthalpic effects, as evidenced by the temperature dependence of aggregated structures[65]. TEM micrographs of aggregates formed at -20°C showed the formation of microscale (5-10 μm) polydisperse discrete spherical particles. Aggregates that are formed at room temperature, 23°C, yielded in comparison smaller diameters, in average 5 to 10 times smaller than the aggregates that formed at -20°C[65]. However, despite demonstrated thermal size control, aggregates formed by this method tended to be quite polydisperse. To achieve control over the aggregate dimensions, they applied, as the mortar, three symmetric diblock copolymers and varied their total lengths[64]. The aggregate's growth is therefore restricted by the diblock copolymer, which is a feature of micro-phase separation and the final size is determined by the functionalized block length. This supramolecular approach offers excellent control over the distances between the nanoparticles[64]. Finally, Rotello and co-workers wanted to control the interparticle spacing of their nanoparticles[63]. To control the interparticle distances they used poly(amido-amine) (PAMAM) dendrimers of different generations (G_0-G_6) as the mortar units. From their Small angle scattering of x-ray (SAXS) results, they saw a clear correlation between particle-particle spacing and the dendrimer generation, as the dendrimer generation increased, the particle-particle spacing increased[63].

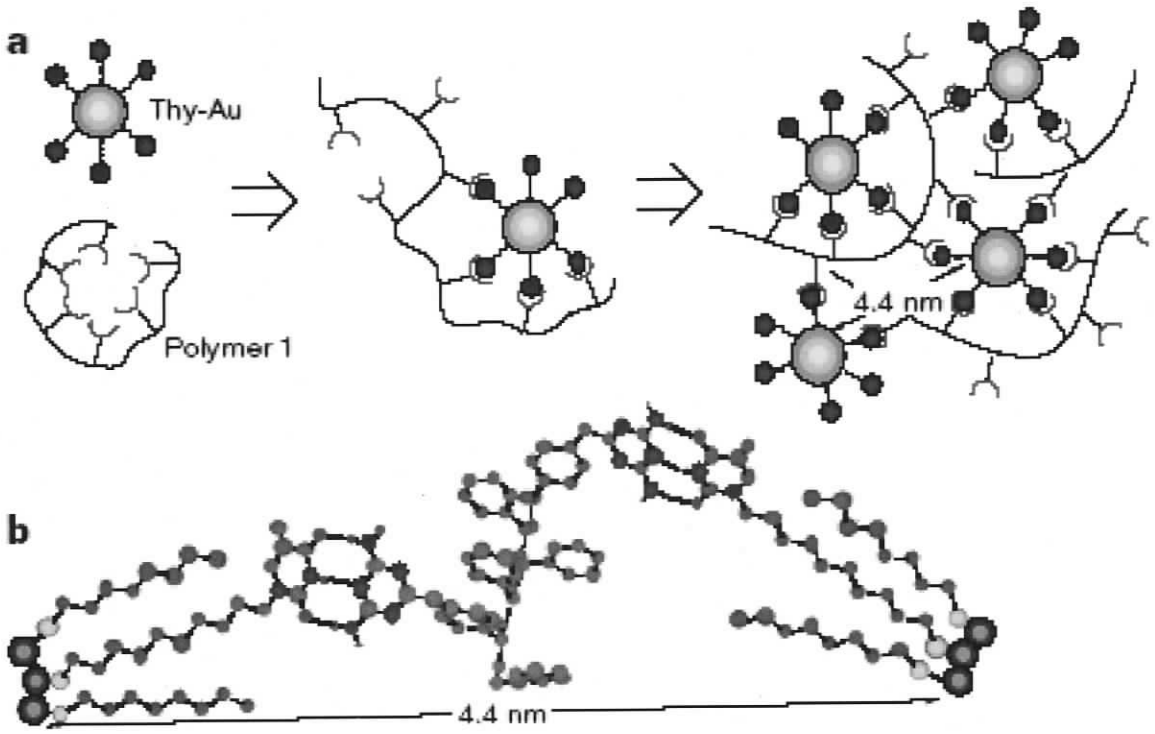

Figure 1.5. Proposed mechanism for the aggregation of polymer **1**-Thy-Au. **a**, Polymer mediated self-assembly of Thy-Au, showing the experimentally determined interparticle distance. **b**, Proposed polymer **1**-Thy-Au self-assembled structure (using the AMBER force field as implemented by Macromodel 4.0), showing the computationally predicted interparticle distance[65].

1.8. Target of This Project

This thesis will employ a new multi-step self-assembly approach to photonic structures, based on hybrid building blocks of CdS nanoparticles encapsulated in the cores of stable block ionomer micelles. The aim of this thesis is to demonstrate a route to hierarchical photonic materials with potential applications in optical switching and light-emitting devices. A unique and essential feature of this approach is that separate self-assembly steps are used to impart order on progressively longer length scales, using different media to induce self-assembly of increasingly complex building blocks. This

will allow for unprecedented control of multi-scale ordering, since factors that control ordering on different length scales are operative in different self-assembly steps. Photoluminescence will be measured after each self-assembly step, allowing the effects of ordering on various length scales to be determined. An additional advantage of this strategy is that the optical effects of nanoparticle ordering should be fully decoupled from effects related to the nanoparticle surface, with the micelle core maintaining a constant nanoparticle surface environment during each self-assembly step.

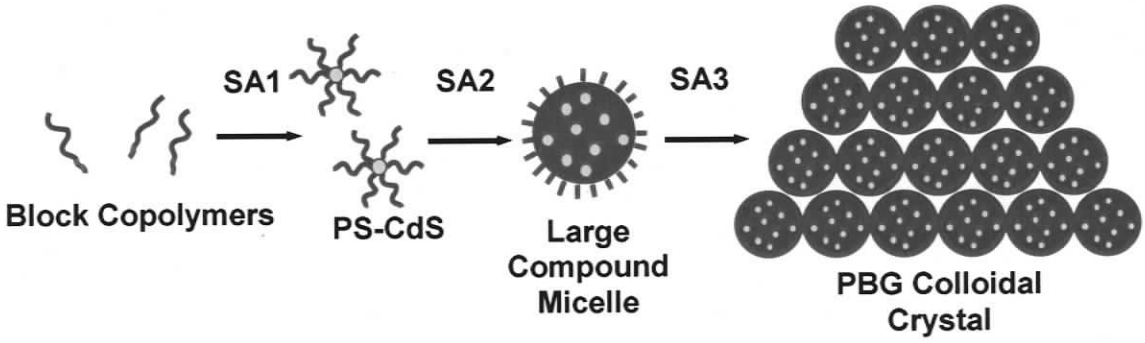

Figure 1.6. Strategy to materials with multiple length scales.

The proposed multi-step strategy (Figure 1.6) is as follows: in a primary self-assembly step (SA1), polystyrene(PS)-*b*-poly(acrylic acid)(PAA)-based block ionomers will form stable micelles in organic solvents, each with an ionic polyacrylate core and solubilized PS corona; a single cadmium sulfide (CdS) nanoparticle (3-5 nm) will subsequently be synthesized in each core, forming stable hybrid inorganic/block copolymer building blocks designated PS-CdS (Figure 1.7). Although SA1 occurs under equilibrium conditions, the PS-CdS particles are kinetically frozen aggregates, which can be recovered as a yellow powder and transferred into various organic solvents.

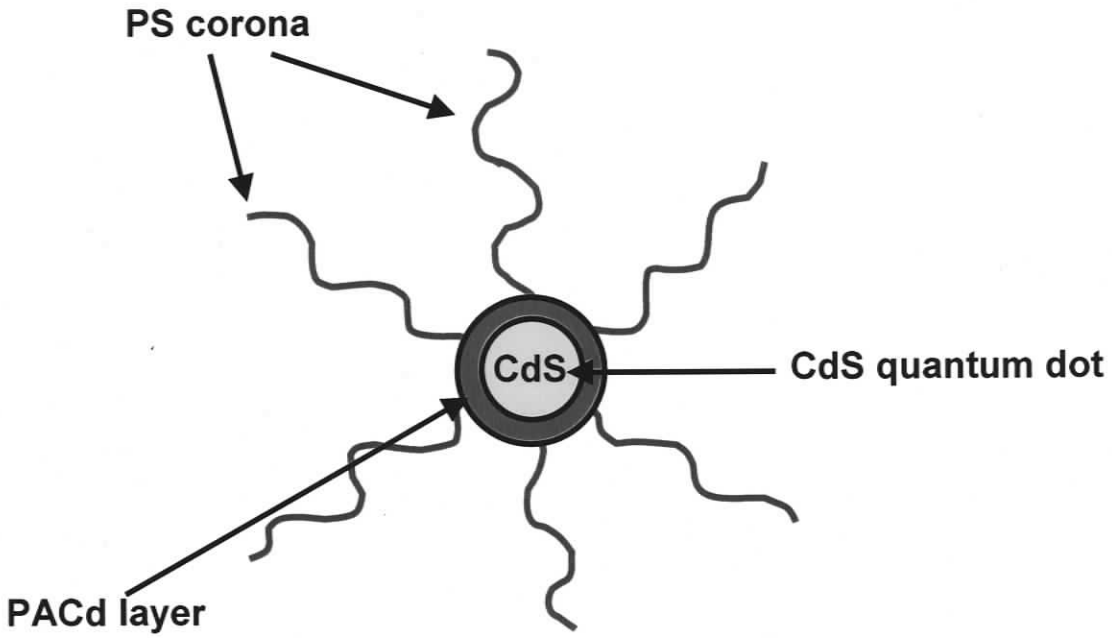

Figure 1.7. Hybrid PS-CdS building block.

Next, PS-CdS will be blended with stabilizing PS-*b*-PAA chains in DMF, then slowly transferred to an aqueous medium where they will undergo secondary self-assembly (SA2), forming spherical nanoparticle assemblies, termed large compound micelles (LCMs) (Figure 1.8). A reasonable model for LCM formation is an arrested phase-separation process induced by water addition; above a critical water concentration (CWC) PS-CdS micelles undergo clustering to form a polymer-rich phase, stabilized at the surface by the "free" PS-*b*-PAA chains. Clusters of the phase-separated nanoparticles grow to minimize interfacial energy, but become kinetically trapped with continued water addition, in a similar manner to crew-cut aggregates in DMF/water mixtures, described previously.

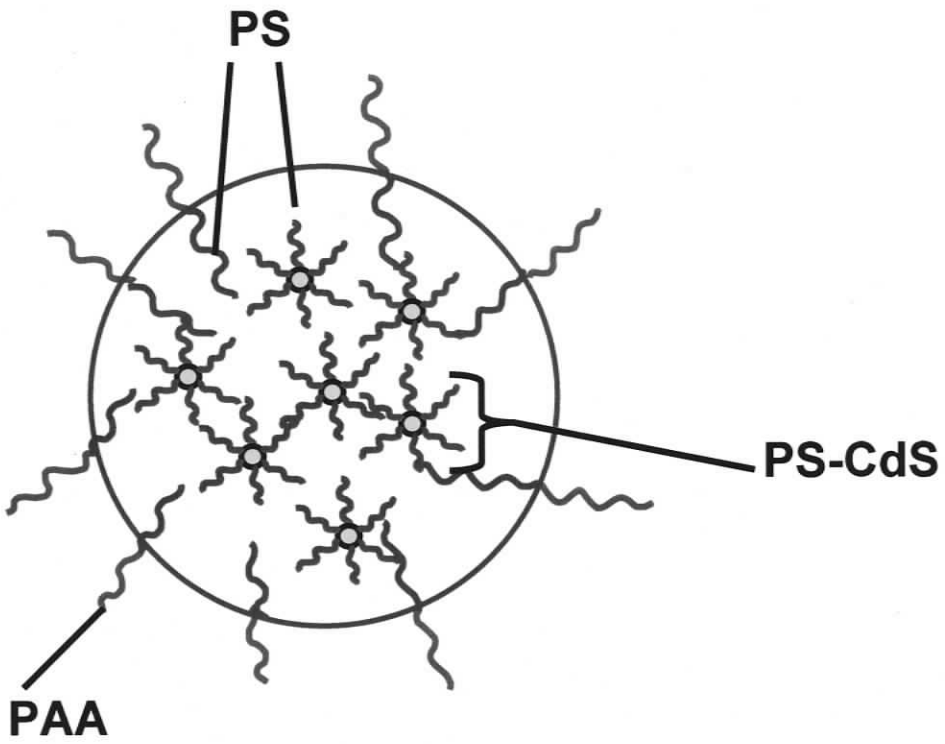

Figure 1.8. Large Compound Micelle (LCM).

In a final self-assembly step (SA3), slow evaporation of water from LCM dispersions will be used to induce ordering of spherical LCMs into close-packed three-dimensional (3D) crystals. In previous work, the feasibility of steps SA1 and SA2[66-67] has been demonstrated, however, the application of these processes to produce complex tertiary structures has not been shown.

It is of critical importance to control the size and polydispersity of LCMs in the secondary self-assembly step (SA2) because these factors will have a direct effect on the ordering of the final step, SA3. LCMs with PS-CdS nanoparticles have been previously synthesized by Moffitt and co-workers[66] using the SA1 and SA2 steps described earlier.

However, size control and factors affecting polydispersity were not investigated in that study. The size of LCMs will determine the periodicity of close-packed arrays formed in the SA3 step, which will determine the wavelength of light which selectively propagates through the crystal, according to the Bragg equation[6]. For selective propagation of visible light at normal incidence, LCMs with sizes between 150 – 350 nm will be required. Also, to achieve an ordered 3D array of LCMs, low LCM polydispersity will be essential.

This thesis will be divided in the following manner: in Chapter 2, the effects of blend composition (amount of stabilizing chains) and nanoparticle aggregation on LCM formation in the SA2 step will be described. In Chapter 3, by varying different parameters such as initial polymer concentration, composition and rate of water addition, we will demonstrate effective size control of LCMs in the SA2 step. Finally, Chapter 4, will focus on the self-assembly of LCMS (SA3 step) into ordered 3D arrays with unique hierarchical structure.

References

1. Ewers, T. D.; Sra, A. K.; Norris, B. C.; Cable, R. E.; Cheng, C.-H.; Shantz, D. F.; Schaak, R. E. *Chem. Mater.* **2005,** 17, 514-520.

2. de A. A. Soler-Illia, G.; Sanchez, C.; Lebeau, B.; Patarin, J. *Chem. Rev.* **2002,** 102, 4093-4138.

3. Fendler, J. H. *Chem. Mater.* **2001,** 13, 3196-3210.

4. Ma, Y.; Qi, L.; Ma, J.; Cheng, H.; Shen, W. *Langmuir* **2003,** 19, 9079-9085.

5. Murray, C. B.; Keagan, C. R.; Bawendi, M. G. *Annu. Rev. Mater. Sci.* **2000,** 30, 545-610.

6. Xia, Y.; Gates, B.; Ying, Y.; Lu, Y. *Adv. Mater.* **2000,** 12, (10), 693-713.

7. Xia, Y.; Gates, B.; Li, Z.-Y. *Adv. Mater.* **2001,** 13, 409-413.

8. Cowie, J. M. G., *Polymers: Chemistry and Physics of Modern Materials*. Second ed.; T. J. International Ltd: Cheltenham, 1991.

9. Nicholson, J. W., *The Chemistry of Polymers*. Second Edition ed.; The Royal Society of Chemistry: Letchworth, 1997.

10. Young, R. J.; Lovell, P. A., *Introduction to Polymers*. Second Edition ed.; Chapman & Hall: New York, 1991.

11. Zhong, X. F.; Varshney, S. K.; Eisenberg, A. *Macromolecules* **1992,** 25, 7160-7167.

12. Hautekeer, J.-P.; Varshney, S. K.; Fayt, R.; Jacobs, C.; Jerome, R.; Teyssie, P. *Macromolecules* **1990,** 23, 3893-3898.

13. Gao, Z.; Zhong, X. F.; Eisenberg, A. *Macromolecules* **1994,** 27, 7160.

14. Khougaz, K.; Astafieva, I.; Eisenberg, A. *Macromolecules* **1995,** 28, 7135-7147.

15. Zhang, L.; Barlow, R. J.; Eisenberg, A. *Macromolecules* **1995,** 28, 6055-6066.

16. Zhang, L.; Eisenberg, A. *J. Am. Chem. Soc.* **1996,** 118, 3168-3181.

17. Zhang, L.; Eisenberg, A. *Journal of Polymer Science: Part B: Polymer Physics* **1999,** 37, 1469-1484.

18. Zhang, L.; Eisenberg, A. *Macromolecules* **1999,** 32, 2239-2249.

19. Zhang, L.; Shen, H.; Eisenberg, A. *Macromolecules* **1997,** 30, 1001-1011.

20. Zhang, W.; Shi, L.; An, Y.; Gao, L.; Wu, K.; Ma, R. *Macromolecules* **2004,** 37, 2551-2555.

21. Eisenberg, A.; Rinaudo, M. *Polymer Bulletin* **1990,** 24, 671.

22. Hengleing, A. *Chem. Rev.* **1989,** 89, 1861-1873.

23. Goldstein, A. N.; Echer, C. M.; Alivisatos, A. P. *Science* **1992,** 256, 1425.

24. Murphy, C. J. *Anal. Chem.* **2001**, 520A.

25. Brus, L. E. *J. Phys. Chem.* **1986,** 90, 2555-2560.

26. Vukusic, P.; Sambles, J. R. *Nature* **2003,** 424, 852-855.

27. Maye, M. M.; Lim, I.-l. S.; Luo, J.; Rab, Z.; Rabinovich, D.; Liu, T.; Zhong, C.-J. *J. Am. Chem. Soc.* **2005,** 127, 1519-1529.

28. Maye, M. M.; Luo, J.; Lim, I.-l. S.; Han, L.; Kariuki, N. N.; Rabinovich, D.; Liu, T.; Zhong, C.-J. *J. Am. Chem. Soc.* **2003,** 125, 9906-9907.

29. Maya, L. *Langmuir* **2000,** 16, 9151-9154.

30. Moffitt, M.; McMahon, L.; Pessel, V.; Eisenberg, A. *Chem. Mater.* **1995,** 7, 1185-1192.

31. Moffitt, M.; Eisenberg, A. *Chem. Mater.* **1995,** 7, 1178-1184.

32. Mokari, T.; Sertchook, H.; Aharoni, A.; Ebenstein, Y.; Avnir, D.; Banin, U. *Chem. Mater.* **2005,** 17, 258-263.

33. Adachi, E. *Langmuir* **2000,** 16, 6440-6463.

34. Yonezawa, T.; Matsune, H.; Kimizuka, N. *Adv. Mater.* **2003,** 15, (6), 499-503.

35. Cha, J. N.; Birkedal, H.; Euliss, L. E.; Bartl, M. H.; Wong, M. S.; Deming, T. J.; Stucky, G. D. *J. Am. Chem. Soc.* **2003,** 125, 8285-8289.

36. Kumacheva, E.; Klein, J.; Pincus, P.; Fetters, L. J. *Macromolecules* **1993,** 26, 6477-6482.

37. Kumacheva, E.; Kalinina, O.; Lilge, L. *Adv. Mater.* **1999,** 1, (3), 231-234.

38. Kumacheva, E.; Golding, R. K.; Allard, M.; Sargent, E. H. *Adv. Mater.* **2002,** 14, (3), 221-224.

39. Nie, Z.; Xu, S.; Seo, M.; Lewis, P. C.; Kumacheva, E. *J. Am. Chem. Soc.* **2005,** 127, 8058-8063.

40. Kitaev, V.; Kumacheva, E. *Langmuir* **1998,** 14, 5568-5572.

41. Sohn, D.; Kitaev, V.; Kumacheva, E. *Langmuir* **1999,** 15, 1698-1702.

42. Kalinina, O.; Kumacheva, E. *Chem. Mater.* **2001,** 13, 35-38.

43. Kalinina, O.; Kumacheva, E. *Macromolecules* **1999,** 32, 4122-4129.

44. Caruso, F.; Mohwald, H. *Langmuir* **1999,** 15, 8276-8281.

45. Blomberg, E.; Poptoshev, E.; Claesson, P. M.; Caruso, F. *Langmuir* **2004,** 20, 5432-5438.

46. Salgeirino-Maceira, V.; Caruso, F.; Liz-Marzan, L. M. *J. Phys. Chem. B* **2003,** 107, 10990-10994.

47. Schoeler, B.; Sharpe, S.; Hatton, T. A.; Caruso, F. *Langmuir* **2004,** 20, 2730-2738.

48. Kumaraswamy, G.; Dibaj, A. M.; Caruso, F. *Langmuir* **2002,** 18, 4150-4154.

49. Yu, K.; Zhang, L.; Eisenberg, A. *Langmuir* **1996,** 12, 5980-5984.

50. Yu, A.; Meiser, F.; Cassagneau, T.; Caruso, F. *Nano Lett.* **2004,** 4, (1), 177-181.

51. Niemz, A.; Rotello, V. M. *Acc. Chem. Res.* **1999,** 32, 44-52.

52. Drechsler, U.; Thibault, R. J.; Rotello, V. M. *Macromolecules* **2002,** 35, 9621-9623.

53. Boal, A. K.; Gray, M.; Ilhan, F.; Clavier, G. M.; Kapitzky, L.; Rotello, V. M. *Tetrahedron* **2002,** 58, 765-770.

54. Shenhar, R.; Rotello, V. M. *Acc. Chem. Res.* **2003,** 36, 549-561.

55. Shenhar, R.; Norsten, T. B.; Rotello, V. M. *Adv. Mater.* **2005,** 17, (6), 657-669.

56. Zhang, J.; Coombs, N.; Kumacheva, E. *J. Am. Chem. Soc.* **2002,** 124, 14512-14513.

57. Caruso, F.; Caruso, R., A.; Mohwald, H. *Science* **1998,** 282, 1111-1114.

58. Schuetz, P.; Caruso, F. *Chem. Mater.* **2004,** 16, 3066-3073.

59. Wang, D.; Rogach, A. L.; Caruso, F. *Chem. Mater.* **2003,** 15, 2724-2729.

60. Gaponik, N.; Radtchenko, I. L.; Gerstenberger, M., R.; Fedutik, Y. A.; Sukhorukov, G. B.; Rogach, A. L. *Nano Lett.* **2003,** 3, (3), 369-372.

61. Hong, X.; Li, J.; Wang, M.; Xu, J.; Guo, W.; Li, J.; Bai, Y.; Li, T. *Chem. Mater.* **2004,** 16, 4022-4027.

62. Norsten, T. B.; Frankamp, B. L.; Rotello, V. M. *Nano Lett.* **2002,** 2, (12), 1345-1348.

63. Frankamp, B. L.; Boal, A. K.; Rotello, V. M. *J. Am. Chem. Soc.* **2002,** 124, 15146-15147.

64. Frankamp, B. L.; Uzun, O.; Ilhan, F.; Boal, A. K.; Rotello, V. M. *J. Am. Chem. Soc.* **2002,** 124, 892-893.

65. Boal, A. K.; Ilhan, F.; DeRouchey, J. E.; Thurn-Albrecht, T.; Russell, T. P.; Rotello, V. M. *Nature* **2000,** 404, 746-748.

66. Moffitt, M.; Vali, H.; Eisenberg, A. *Chem. Mater.* **1998,** 10, 1021-1028.

67. Wang, C.-W.; Moffitt, M. *Langmuir* **2004,** 20, 11784-11796.

CHAPTER 2

Spherical Nanoparticle Assemblies in Water via Self-Assembly of Block Copolymer-Stabilized Cadmium Sulfide Nanoparticles Part I: Effect of Blend Composition and Nanoparticle Aggregation

2.1. Introduction

The need for new materials for computing, data storage, and information transfer has spurred a growing field of research into tuning material properties at the nano-scale. Metallic and semiconducting nanoparticles (quantum dots) are subject to quantum confinement and surface effects, with tunable, size-dependent properties that make them ideal candidates for structural elements in photonic devices. For real applications, however, the ability to control nanoparticle ordering on multiple length scales is essential since the overall properties of a photonic device are dependent on a combination of effects operating on different length scales.

"Bottom-up" techniques, including self-assembly and directed-assembly processes, have been recognized as efficient routes to multi-scale ordering of colloidal nanoparticles. As outlined in the previous chapter, many different strategies along these lines have been employed, including molecular recognition-based "bricks and mortar" self-assembly (where the "mortar" can be DNA, polymers[1-5], or metal ions[6,7,8], electrostatic and H-bonding –mediated assembly[910], deposition of nanoparticles onto colloidal surfaces[11,12], infiltration of nanoparticles into colloidal crystals[13], and assembly at the surface of liquid droplets[14]. However, a fundamental challenge of multi-scale engineering that remains to be overcome before effective control of optical properties via self- and directed-assembly can be realized is the control of particle ordering at all functional length scales. In existing studies, a number of factors preclude full realization of this goal, including irregularly-shaped aggregate structures and poor control of inter-particle distances within nanoparticle assemblies. In addition, changes in the ordering of colloidal nanoparticles are generally accompanied by changes in the environment of the

nanoparticle's surface, resulting in optical effects of different origins that are impossible to decouple.

As described earlier in the introduction, this thesis describes a new "multi-step" self-assembly approach to form photonic structures which are based on hybrid building blocks of CdS nanoparticles encapsulated in the cores of stable block ionomer micelles. The first step in the "multi-step" approach is the self-assembly of diblock copolymers to form block ionomer micelles (SA1); within each micelle core, a single CdS semiconducting nanoparticle is synthesized to yield the hybrid building block PS-CdS. Once SA1 has been completed, the stable PS-CdS building blocks are blended with block copolymer stabilizing chains (PS-*b*-PAA) in the organic solvent DMF; water addition induces the secondary self-assembly (SA2) step to form large compound micelles (LCMs). Finally, aqueous dispersions of LCMs will be slowly evaporated to induce formation of three-dimensional colloidal crystals in a tertiary self-assembly step (SA3). The resulting 3D hierarchical structures show order on multiple length sales, with the CdS nanoparticles protected in the cores of the PS-CdS block ionomer micelles during the second and third self-assembly steps, such that a constant surface environment is maintained for the photoluminescent nanoparticles.

The formation of large compound micelles (LCMs) upon addition of water to a blend of PS-CdS particles and PS-*b*-PAA stabilizing chains in DMF has many similarities to the formation of PS-*b*-PAA crew-cut micelles[15,16,17,18], along with important differences. For crew-cut micelle formation, single chains of PS-*b*-PAA are dissolved in an organic solvent which is thermodynamically "good" for both blocks (e.g. DMF). Water is then slowly added to the solution, resulting in a progressively poorer solvent for

the hydrophobic polystyrene block. At a critical water content (CWC), the PS blocks undergo microphase separation to form a micelle core surrounded by a corona of water soluble blocks. The interfacial free energy between the core and the surrounding solvent favours an increase in the aggregation number and micelle core size; however, this increase in aggregation number is ultimately limited by the increased stretching of PS chains inside the core, which must extend from the interface to the center of the core to maintain constant density. The entropic penalty of chain stretching therefore balances the lowering of interfacial tension with micelle growth, resulting in an equilibrium micelle size determined by an overall minimization of the free energy.

Similar to crew-cut micelle formation, the formation of large compound micelles (LCMs) in the SA2 step begins with the slow addition of water to a polymer solution in DMF, although in this case two components are present: PS-*b*-PAA chains and the PS-CdS micelles (with a CdS core and PS chains extending into solution). Just as in crew-cut micelle formation, a CWC exists above which PS chains phase-separate from the DMF/water mixture. Since the PS-CdS is the higher-molar mass component, it will phase separate first, defining the CWC of the mixture. Unlike the formation of crew-cut micelles, this is a macrophase separation process, with the hydrophobic PS-CdS particles self-assembling in the unfavourable DMF/water mixture to form a polymer-rich phase via spinodal decomposition, eventually breaking into droplets, or spherical clusters of PS-CdS particles (LCMs), which will grow in order to decrease interfacial energy. Once phase separation occurs, the PS-*b*-PAA chains will distribute themselves at the interface of the polymer-rich phase and the solvent mixture, lowering the interfacial free energy. However, growth of the spherical clusters, driven by a lowering of interfacial energy,

continues to be thermodynamically favourable, since PS chains of PS-*b*-PAA at the interface are not forced to stretch as the phase grows, as they are in the case of crew-cut micelles. Therefore, without the entropic penalty of PS stretching, there is no thermodynamically-determined equilibrium LCM size, with thermodynamics favouring continued LCM growth.

To consider a strategy for LCM size control (as demonstrated in this and subsequent chapters), one must therefore consider the important contribution of kinetics to LCM growth above the CWC. As water is added dropwise above the CWC, the thermodynamic driving force for phase separation and LCM growth is increased, as the DMF/water mixture becomes progressively poorer for PS. However, at the same time, DMF is progressively forced from the polymer-rich phase by osmotic pressure as more water is added, decreasing plasticization and lowering the mobility of the increasingly glassy polymer phase. Therefore, at some stage of water addition above the CWC, LCM growth becomes kinetically frozen on the time scale of further water addition, so that LCMs are locked into an average size that is determined by kinetics, rather than thermodynamics. We can therefore describe LCM formation and growth as occurring in a window of time on the scale of water addition between the CWC and the time at which the water content is high enough for LCMs to become effectively frozen. The average sizes of LCMs will therefore be influenced by experimental variables that influence the width of this kinetic window. Of these variables, the polymer concentration (which influences the CWC) and the rate of water addition will be investigated in Chapter 3 as experimental handles on LCM size control.

In this chapter, we describe the formation of LCMs from blends of the stabilizing chains PS(665)-*b*-PAA(68) hybrid building blocks designated PS-CdS1, formed from self assembly of the copolymer PS(145)-*b*-PAA(12). We intended initially to study the effect of the relative amounts of PS-CdS1 and the stabilizing chains on the resulting LCM populations. However, the unexpected presence of aggregates of PS-CdS1 within the DMF solutions before water addition was found to markedly affect LCM formation, as was demonstrated by pre-sonication and break-up of the aggregates. These experiments therefore provide additional insights into the influence of molar mass polydispersity of constituent building blocks on self-assembly and LCM formation in the SA2 step.

2.2. Experimental

2.2.1. Synthesis of Polystyrene-b-Poly(acrylic acid) (PS-b-PAA) Diblock Copolymer

Anionic polymerization was used to synthesize one of the polystyrene-*b*-poly(acrylic acid) (PS-*b*-PAA) diblock copolymers used for this study; the other diblock copolymer was purchased from Polymer Source Inc. The purchased and synthesized samples will be denoted as follows: PS(145)-*b*-PAA(12) and PS(665)-*b*-PAA(68), respectively, where the numbers in brackets indicate number-average degrees of polymerization for each block. The two diblock copolymers were used for different purposes: PS(145)-*b*-PAA(12) was used to prepare block ionomer reverse micelles (SA1 step) in which CdS nanoparticles were synthesized, resulting in the block copolymer stabilized nanoparticles, PS-CdS1. PS-CdS1 was then blended with the second copolymer PS(665)-*b*-PAA(68) in DMF for the preparation of LCMs by water addition (SA2 step), with the second copolymer serving as the stabilizing chains.

2.2.1.1. Purification of Styrene, tert-Butyl Acrylate, and α-Methylstyrene Monomers

A 500 mL two-necked round bottom distillation flask with a stir bar was flamed three times to remove any moisture. Approximately 5 g of CaH_2 and 350 mL of the desired monomer from the supplier were added to the flask and the solution was stirred overnight. The distillation flask that contained the monomer/CaH_2 mixture was attached using a distillation arm to a 500 mL two-necked receiving flask. Afterwards, the distillation flask was frozen using liquid N_2 and, once confirmed that it was frozen, the

receiving flask was flamed three times under active vacuum. The vacuum line was closed and the distillation flask with the frozen monomer was heated using a water bath (50 - 60°C) and the monomer was collected under static vacuum. Once all the monomer was collected in the receiving flask, the flow of N_2 was increased and in a quick movement the distillation arm and distillation flask were removed and the receiving flask was sealed under N_2 and stored in the freezer (-10°C). This first distillation step was required to remove any inhibitors present in the monomer from the supplier.

Just before their addition to the reaction flask, styrene and *tert*-butylacrylate, monomers had to be distilled a second time to remove all impurities. For the second distillation of styrene, a distillation apparatus consisting of a 50 mL round bottom flask attached by an arm to a 25 mL graduated receiving cylinder was used. The distillation apparatus was flamed under active vacuum and purged with UHP N_2 three times using Schlenk line techniques. After the distillation flask was cooled to room temperature, the prepared monomer "purifying agent" fluorenelithium solution (50 vol% of amount of styrene that will be added) was added to the distillation flask and the toluene solvent was evaporated off under active vacuum. The desired amount of the styrene monomer was added to the distillation flask and stirred for a few minutes. The styrene and fluorenelithium were frozen using liquid nitrogen, and then the arm and graduated receiving cylinder were flamed under active vacuum. The styrene was then warmed in a hot water bath and distilled under vacuum into the receiving cylinder, which was cooled using liquid N_2. The same procedure was used to purify the *tert*-butylacrylate a second time, with two differences: 1) the *tert*-butylacrylate was diluted with distilled toluene (70

vol% toluene relative to monomer) before addition of the purifying agent, and 2) triethyl aluminum was used as the purifying agent.

2.2.1.2. Synthesis of Polystyrene-b-Poly(tert-butyl acrylate) (PS-b-PtBA) Diblock Copolymer

Tetrahydrofuran (THF) was purified by refluxing over sodium benzophenone complexes under ultra high purity nitrogen (UHP N_2). The THF solution was a blue-violet colour indicating that the solvent was free of oxygen and moisture. The solution was then distilled and collected under UHP N_2.

The anionic polymerization was carried out under UHP N_2 atmosphere and all transfers were done using syringe and canula techniques. LiCl was added to a two-necked round bottom reaction flask with a 3-way stopcock that was greased with silicone-free grease and put in the oven overnight. The reaction flask was then removed from the oven and was flamed under vacuum on the Schlenk line then purged three times using repeated cycles of UHP N_2 and vacuum. Then the distilled THF was transferred under UHP N_2 to the reaction flask using a double-tip needle that had been previously flamed. Once all the THF was transferred and LiCl was dissolved, the reaction flask was again purged three times using repeated cycles of UHP N_2 and vacuum. Then a few drops of α-methylstyrene were added to the reaction flask and stirred for a few minutes. The solution was then titrated with *sec*-BuLi at room temperature until a light red colour was sustained indicating all impurities had been removed. The reaction flask was cooled to -78°C using an acetone/dry ice bath and the red colour was observed to fade. The

reaction mixture was again titrated to the end point to remove impurities then the desired amount of *sec*-BuLi was added to initiate the reaction.

Using a flamed canula, the distilled styrene was added to the reaction flask containing THF, LiCl and α-methylstyrene accompanied by vigorous stirring. As the styrene was being added the colour of the solution changed from red to yellow indicating polymerization of the styrene monomer; however, once all the styrene was consumed (within minutes), the solution changed back to the original red colour and the reaction was stirred for an additional 30 min. A 10 mL aliquot was removed from the polystyrene solution, in order to determine the molar mass and the degree of polymerization of the polystyrene block using size exclusion chromatography (SEC). To polymerize the second block, the desired amount of distilled *tert*-butylacrylate (*t*-BA) was added to the reaction flask using a flamed canula, accompanied by vigorous stirring. Once the *t*-BA was added, the red colour disappeared immediately. The polymerization was allowed to continue for another 30 min, and then a few drops of methanol (previously bubbled with UHP N_2) were added to terminate the polymerization. The block copolymer was recovered by precipitation into methanol, followed by drying overnight under vacuum at 70°C.

2.2.1.3. Characterization of PS-b-PtBA Diblock Copolymer

To characterize the length of the PtBA block, two different known concentrations of the diblock were prepared using CCl_4 as the solvent for quantitative FTIR analysis. Using a calibration curve (A_{1730} vs. [PtBA]) determined from various known concentrations of PtBA homopolymer for a particular FTIR solution cell, the FTIR

absorbance at 1730 cm^{-1} was used to determine the concentration of PtBA in the diblock copolymer solution:

$$[\text{PtBA}] = A_{1730}/0.1891 \text{ g}^{-1} \text{ L} \qquad (2.1)$$

where 0.1891 g^{-1} L is the slope of the calibration curve. Then using [PtBA] and the total concentration of diblock copolymer in $CHCl_3$, the weight fraction of the PtBA block was determined:

$$\textit{weight fraction}_{PtBA} = [\text{PtBA}]/[\text{PS-}b\text{-PtBA}] \qquad (2.2)$$

Then using the number-average molar mass, M_n, of the PS block from SEC, the composition of the copolymer was calculated using the following formulas:

$$M_n(\text{PS-}b\text{-PtBA}) = M_n(\text{PS})/(1- \textit{weight fraction}_{PtBA}) \qquad (2.3)$$

$$M_n(\text{PtBA}) = M_n(\text{PS-}b\text{-PtBA}) - M_n(\text{PS}) \qquad (2.4)$$

$$N_{PS} = M_n(\text{PS})/104 \text{ g/mol} \qquad (2.5)$$

$$N_{PtBA} = M_n(\text{PtBA})/128 \text{ g/mol} \qquad (2.6)$$

where N_{PS} and N_{PtBA} are number-average degree of polymerization for each block.

2.2.1.4. Hydrolysis of Polystyrene-b-Poly(tert-butyl acrylate) (PS-b-PtBA) to Polystrene-b-Poly(acrylic acid) (PS-b-PAA)

The diblock copolymer was hydrolyzed to form polystyrene-*b*-poly(acrylic acid) (PS-*b*-PAA) in the following manner: the previously dried PS-*b*-PtBA diblock copolymer was dissolved in 1,4-dioxane to make a 4% w/w solution. The clear, colourless solution was stirred for 30 minutes at room temperature. A 10-fold mole excess (relative to *t*-BA repeat units) of 37% HCl was added drop-wise to the stirred solution. The solution was refluxed at 101°C overnight and slowly cooled to room temperature over a period of 1 hour. The slightly brown, clear solution was concentrated to four times its initial concentration via rotary evaporation and precipitated into isopropanol. The white powder was separated by vacuum filtration and subsequently dried for two days under active vacuum at 65°C. FTIR was used to confirm hydrolysis by the complete loss of the 1120 cm^{-1} peak and a shortening and broadening of the C=O peak at ~1730 cm^{-1}.

2.2.1.5. Fractionation of Polystyrene-b-Poly(acrylic acid) (PS-b-PAA)

In order to remove most of the polystyrene homopolymer impurity present from killing during anionic polymerization, fractionation of the PS-*b*-PAA diblock copolymer was performed. The strategy here is to convert the PS-*b*-PAA diblock copolymer into high-molar mass reverse micelles by neutralizing the acid blocks in organic solvent, which can then be separated from the homopolymer fraction (which will not micellize) by addition of water and selective precipitation. The micelles can then be converted back to single chains of PS-*b*-PAA diblock copolymer by re-protonation of the poly(acrylic

acid) blocks. For the neutralization step, the PS-*b*-PAA diblock copolymer was dissolved in THF (5 wt%). NaOH was added in a 3-fold mole excess ratio relative to the acrylic acid content. The solution acquired a bluish colour as inverse micelles with a sodium acrylate core and a styrene corona formed. At this point, an aliquot was taken for SEC analysis, which showed two peaks: one at low elution time (high molar mass) for the inverse micelles, and one at high elution time (low molar mass) for the homopolymer. The inverse micelle solution was stirred and water was added drop-wise until the solution remained turbid for several minutes after the addition of the last drop. At this point the solution was left to stand overnight. Two layers were found; the top layer contained the homopolystyrene while the bottom layer contained the inverse micelles, which precipitated and settled to the bottom. After removal of the top layer, the bottom layer was dissolved by addition of THF, and SEC analysis was performed again. The process was repeated until SEC showed mostly the peak of the micelles and relatively little of the homopolymer: for the PS(665)-*b*-PAA(68) it took two fractionation steps to achieve 95 wt% micelle / 5 wt% homopolymer by SEC peak integration.

Once the homopolystyrene was removed, the micelles were converted back to PS-*b*-PAA single chains by stirring the inverse micelles in a mixture of 15 vol% acetic acid, 5 vol% deionized water and 80 vol% THF overnight followed by precipitation into a mixture of 95 vol% methanol, 4 vol% deionized water and 1 vol% HCl. This procedure was repeated until there was no micelle fraction detected by SEC.

2.2.2. Preparation of Block Copolymer-Stabilized CdS Nanoparticles (PS-CdS1)

The diblock copolymer used to prepare PS-CdS1 was PS(145)-*b*-PAA(12) purchased from Polymer Source Inc. This copolymer was dissolved in a 90/10 (v/v) benzene/methanol mixture to a concentration of 2 wt% and stirred for 3 hours. A cadmium acetate solution in methanol (0.25 M) was prepared and 1.5 moles of CdAc were added for every 1 mole of acrylic acid groups in a continuous flow then stirred overnight. The next morning the solution consisting of micelles with poly(cadmium acrylate) (PACd) cores and polystyrene (PS) coronal chains (PS-*b*-PACd) was freeze-dried overnight, removing all the solvent, to recover the kinetically-frozen reverse micelles as a white powder; the powder was dried in the vacuum oven overnight at 70°C with active vacuum. To remove excess unbound cadmium acetate, the sample was washed 7 times with methanol and the filtrate was tested with aqueous Na_2S solution; yellow precipitate in the filtrate indicated unbound Cd^{2+} ions by formation of bulk CdS. The sample was washed until three consecutive tests of the filtrate revealed no yellow colour. After the sample was washed, the white powder was dried for two nights at 70°C under active vacuum.

Once methanol was removed from the micelle sample, it was placed in a humidity chamber at 70°C for one week. When the sample was removed from the humidity chamber it was directly placed under an atmosphere of "wet" H_2S. The H_2S was bubbled through water at room temperature and then into the sample chamber for 10 hours, then the line and sample chamber were flushed with N_2 for 1 hour. The resulting powder was yellow in colour, indicating formation of CdS, and was removed and dried under ambient

conditions overnight in a fumehood, then dried overnight under active vacuum (with no heat) to remove any residual H_2S. A second neutralization step was then performed by dissolving the yellow powder in THF (2 wt%) and then two moles of 0.25 M CdAc were added for every mole of acrylic acid groups and stirred overnight. The yellow powder was recovered by precipitation into methanol, and then washing repeatedly with methanol. To remove excess unbound cadmium acetate, the sample was washed several times with methanol, testing the filtrate with Na_2S solution, as described previously, and then dried under vacuum at 70°C under active vacuum overnight. The resulting block copolymer-stabilized CdS nanoparticles, consisting of a CdS core, a poly(cadmium acrylate) surface layer, and a polystyrene corona (see Figure 1.8 in Chapter 1), is designated PS-CdS1. The characterization of these hybrid nanoparticles will be described in the Results and Discussion section.

2.2.3. Preparation of Large Compound Micelles (LCMs) in DMF/Water Mixtures

The various large compound micelles (LCMs) described in this chapter were prepared using the following general procedure: PS(665)-*b*-PAA(68), used as stabilizing chains, and PS-CdS1 were each dissolved in separate DMF solutions to the same initial polymer concentration, C_0, and both solutions were stirred overnight at room temperature. The DMF used was 99.9+ % HPLC Grade, $H_2O < 0.03$ wt%; the bottle was sealed with Teflon when not in use. These solutions were then mixed in different ratios to obtain various blend solutions with the same initial polymer concentration C_0 and different compositions designated by the weight fraction of PS-CdS1 (f) relative to the total polymer content. For experiments described in this chapter, C_0 = 1 wt% polymer

and f = 0, 0.1, 0.3, 0.5, 0.7, 0.9; the room temperature during water addition was monitored and found to be 22.5 ± 1°C.

To initiate LCM self-assembly within each of these blend solutions, deionized water was added to 5 g of each solution (Scheme 2.1) with continuous rapid stirring. The rate of water addition ($rate_{water}$) was an important factor in these experiments and was controlled for a given experiment by adding 20 μL drops every 10 seconds to give $rate_{water}$ of 2.4 wt% / min which is relative to the initial weight of solution (5 g) before water was added. For all experiments, the formation of LCMs was indicated by an increase of turbidity by eye at a specific critical water content (CWC). Addition of water was continued with stirring to 25 wt%, after which the LCM solutions were stirred overnight. The solutions were then dialyzed against deionized water for 5 days, changing the deionized water every day. This removed all DMF from the LCM samples and resulted in LCMs dispersed in pure water.

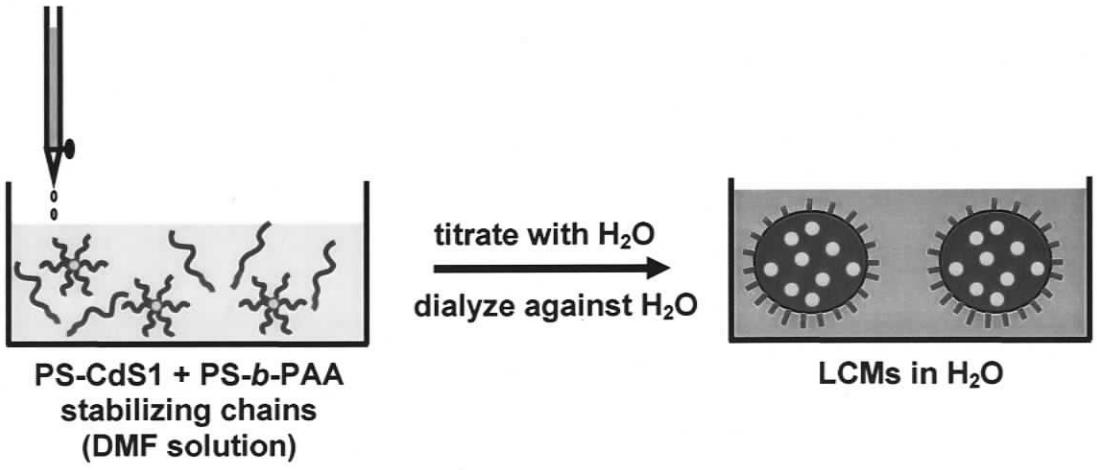

Scheme 2.1. Secondary self-assembly (SA2) in DMF/water mixtures: large compound micelle (LCM) formation.

2.2.4. Size-Exclusion Chromatography (SEC)

All SEC measurements were performed using a Viscotek Model 302 liquid chromatography system equipped with refractive index (RI), low-angle light scattering (LALS, $\theta = 7°$), right-angle light scattering (RALS, $\theta = 90°$), and UV detectors. THF was used as the eluent at a flow rate of 1 mL/min and the column temperature was set at 35°C. All polymer solutions were filtered through membrane filters with a nominal pore size of 0.45 μm before injection into the SEC column. The data were collected and analyzed on a Dell Dimension 2300 computer with appropriate SEC software from Viscotek. Two ViscoGEL HR High Resolution Columns (styrene-divinyl benzene columns) in series were used: G3000 HR 60k GMHHR-M Mixed Bed 4 M columns.

Molar mass were calculated from SEC data using an algorithm from Viscotek, which relies on low-angle light scattering detection from a 670 nm diode laser source. This utilized the fundamental Zimm equation for light scattering from polymer solutions:

$$\frac{Kc}{\Delta R_\theta} = \frac{1}{M_w P(\theta)} + 2A_2 c \qquad (2.7)$$

where R_θ is the excess Rayleigh scattering ratio, $P(\theta)$ is the particle scattering factor, M_w is the weight-average molar mass of the sample, A_2 is the second virial coefficient, c is the polymer concentration and K is a composite of optical and fundamental constants. The excess Rayleigh ratio is the ratio of light scattered from the solution in excess of solvent scattering at an angle of detection θ, I_θ, with respect to the incident beam

intensity, I_0 : $R_\theta = kI_\theta/I_0$, where k is an instrumental constant. In the typical Zimm plot approach, M_w is analyzed by detecting scattered light for each concentration at a series of angles, followed by extrapolation to $\theta = 0$, where the scattering form factor $P(\theta) = 1$. By contrast, the present Viscotek LALS monitors light scattered at a single low-angle as the sample is eluted; irrespective of particle shape, $P(\theta)$ is very close to 1 for an angle of detection of $\theta = 7°$, so that M_w can be calculated without multi-angle extrapolation.

2.2.5. UV-Vis Absorption and Photoluminescence Measurements

Absorption spectra of PS-CdS1 were recorded on a Cary 50-scan UV-Vis spectrophotometer using samples dissolved in spectroscopic grade toluene with pure spectroscopic grade toluene subtracted as the background. Static fluorescence measurements were recorded on an Edinburgh Instruments FLS 920 instrument equipped with a Xe 450 W arc lamp and a red sensitive PMT (R928-P). For typical measurements of fluorescence, the PS-CdS1 samples were dispersed in spectroscopic grade toluene at concentrations such that the measured absorbance at 400 nm was less than 0.1; this is to keep the concentration low enough so that the auto-absorption effects were minimized. To obtain the final fluorescence spectrum of PS-CdS1, the spectrum of the solvent (spectroscopic grade toluene) was subtracted. The fluorescence spectra were recorded at 1 nm spectra resolution, $\lambda_{ex} = 400$ nm using a 425 nm filter.

2.2.6. Dynamic Light Scattering

All DLS experiments were carried out on a Brookhaven Instruments photon correlation spectrometer equipped with a BI-200SM goniometer, a BI-900AT digital

autocorrelator, and a Melles Griot He-Ne Laser (632.8 nm) with maximum power output of 75 mW. To ensure the accuracy of DLS measurements, great care was taken to eliminate dust from the samples.

For DLS characterization, spectroscopic grade DMF was filtered through 2 membrane filters connected in series with 0.20 μm nominal pore size; stock solutions of PS-CdS colloids dispersed in DMF with concentration of ca. 5 mg/mL were filtered through 2 membrane filters connected in series with 0.45 μm nominal pore size. All scintillation vials were thoroughly cleaned with filtered DMF, and the stock solution of the PS-CdS1 colloids was filtered into the dust-free scintillation vials. Successive dilutions of the colloids were carried out by adding known quantities of filtered DMF. DLS measurements were conducted at 1 angle: 90° and a diluted concentration of 2.5 x 10^{-3} g/mL. For each experiment, 3 repeat measurements of the autocorrelation function were obtained. All DLS measurements were conducted at 23°C.

2.2.6.1. Basic Theory of DLS:

Dynamic light scattering (DLS) allows the detection of quick changes in the scattered light intensity caused by solution density changes. These changes are a result of Brownian motion of particles in solution, and can be investigated to determine the diffusion coefficient, D_0, of the particles. Using the Stokes-Einstein relation, the diffusion coefficient can subsequently be used to calculate the hydrodynamic diameter (d_h), which is a measure of particle size in solution including any solvent molecules that move with the particle[19].

The fundamental quantity measured in a DLS experiment is the intensity autocorrelation function, $G_2(\tau)$, which in a very dilute solution of monodisperse particles, is an exponentially decaying function of the delay time, τ. The intensity autocorrelation function can be linked to the normalized electric field autocorrelation function, $g_1(\tau)$, in the following manner:

$$G_2(\tau) = B(1 + \beta| g_1(\tau) |^2) \qquad (2.8)$$

where B is the measured baseline of the decaying autocorrelation function and β is the consistency factor which is used as a modifiable factor in the data investigation. If the system is monodisperse and the particles are not interacting,$| g_1(\tau) |$ is also simple and a single exponential function and can be expressed as:

$$| g_1(\tau) | = \exp(-\Gamma\tau) \qquad (2.9)$$

where Γ is the relaxation rate of the decaying autocorrelation function with units of s^{-1}. Γ can be related to the diffusion coefficient, D (which has units of m^2s^{-1}), as follows:

$$\Gamma = Dq^2 \qquad (2.10)$$

where q is the scattering vector and is expressed as:

$$q = (4\pi n/\lambda) \sin(\theta/2) \qquad (2.11)$$

where n is the refractive index of the solvent, λ is the wavelength of the incident light, and θ is the scattering angle.

It is usually observed that the experimental autocorrelation function is not a single exponential function and that there is a distribution of relaxation rates due to a distribution of particle sizes in solution. Many techniques of analyzing autocorrelation functions consisting of a distribution of relaxation rates have been utilized and two specific methods are used in this thesis: 1) the cumulant method and 2) CONTIN analysis.

First, the data were fitted by the method of cumulants developed by Koppel, using the Brookhaven correlator software. In this method, the autocorrelation function is expanded about a z-average relaxation rate, $(\ \bar{\Gamma}\ )_z$. The result is a polynomial expansion in the delay time with cumulants (moments about $(\ \bar{\Gamma}\ )_z$) as the restrictions to be fitted. For polydisperse, point like, isotropic particles lacking intermolecular interactions the expansion may be written as follows:

$$|g_1(\pi)| = \text{expt}\ \{-\ \bar{\Gamma}\tau + (\mu/2!)\tau^2 + \ldots\} \qquad (2.12)$$

where $\bar{\Gamma}$ is the intensity (I)-weighted mean relaxation rate and μ is the second moment of the distribution of relaxation rates. The ratio $\mu / (\ \bar{\Gamma}\ )_z^2$ is used to calculate the width of the intensity distribution of relaxation rates, which is related to the size polydispersity of the sample. Using $(\ \bar{\Gamma}\ )_2$, a z-average effective diffusion coefficient, D_T, is determined from equation 2.10, then an effective z-average hydrodynamic diameter, d_h, is calculated using the Stokes-Einstein equation:

$$D_T = k_B T / 3\pi\eta d_h \qquad (2.13)$$

where k_B is Boltzmann's constant, T is the temperature, and η is the viscosity of the solvent. Due to frictional and thermodynamic interparticle interactions, the effective hydrodynamic diameter d_h is not always equal to the true hydrodynamic diameter for an individual non-interacting particle, d_0. To determine d_0, the effective diffusion coefficient is measured from cumulant analysis for solutions of various concentrations and then extrapolated to infinite dilution ($c = 0$) to determine the true diffusion coefficient, D_0. D_0 is then used to calculate d_0 using the Stokes-Einstein relation (equation 2.13).

The second method used in this thesis to determine the hydrodynamic diameter is CONTIN analysis using the Brookhaven software. This method, involves an inverse LaPlace transform to determine $G(\Gamma)$, the distribution of decay rates, using the relation:

$$| g(t) | = \int \Gamma G(\Gamma) \exp(-\Gamma\tau)\, d\ln\Gamma \qquad (2.14)$$

Unlike cumulant analysis, CONTIN does not assume a single narrow distribution of decay rates, and is therefore sensitive to the pressure of multiple populations of different sizes in the sample.

2.2.7. Transmission Electron Microscopy

Transmission electron microcopy (TEM) of various aqueous LCM colloids was performed on a Hitachi H-700 electron microscope, operating at an accelerating voltage of 75 kV. LCMs in water were diluted to a concentration of 0.5 mg/mL and then a 10 μL drop was deposited on a carbon coated formvar 300 mesh copper grid and then shadowed with Pt/Pd wire for imaging. Also, images were taken of the same solutions without Pt/Pd shadowing, in order to characterize the LCM internal structure.

2.3 Results and Discussion

2.3.1. Synthesis and Characterization of Polystyrene-b-Poly(acrylic acid) (PS-b-PAA) Diblock Copolymer

As mentioned in the experimental section, anionic polymerization was used to synthesize the diblock copolymer, polystyrene-*b*-poly(*tert*-butylacrylate) (PS-*b*-PtBA), which was the precursor for the PS-*b*-PAA copolymer used as stabilizing chains for LCM formation. The number-average and weight-average molar mass of both the PS block and the final diblock copolymer were determined using size-exclusion chromatography (SEC) with light scattering and refractive index detectors. We determined the molar mass of the polystyrene (PS) block by injecting the homopolymer sample removed from the reaction flask prior to addition of the second monomer. The resulting SEC chromatogram of PS(665) is shown in Figure 2.1, with the number-average degree of polymerization calculated from M_n as determined by SEC. In addition, Figure 2.1 shows the SEC chromatogram for the final diblock copolymer sample, PS(665)-*b*-PtBA(68), where the degree of polymerization of the second block was determined from FTIR data, as described in the experimental section. Both SEC chromatograms show single narrow peaks, indicating low polydispersities for both the PS block and the copolymer. The peak elution time of the copolymer (13.28 min) is just slightly greater than the elution time of the PS block (13.17 min) as expected considering that the PtBA block is short and should not increase the size of the copolymer in solution to a great extent. From SEC, the PS(665)-*b*-PtBA(68) copolymer has a polydispersity of P.I. = 1.01

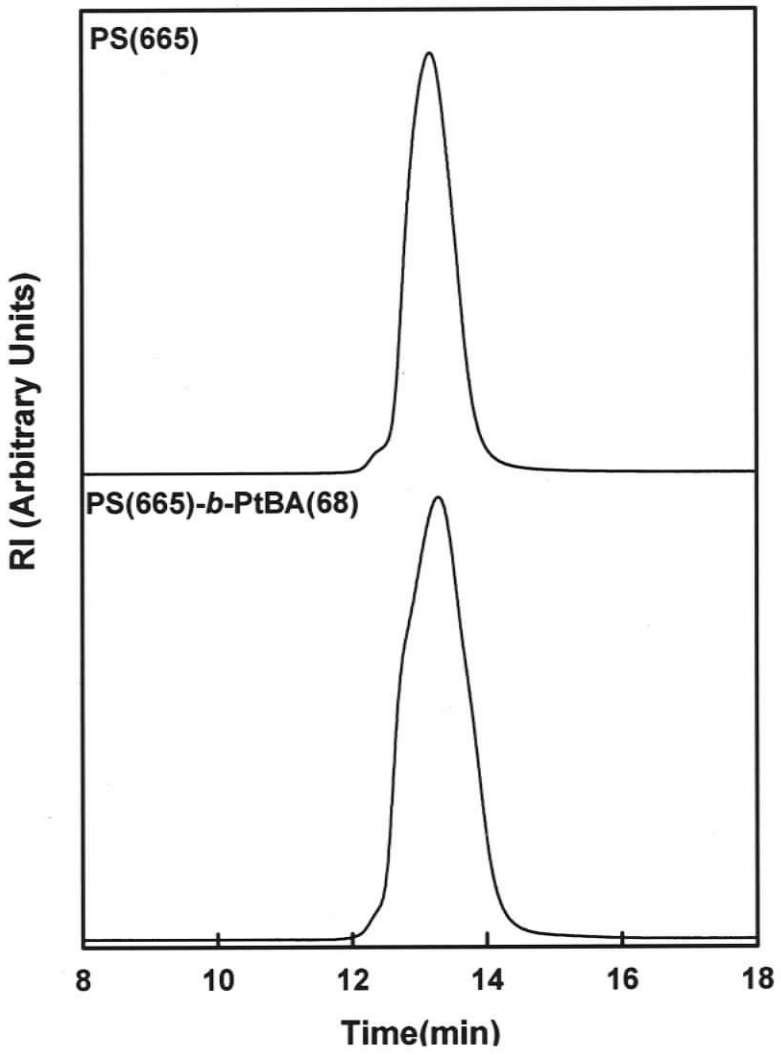

Figure 2.1. SEC chromatograms of the PS block and the diblock copolymer PS-*b*-PtBA in THF for the PS(665)-*b*-PtBA(68) copolymer prepared by anionic polymerization.

Once the lengths of both blocks had been determined, the PtBA block was converted to poly(acrylic acid) (PAA), and this was followed by FTIR as shown in Figure 2.2. The FTIR spectra in Figure 2.2 show the complete conversion of the ester moieties of the diblock copolymer PS-*b*-PtBA to the acid form PS-*b*-PAA; after the hydrolysis procedure, the single absorption band at 1730 cm^{-1}, which is due to the C=O stretch of the ester, converts to two peaks which are characteristic of the C=O stretch of carboxylic acid. Further evidence of the complete conversion from the ester to the carboxylic acid is the disappearance of the band at 1150 cm^{-1} which is characteristic of the C—O stretch of the ester.

2.3.2. Fractionation of Polystyrene(665)-b-PAA(68) Diblock copolymer.

One inherent disadvantage of anionic polymerization is that it is very sensitive to impurities that could be present in the system such as moisture and air. This could result in some PS homopolymer in the sample due to killing of living chains before addition of the second monomer. We attempted to remove the PS homopolymer from the hydrolyzed PS-*b*-PAA using the fractionation procedure described in the experimental section. As mentioned earlier, this process begins with conversion of the PS-*b*-PAA diblock copolymer into high-molar mass reverse micelles by neutralizing the acid blocks with NaOH in organic solvent, and then removing the homopolymer by several steps of selective precipitation; this process was followed using SEC. As shown in Figure 2.3, the original PS-*b*-PAA diblock copolymer which is dissolved in THF before

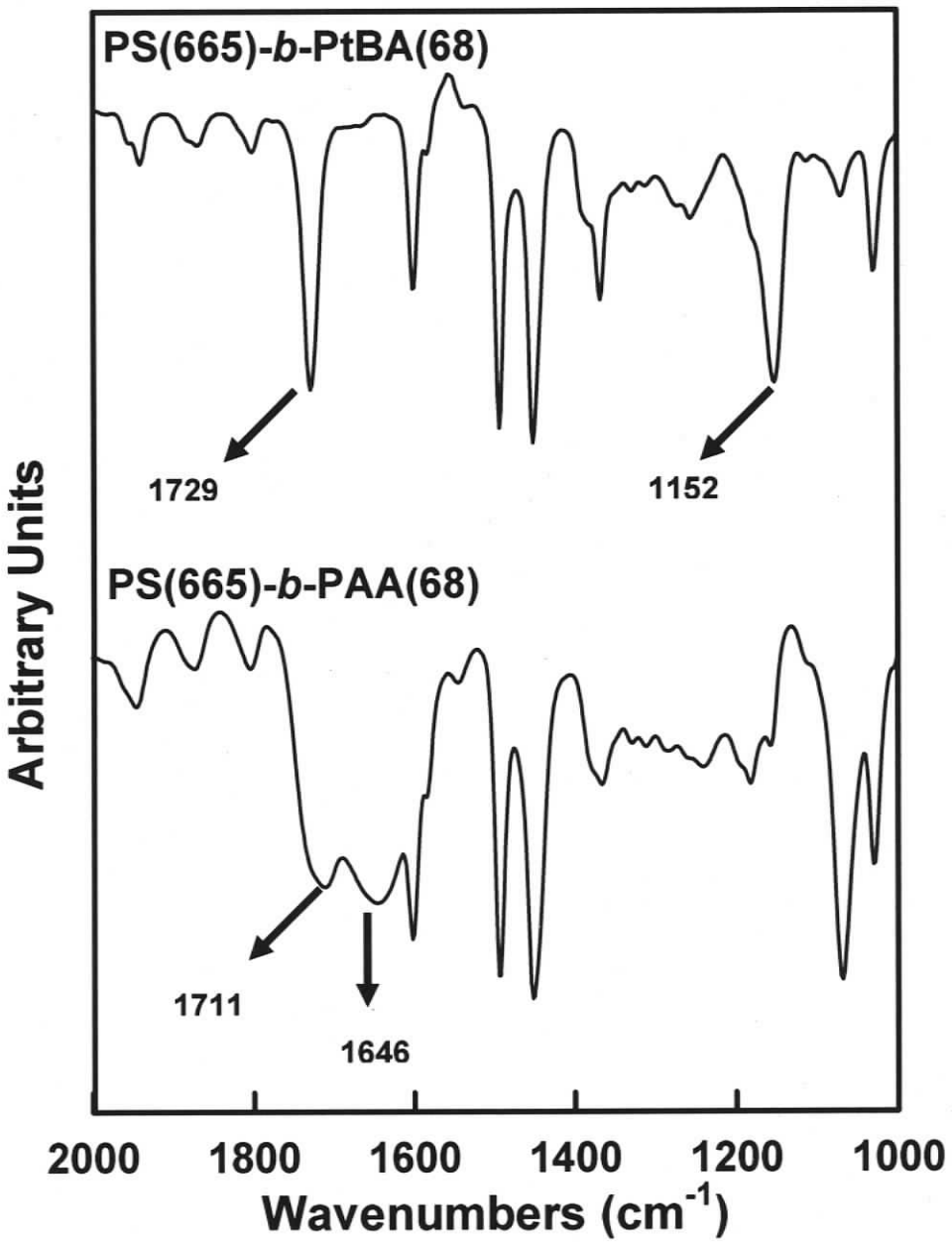

Figure 2.2. FTIR of poly(styrene)-*b*-poly(*tert*-butylacrylate) (PS-*b*-PtBA) and the poly(styrene)-*b*-poly(acrylic acid) (PS-*b*-PAA) sample resulting from hydrolysis of the ester form of the copolymer. Both spectra were obtained from neat films on KBr windows.

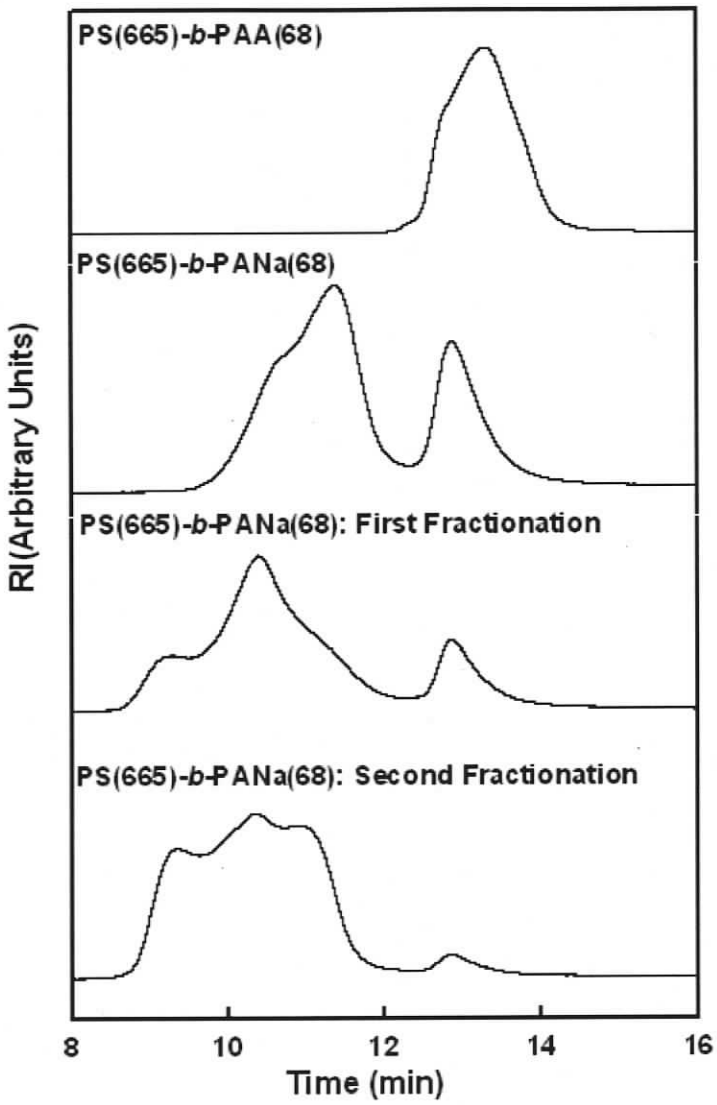

Figure 2.3. SEC chromatograms monitoring the fractionation of diblock copolymer polystyrene-*b*-poly(acrylic acid) (PS-*b*-PAA). The diblock copolymer PS-*b*-PAA is converted to high molecular-weight reverse micelles by first dissolving it in THF then neutralizing with NaOH, resulting in polystyrene-*b*-poly(sodium acrylate) (PS-*b*-PANa). The SEC shows two peaks: one at low elution time (high-molar mass) for the reverse micelles, and one at high elution time (low-molar mass) for the homopolymer. The homopolymer was mostly eliminated by selective precipitation by water addition in two fraction steps.

any fractionation comes out as a single peak. It is important to note that the homopolymer PS and diblock fractions will elute at nearly the same elution times and so are not resolved by SEC. However, once the diblock copolymer is neutralized with NaOH (PS-*b*-PANa), two peaks are seen: one at low elution time (high molar mass) which is due to reverse micelles of polystyrene-*b*-poly(sodium acrylate) (PS-*b*-PANa) and one at high elution time (low molar mass) which is due to the PS homopolymer that is present in the system. To remove the PS homopolymer, water was added slowly to precipitate selectively the higher-molar mass fraction (reverse micelles) and this fraction was allowed to settle then recovered and redissolved by addition of THF, and analyzed by SEC. This selective precipitation process was repeated. As shown in Figure 2.3, the peak that characterizes the PS homopolymer decreases and the reverse micelle peak increases with each fractionation attempt. As well, the micelle peak is found to broaden in the process of fractionation presumably due to supermicellar aggregate formation with water addition. Integration of the SEC peaks indicated that after two fractionation steps there was only 5 wt% of PS homopolymer remaining in the sample, compared to 31% prior to the first fractionation step.

After removing as much of the PS homopolymer as possible (subsequent fractionation steps did not reduce the amount of PS significantly), the reverse micelles were converted back to single chains; this was accomplished by reprotonating the PS-*b*-PAA in acidic medium and precipitation into a strong acid solution. Several such acid treatments were required to entirely break-up the reverse micelles as indicated by SEC

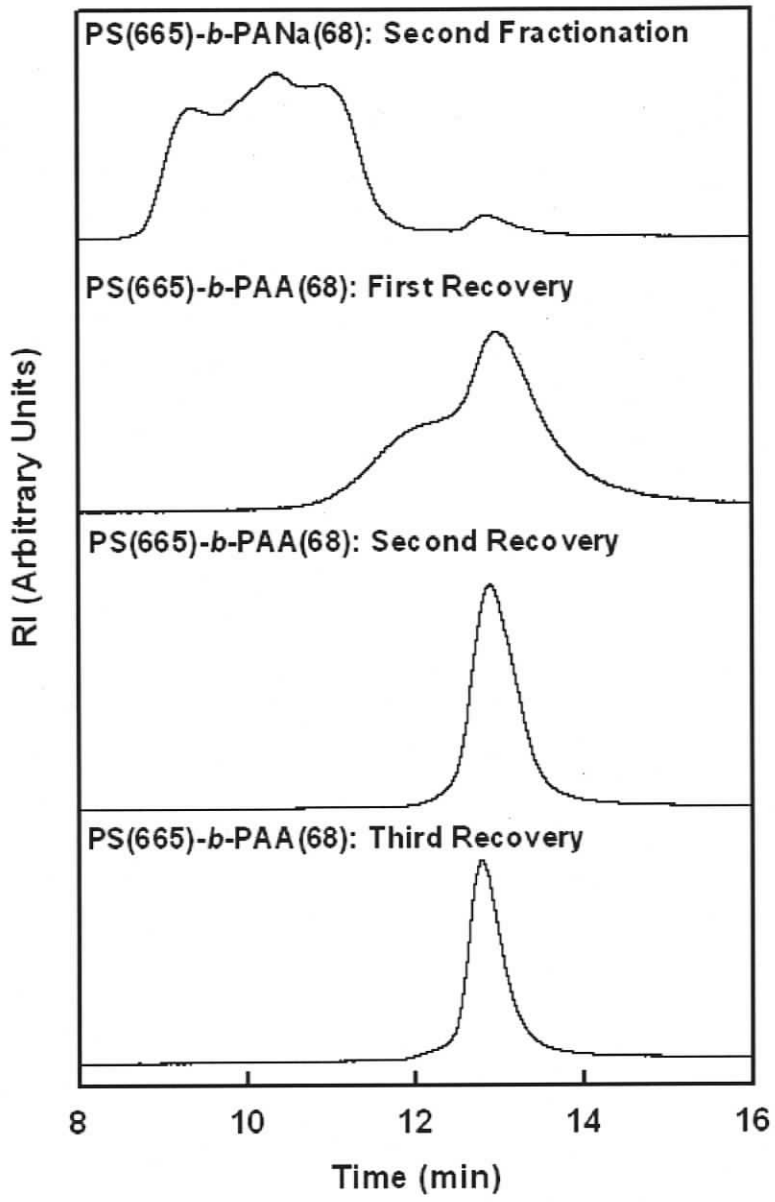

Figure 2.4. SEC chromatogram monitoring the conversion of the high molecular-weight reverse micelles of polystyrene-*b*-poly(sodium acrylate) (PS-*b*-PANa) back into single chains of polystyrene-*b*-poly(acrylic acid) (PS-*b*-PAA) by dissolving into an acetic acid solution, and stirring overnight, then precipitating into an HCl solution. This recovery procedure was repeated 3 times to complete the conversion.

(Figure 2.4). The first chromatogram shown in Figure 2.4 represents the sample following the last fractionation step which shows the micelle and the small PS homopolymer peaks. After one acid treatment (first recovery), the high-molar mass micelle peak has decreased considerably and the low-molar mass single chain peak has increased, indicating partial break-up of micelles into PS-*b*-PAA. The process in completed after two subsequent acid treatments (second and third recovery), after which a single, narrow copolymer distribution was obtained (Figure 2.4).

2.3.3. Characterization of Block Copolymer-Stabilized CdS Nanoparticles (PS-CdS1): SEC, UV-Vis, and Photoluminescence.

The diblock copolymer PS(145)-*b*-PAA(12), purchased from Polymer Source Inc, was used to prepare the block copolymer-stabilized CdS nanoparticles, PS-CdS1, as described in the Experimental section. Figure 2.5 shows SEC chromatograms of the PS-CdS1 sample in THF: one from the refractive index detector, RI, and the other from the low-angle light scattering detector, LALS. They both show broad peaks attributed to the polymer-coated quantum dots. The RI also shows a low-molar mass shoulder which is due to unmicellized copolymer or PS homopolymer impurity. By integration of the PS-CdS1 peaks, the combination of RI and LALS signals were used to determine the number-average molar mass of the copolymer (assuming that *dn/dc* was equivalent to PS in THF = 0.185). This gave M_n = 2.151 x 10^6 g/mol for PS-CdS1. Combining this number with the molar mass of PS(145)-*b*-PAA(12) single chains gave an estimated aggregation number of $Z = 105$. This value is a factor of 2 greater than the

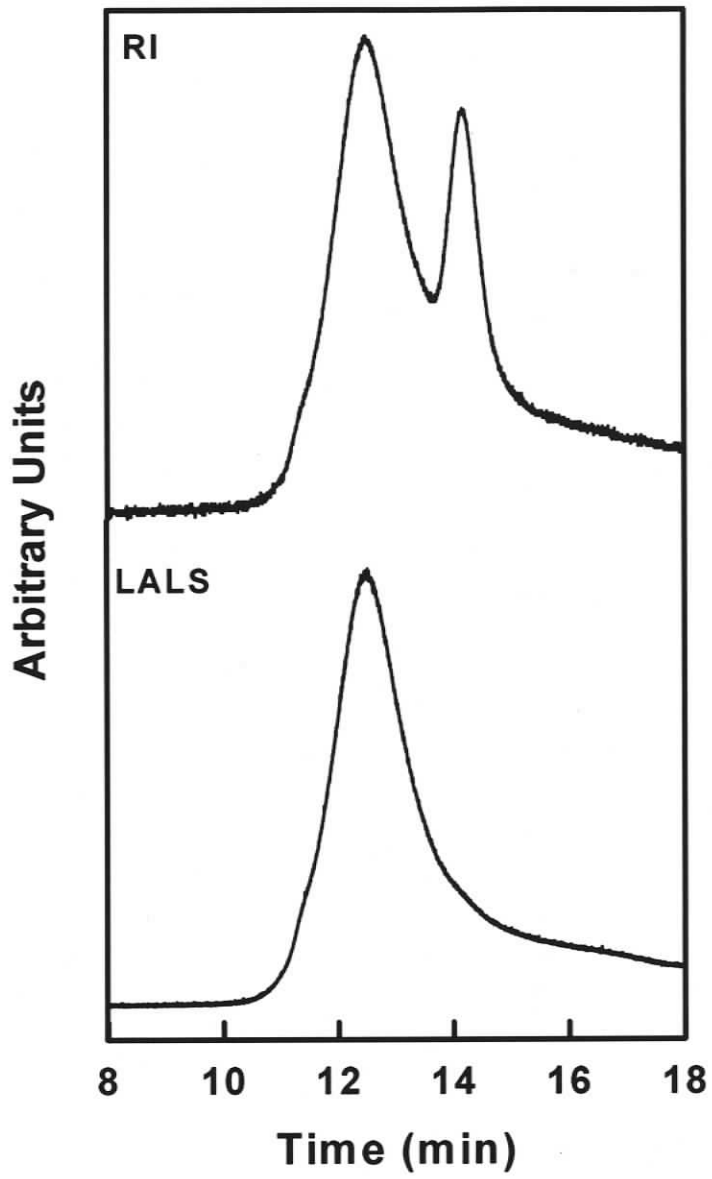

Figure 2.5. SEC of PS-CdS1 in THF solvent. The first chromatogram shows the refractive index (RI), the second chromatogram shows the low angle light scattering (LALS). The shoulder on the right of the RI is due to the PS homopolymer present in the system.

predicted aggregation number of PS(145)-*b*-PAA(12 from the empirically-determined scaling relation $Z = 8.9 \pm 1.9\ N_B^{0.68 \pm 0.24}$ for individual cadmium-neutralized reverse micelles ($Z \sim 50$ for $N_B = 12$)[20]. This suggests that PS-CdS1 in organic solvents may contain supermicellar aggregates of block copolymer-stabilized CdS nanoparticles. The presence of aggregates was further investigated by DLS as described in a later section.

In addition, we characterized the optical properties of quantum dots in PS-CdS1 using UV-Vis absorption and photoluminescence spectroscopy as seen in Figure 2.6. The UV-Vis absorption spectrum is attributed to CdS nanoparticles, and shows an exciton shoulder at ~450 nm with a threshold absorption at 482 nm as determined by extrapolating a tangent to the steepest part of the spectrum as shown in Figure 2.6. From the threshold absorbance ($\lambda_{\text{threshold}} = 482$ nm), we calculate the size of the CdS nanoparticles to be 4.8 nm using the formula: $d_{CdS} = 1 / (0.1338 - 0.0002345\lambda_{thresh})$[21,22]. The CdS photoluminescence spectrum for excitation at $\lambda_{ex} = 400$ nm, shows a broad red-shifted emission band centered at 625 nm, which is attributed to recombination from a distribution of deep trap states localized at the quantum dot surface. A very weak band-edge emission at around 464 nm is also visible which is attributed to recombination from band-edge or near band-edge states. The low intensity of band-edge emission compared to trap state emission suggests a high density of the surface trap states in PS-CdS1 and a correspondingly high probability of crossover to these traps once an exciton is created by light absorption.

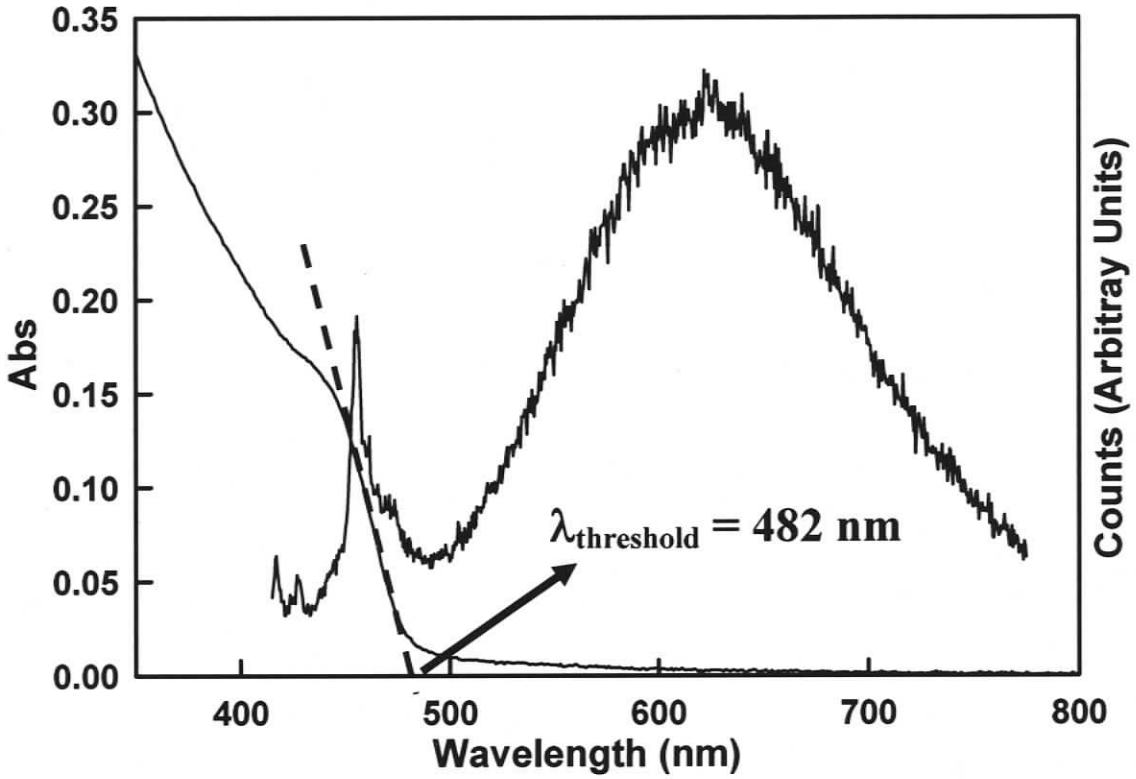

Figure 2.6. Absorbance and photoluminescence of PS-CdS1 dissolved in spectroscopic grade toluene (λ_{ex} = 400 nm). The core size of the CdS was determined to be d_{CdS} = 4.8 nm from $\lambda_{threshold}$ = 482 nm determined from the absorption spectrum. For the photoluminescence spectrum, the solvent (spectroscopic grade toluene) was subtracted. The photoluminescence spectra were recorded at 1 nm spectra resolution using a 425 nm filter.

2.3.4. Dynamic Light Scattering of PS-CdS1 and Sonication of Supermicellar Aggregates.

As mentioned in the last section, the aggregation number of PS-CdS1 determined from SEC (RI and LALS detectors) suggested the presence of supermicellar aggregates in organic solvents. This was confirmed by carrying out dynamic light scattering (DLS) measurements on PS-CdS1 in DMF at a concentration of 2.44 x 10^{-3} g/mL, which revealed two distinct peaks in the hydrodynamic diameter distribution determined from CONTIN analysis of the autocorrelation function (Figure 2.7) with a smaller-sized population centered at ~60 nm and a larger-sized population centered at ~160 nm. Separate cumulant analysis of the same autocorrelation function gives a mean effective hydrodynamic diameter of 99.5 nm.

The smaller size of ~ 60 nm is consistent with the size of individual reverse micelles from literature values[20]. The presence of a larger particle population together with individual PS-CdS1 particles therefore confirms the presence of aggregates. In order to attempt to break-up the aggregates, PS-CdS1 dispersions in DMF at 1.0 wt% polymer concentration were sonicated up to 1000 min; samples of the 1.0 wt% solution were removed, filtered and diluted to 2.7 x 10^{-3} g/mL for DLS analysis after various sonication times to follow the effect of sonication, using both cumulant (Figure 2.8A) and CONTIN (Figure 2.8B) analysis. Mean particle sizes from cumulant analysis clearly decreased from ~ 100 nm to ~ 50 nm with 1000 min

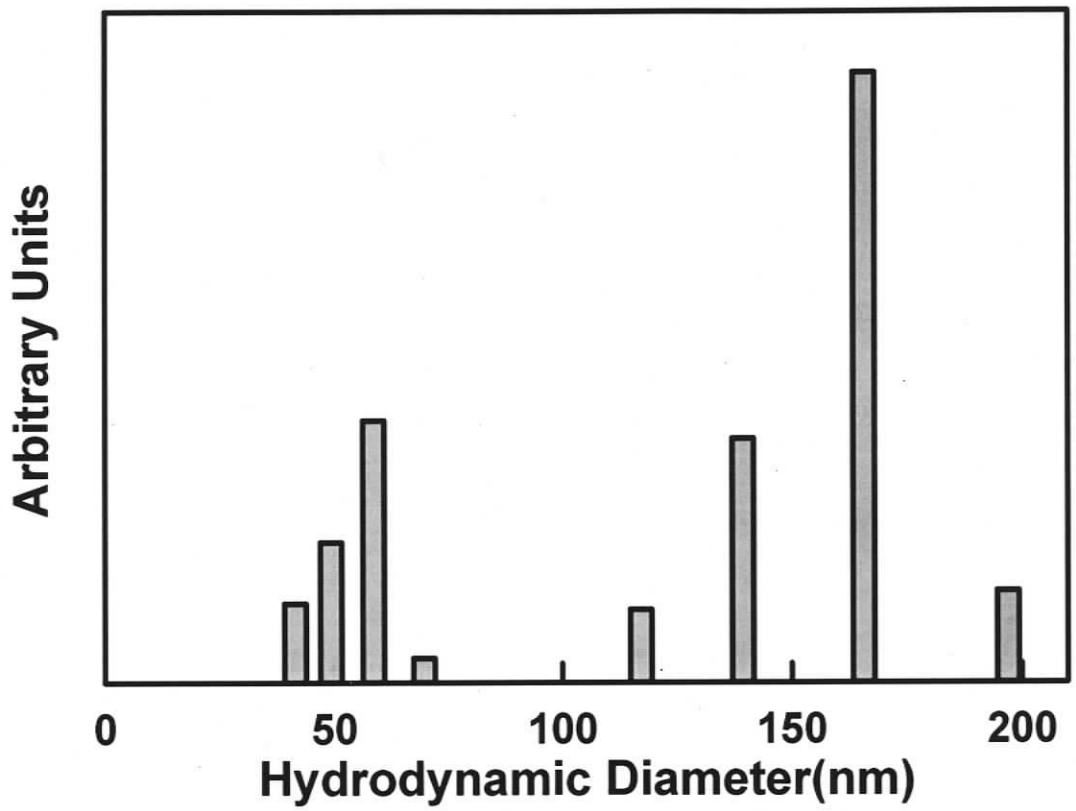

Figure 2.7. CONTIN analysis of dynamic light scattering (DLS) of PS-CdS1 in DMF clearly showing the two populations present in the system. The smaller-sized (~60 nm) population is unaggregated PS-CdS1, the larger-sized (~160 nm) population is the aggregated PS-CdS1. The mean effective hydrodynamic diameter from cumulant analysis of the same data is 99.5 nm.

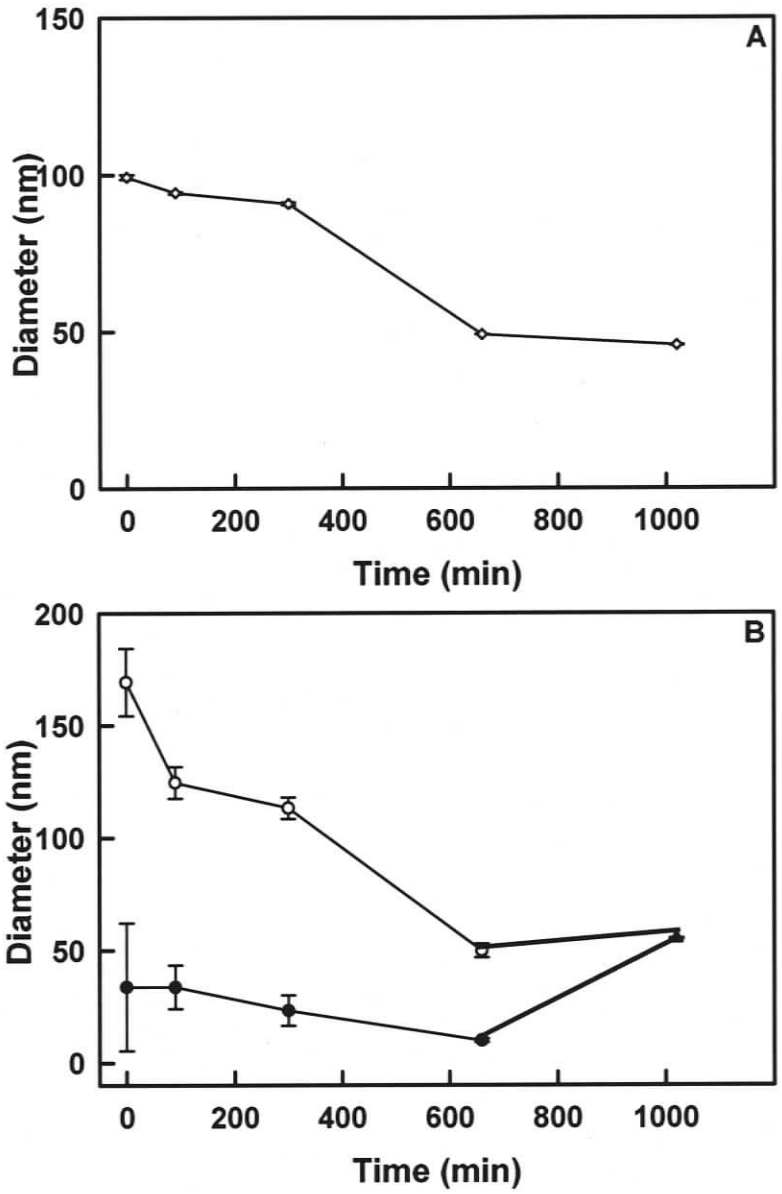

Figure 2.8. Monitoring the effect of sonication via dynamic light scattering (DLS) of PS-CdS1 in DMF: A) mean effective diameter from cumulant analysis, B) peak diameters from CONTIN for the two distributions, the open circles are the aggregated PS-CdS1 micelles, and the closed circles are the non-aggregated PS-CdS1 micelles.

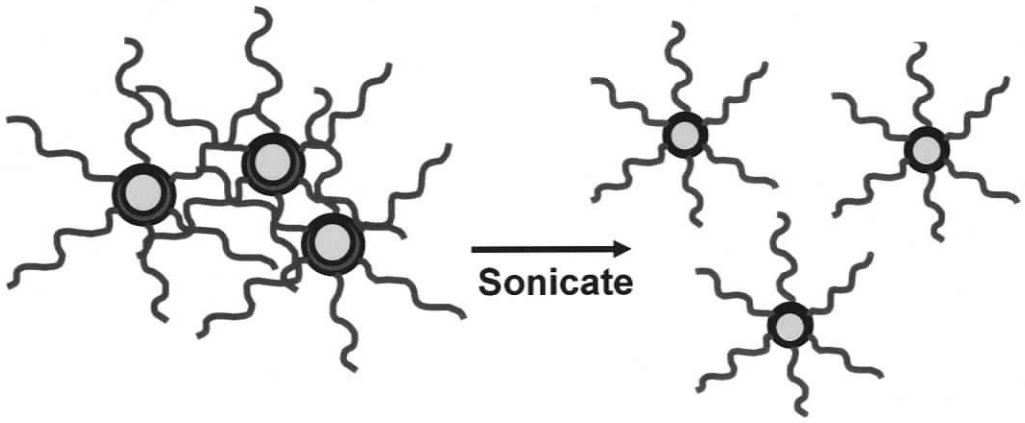

Scheme 2.2. A representation of sonication and break-up of PS-CdS1 aggregates.

sonication, with the sharpest drop in size between 200 and 600 min. CONTIN analysis of the two populations with various sonication times shows the larger particle size to steadily decrease while the smaller particle size remains constant, until CONTIN analysis reveals a single population at ~50 nm after 1000 min of sonication. Both cumulant and CONTIN analysis are therefore consistent with the break-up of aggregates into individual PS-CdS1 particles with sonication (Scheme 2.2). After 1000 min sonication, the 1 wt% solution of PS-CdS1 in DMF was allowed to sit overnight; DLS measurements carried out the next day showed no change in the particle size, suggesting that the break-up of aggregates was irreversible. This indicates that individual PS-CdS1 particles solubilized in DMF are thermodynamically stable and that aggregate formation was a kinetic phenomenon occurring at some stage in the PS-CdS1 preparation. We are not certain what caused aggregate formation, although it may in part be attributed to the relatively

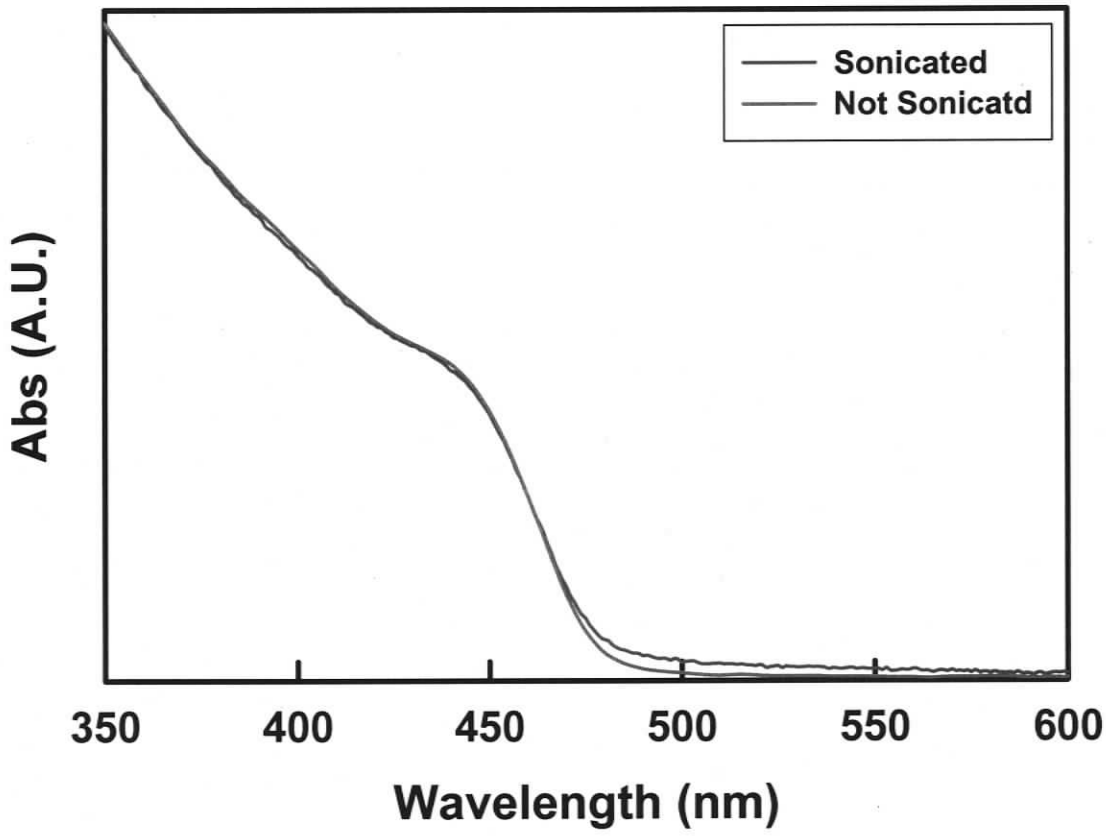

Figure 2.9. UV-Vis spectra of PS-CdS1 dissolved in DMF before and after 1000 min sonication.

short soluble blocks in the copolymer sample PS-(145)-*b*-PAA(12) used to prepare PS-CdS1.

It was important to determine that the sonication process only broke up the aggregates and did not result in break-up of the block copolymer-stabilized PS-CdS1 nanoparticles. This was confirmed by comparing UV-Vis spectra of PS-CdS1 before and after 1000 min sonication (Figure 2.9). The absorption threshold of CdS was not found to increase with sonication, indicating that the CdS nanoparticles did not ripen or agglomerate with sonication. This strongly indicates that the block copolymer stabilizing layer remained intact throughout the sonication procedure.

2.3.5. Preparation of Large Compound Micelles (LCMs) in DMF/Water Mixtures: No Pre-Sonication of PS-CdS1.

To understand the effect of composition (relative amount of PS-CdS1 and PS(665)-*b*-PAA(68) stabilizing chains) on the formation of large compound micelles (LCMs), a constant initial polymer concentration was used to prepare blend solutions in DMF, C_0 = 1 wt%, and the weight fraction of PS-CdS1 relative to the total polymer weight was varied: f = 0, 0.1, 0.3, 0.5, 0.7 and 0.9. For the initial experiments, blend solutions in DMF were prepared without prior sonication of PS-CdS1. From the discussion in the last section, these solutions therefore contain three species: PS-*b*-PAA stabilizing chains, individual PS-CdS1 particles and aggregates of PS-CdS1.

As described earlier, once the various solutions in DMF were prepared, water was added drop-wise at a rate of 20 μL every 10 seconds ($rate_{water}$ = 2.4 wt% / min). For all blend solutions, the onset of species turbidity of the clear yellow solution indicated the

critical water content and the start of SA2 self-assembly. The CWCs, as determined from the number of added water drops where increased turbidity was first observed by visual inspection, were calculated as a weight percentage of added water relative to the total weight of solution (including the added water). The resulting CWCs were as follows for the various C_0 = 1 wt% solutions: f = 0, CWC ≈ 9 wt%; f = 0.1, CWC ≈ 5 wt%; f = 0.3, CWC ≈ 3 wt%; f = 0.5, CWC ≈ 3 wt%; f = 0.7, CWC < 0.4 wt%; f = 0.9, CWC < 0.4 wt%. These data indicate a decrease in CWC with increasing PS-CdS1 content. This is an expected result, since CWC is known to decrease with both concentration and molar mass of the precipitating polymer[15,16,18,19,23,24], and an increase in f represents an increase in the concentration of the higher molar mass PS-CdS1 component.

Once the CWC was reached for each solution, water was continually added at the same rate to a total water content of 25 wt%. Continued water addition not only provides a stronger driving force for self-assembly (since PS-solvent interactions become less favourable) but also progressively slows the dynamics of self-assembly, as DMF is leached out of the aggregates. At some point of water addition above the CWC, the aggregates become kinetically frozen on the experimental time scale, a water content which Eisenberg and co-workers have determined to be between 8 and 11 wt% H_2O[23]. Therefore, at 25 wt% H_2O the aggregates were considered to be completely frozen; dialysis over several days against pure water was then used to remove residual DMF. We note that the f = 0.7 and f = 0.9 blends were found to undergo macroscopic precipitation with continued water addition above the CWC, and settled as a yellow powder to the bottom of the vial; this indicated an insufficient content of stabilizing chains to significantly slow the phase separation process, so that very large aggregates were

obtained which settled under gravity and therefore did not result in stable colloids. The f = 0.7 and f = 0.9 samples were therefore not studied further. However, stable turbid colloids were obtained for f = 0, 0.1, 0.3 and 0.5, even after several days of dialysis, and so these samples were further studied by TEM.

TEM of the dialyzed self-assembled blend solutions, C_0 = 1 wt%: f = 0, 0.1, 0.3 and 0.5, deposited onto carbon/formvar substrates from aqueous colloids are shown in Figure 2.10A, 2.10B, 2.10C and 2.10D, respectively. Prior to TEM imaging, the samples were shadowed with Pt/Pd using high temperature vacuum sputtering; this shadowing increases contrast between the particles and the substrate, and is responsible for the teardrop-shaped shadow oriented along the direction of sputtering. TEM images for the f = 0 and f = 0.1 blends (Figure 210A and B) show a single population of small particles, which are believed to be crew-cut micelles formed from the stabilizing chains of PS(665)-*b*-PAA(68). For the f = 0.1 sample, a very small number of larger particles were also observed in certain parts of the TEM grid, although their number fraction compared to the smaller particle population was insignificant. For the f = 0.3 sample (Figure 2.10C), two particle populations are clearly observed: a smaller particle population attributed to crew-cut micelles and a less numerous population of larger particles. TEM of the various samples without Pt/Pd shadowing (insets) allowed the internal structures of the various aggregates to be imaged, providing critical information on the nature of the different particle populations. For the f = 0.3 sample, the smaller particles appeared as homogenous circles, without internal structure, in the unshadowed TEM images, confirming that they do not contain CdS nanoparticles and are therefore crew-cut

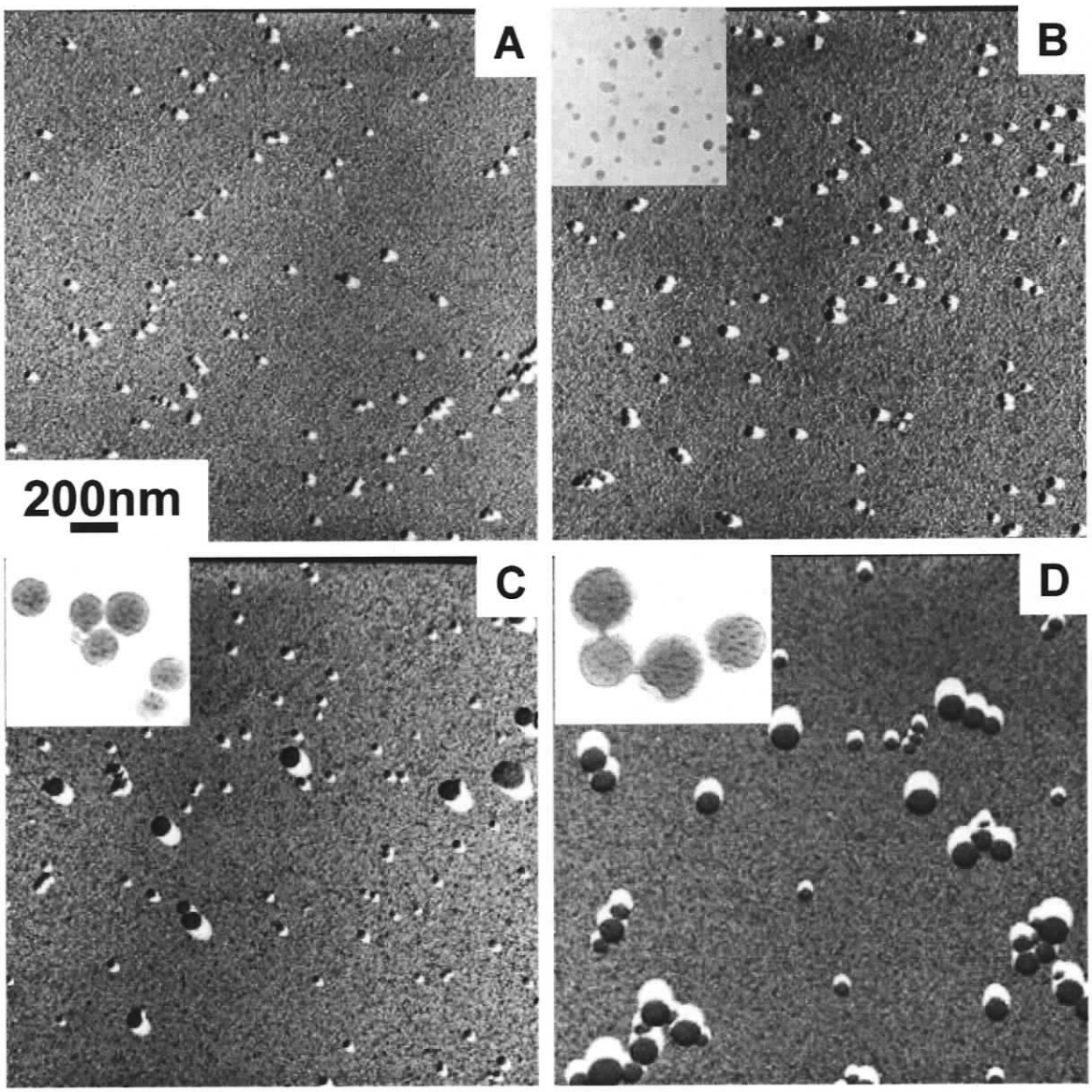

Figure 2.10. TEM images of colloids obtained from SA2 self-assembly from blends of PS(665)-*b*-PAA(68) and PS-CdS1 (without sonication). For all blends, C_0 = 1 wt%, $rate_{water}$ = 2.4 wt% / min: A) f = 0, B) f = 0.1, C) f = 0.3, D) f = 0.5. The insets show the TEM images without Pt/Pd shadowing.

micelles arising from self-assembly of the PS(665)-*b*-PAA(68) stabilizing chains alone. However, the larger particles show obvious internal structure (Figure 2.10C, inset), with a distribution of electron-dense spots throughout the spherical polymer matrix. The structure of these particles clearly suggests that they are LCMs, arising from phase separation-induced self-assembly of PS-CdS1, with PS(665)-*b*-PAA(68) stabilizing chains distributed at the particle's surface to lower interfacial energy and maintain a stable colloidal particle size before kinetic freezing (Scheme 2.3); since both LCM and crew-cut micelle populations are observed for $f = 0.3$, there is clearly an excess of stabilizing chains in this blend as the LCMs are formed, allowing formation of a separate crew-cut micelle population from residual PS(665)-*b*-PAA(68) chains with continued water addition. In contrast, when the relative amount of PS-CdS1 was increased to $f = 0.5$ (Figure 2.10D), a single, broad population of larger particles is observed, and TEM of the unshadowed sample revealed that only LCMs were present (inset). This indicates a critical ratio of PS-CdS1 and stabilizing chains ($f \approx 0.5$) for the current system in order to obtain a single population of stable LCM particles: for $f < 0.5$, we have an excess of stabilizing chains and form mostly small crew-cut micelles (Figures 2.10B and 2.10C); for $f > 0.5$ our experiments have shown that the relative amount of stabilizing chains is insufficient to result in a stable LCM colloid.

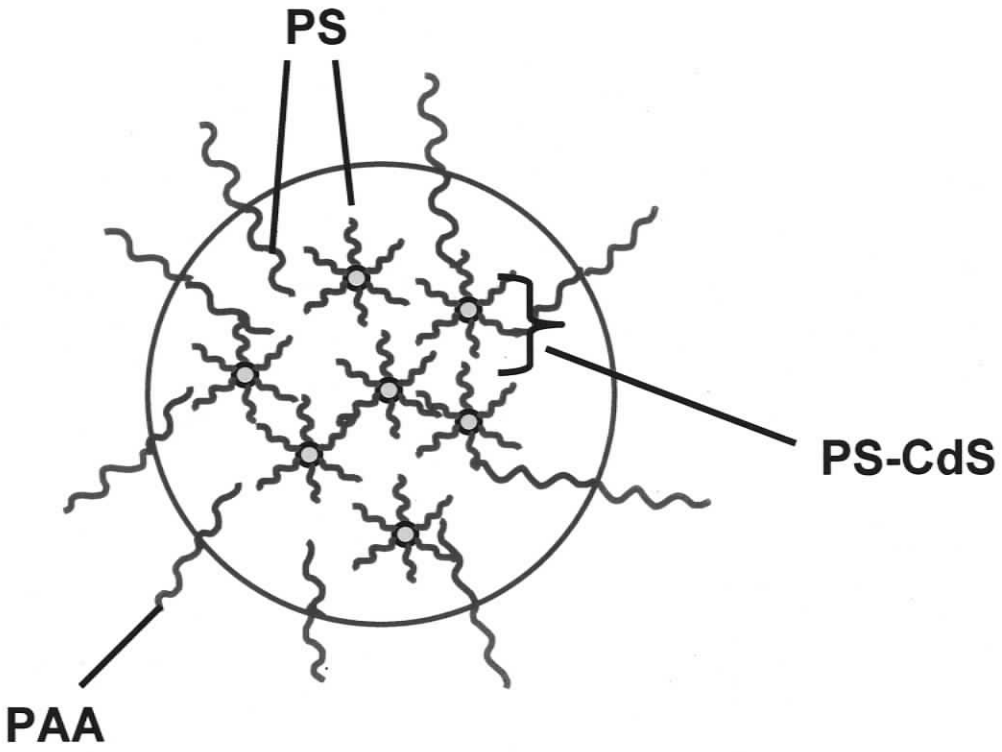

Scheme 2.3. Proposed structure of a large compound micelle (LCM).

We performed particle size distribution analysis from shadowed TEM images for the $f = 0$, 0.1, 0.3 and 0.5 blends. For each blend, several different regions of the TEM grid were randomly sampled and a minimum of 207 and maximum of 673 particles were measured and included in the analysis. The results of the distribution analysis are shown in Figure 2.11, confirming the consistent presence of a population at ~25 nm for $f = 0$, 0.1 and 0.3 due to the formation of crew-cut micelles in these blends. For the $f = 0.3$ sample, a second broad population of larger particles (LCMs) is also apparent in the distribution. Finally, the $f = 0.5$ distribution confirms the presence of a single broad distribution of

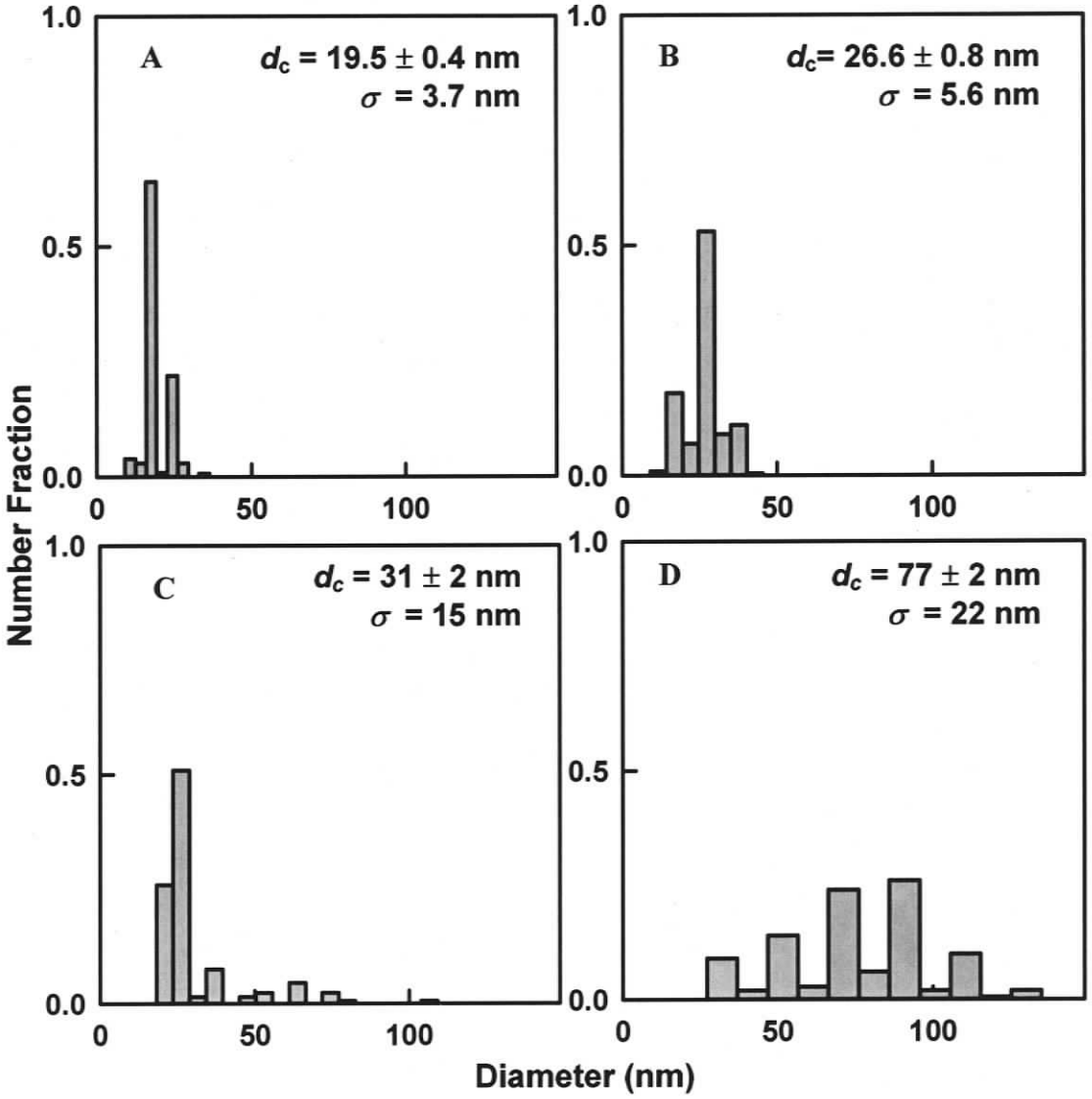

Figure 2.11. Particle size distributions determined from analysis of several TEM images for blends represented in Figure 2.10: A) $f = 0$, B) $f = 0.1$, C) $f = 0.3$, D) $f = 0.5$.

LCMs for this composition (without the crew-cut micelle peak at ~25 nm) with an average size of 77 ± 2 nm and a standard deviation of 22 nm. For the distribution analysis present in Figure 2.11, errors on the mean particle sizes were determined using the formula:

$$\text{Error} = \bar{x} \pm (1.96\sigma/\sqrt{N}) \qquad (2.15)$$

where $\bar{x}$ is the mean particle size, 1.96 is a constant for the 95 % confidence level, σ is the standard deviation and N is the number of particles counted.

It is not surprising that the distribution of LCMs obtained for the "best case" blend of the unsonciated PS-CdS1 sample (i.e. $f = 0.5$) is still quite broad ($\sigma \approx 30$ %), considering our DLS results which show that both PS-CdS1 particles and large aggregates are present in DMF before water addition without sonication. The presence of PS-CdS1 aggregates is expected to affect the resulting LCM population in the following way: as water is added to the blend of PS-CdS1 and PS-*b*-PAA stabilizing chains in DMF, the supermicellar aggregates of PS-CdS1 will start to self-assemble at a relatively low water content, since CWC decreases with increasing molar mass[15,16]. The resulting LCMs will continue to grow as more water is added, while at the same time the smaller sized individual PS-CdS1 particles start to precipitate. It is also likely that there is a distribution of aggregate sizes, resulting in a distribution of start times for LCM formation as water is added at a constant rate. This distribution of start times for LCM self-assembly results in a broad distribution of LCM sizes, since all species will become kinetically frozen at approximately the same point of water addition. In an earlier

section, it was demonstrated that PS-CdS1 aggregates in DMF could be broken up irreversibly with sonication. It was therefore of interest to investigate LCM formation under identical conditions (C_0 = 1 wt%; f = 0, 0.1, 0.3, 0.5, 0.7 and 0.9) to those described in this section, except using a PS-CdS1 stock solution that had been pre-sonicated to remove all aggregates prior to H_2O addition.

2.3.7 *Preparation of Large Compound Micelles (LCMs) in DMF/Water Mixtures: With Pre-Sonication of PS-CdS1*

The same procedure with identical blend compositions and solution concentrations as described in the earlier section was used to form the LCMs described in this section, with the exception that the PS-CdS1 was sonicated for 1000 min to break-up the supermicellar aggregates. Therefore, before water addition, the blend solutions contained only PS-*b*-PAA stabilizing chains and individual PS-CdS1 particles. With pre-sonication of PS-CdS1, CWCs determined from visual inspection of increased turbidity were as follows for the various C_0 = 1 wt% solutions: f = 0, CWC ≈ 7 wt%; f = 0.1, CWC ≈ 7 wt%; f = 0.3, CWC ≈ 3 wt%; f = 0.5, CWC ≈ 2 wt%; f = 0.7, CWC ≈ 2 wt%; f = 0.9, CWC ≈ 1 wt%. Again, the CWC was found to decrease with increasing PS-CdS1 content in the blends. Compared to CWCs without sonication of PS-CdS1 (Table 2.1), the CWCs of blends containing PS-CdS1 (f > 0) are generally higher with pre-sonication. This is explained by the break-up of aggregates lowering the average molar mass of the polymer blend solutions and therefore raising the CWC. Water was added to 25 wt% as before to ensure that the aggregates were completely frozen. We believed that once the PS-CdS1 supermicellar aggregates

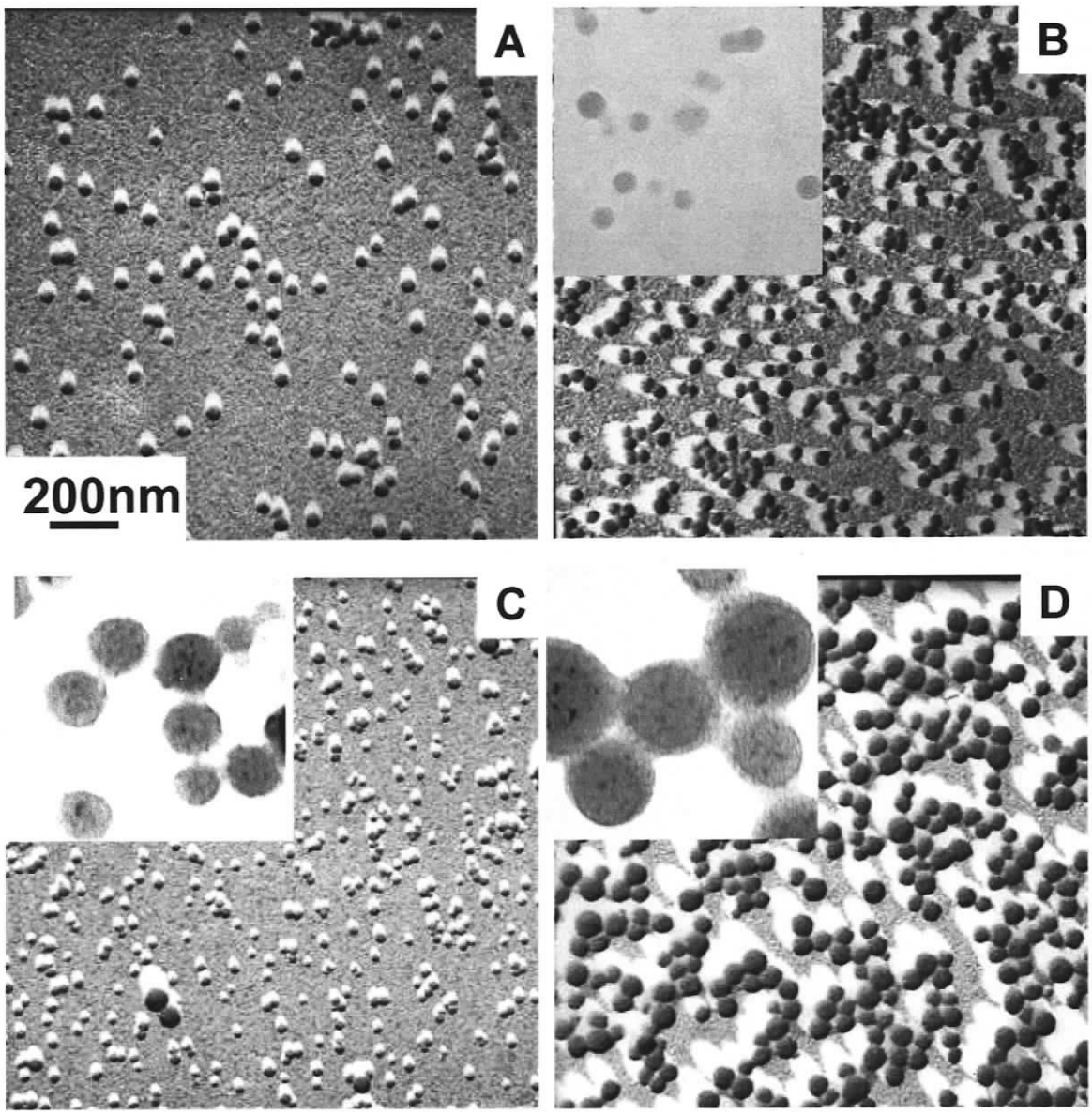

Figure 2.12. TEM images of colloids obtained from SA2 self-assembly from blends of PS(665)-*b*-PAA(68) and PS-CdS1 (with sonication). For all blends, C_0 = 1 wt%, $rate_{water}$ = 2.4 wt% / min: A) f = 0, B) f = 0.1, C) f = 0.3, D) f = 0.5. The insets show the TEM images without Pt/Pd shadowing.

were broken by sonication, the $f = 0.7$ and 0.9 blends might form stable LCM colloids; however, this was not the case. For both compositions, the yellow powder settled to the bottom of the vial. Stable colloids were achieved for $f = 0$, 0.1, 0.3 and 0.5, and these were dialyzed in pure water for 5 days and then studied by TEM.

Table 2.1: Critical Water Content (CWC) of Colloids (C_0 = 1 wt%)

Composition (f)	0	0.1	0.3	0.5	0.7	0.9
No Sonication	9 wt%	5 wt%	3 wt%	3 wt%	< 0.4 wt%	< 0.4 wt%
With Sonication	7 wt%	7 wt%	3 wt%	2 wt%	2 wt%	1 wt%

The TEM of the stable colloids (C_0 = 1 wt%; $f = 0$, 0.1, 0.3 and 0.5) deposited onto carbon/formvar substrates from aqueous media are shown in Figure 2.12A, 2.12B, 2.12C, and 2.12D, respectively. Again, before the TEM images were taken, the samples were shadowed with Pt/Pd with representative images of unshadowed samples shown in the insets. The TEM images in Figure 2.12 indicate that self-assembly of the various blends with pre-sonication of PS-CdS1 yielded particle populations that were similar to those obtained without pre-sonication (Figure 2.10). The TEM for $f = 0$ and 0.1 show a single population of crew-cut micelles, similar to samples without pre-sonication. For $f =$ 0.1 there was a very small population of larger particles that were observed in some parts of the TEM grid but again their number was insignificant; the inset to Figure 2.12B shows that the vast majority of particles possess no internal structure and are therefore crew-cut micelles. For the $f = 0.3$ sample, there are two populations again: smaller-sized

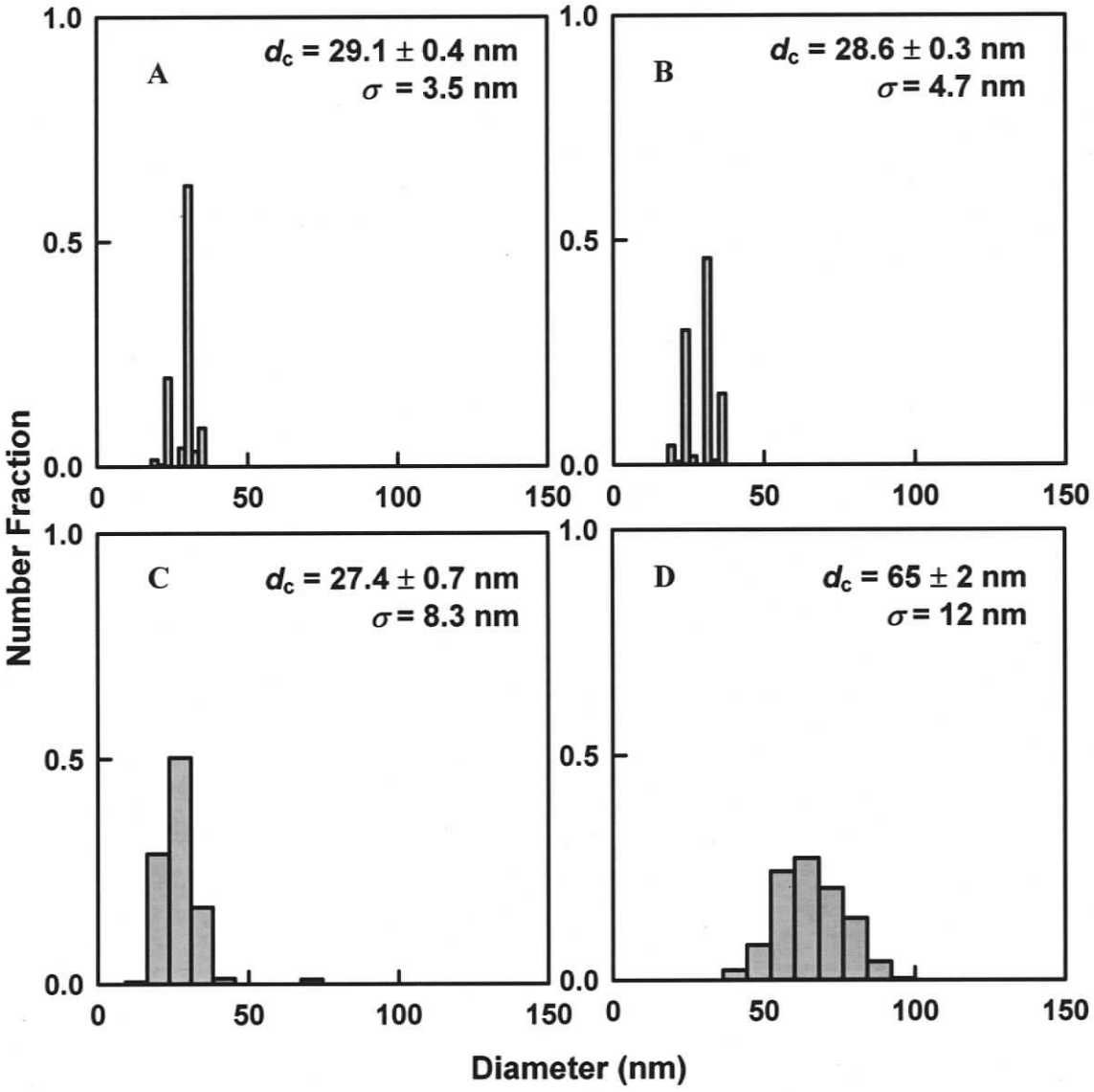

Figure 2.13. Particle size distributions determined from analysis of several TEM images for blends represented in Figure 2.12: A) $f = 0$, B) $f = 0.1$, C) $f = 0.3$, D) $f = 0.5$.

particles which are again attributed to crew-cut micelles and larger-sized particles shown from the unshadowed samples to be LCMs (the insets in Figure 2.12C show internal structures due to a distribution of electron-dense CdS nanoparticles). As shown in Figure 2.12D, when the composition of PS-CdS1 is increased to $f = 0.5$, a single population of particles was obtained, with internal structure consistent with LCMs (inset). Compared to the $f = 0.5$ blend obtained without pre-sonication, which also showed a single population of LCMs, the size distribution of LCMs in Figure 2.12D is noticeably more narrow.

Particle size distribution analysis was conducted for these samples following the same procedure described previously, with a minimum of 270 and a maximum of 723 particles counted for each sample. Results are seen in Figure 2.13. The $f = 0$, 0.1 and 0.3 blends all possess a small particle population at ~ 25 nm which is attributed to crew-cut micelles from an excess of stabilizing chains as previously discussed. We note that the crew-cut micelles from pure stabilizing chains ($f = 0$) are larger (29.1 ± 0.4 nm) compared to the previous experiment (19.5 ± 0.4 nm, Figure 2.11A). This is surprising since neither sample contains PS-CdS1 and so sonication vs no sonication will not affect the $f = 0$ cases. This difference could be due a small variation in temperature, causing differences in the thermodynamic driving force for micelle formation on the two days the samples were prepared. The trends in the number of particle populations are similar to the samples prepared without pre-sonication, with the LCM population (larger particles) starting to appear for $f = 0.3$, and a single population of larger particles (LCMs) for $f = 0.5$. Finally, for $f = 0.5$, the distribution analysis shows the LCM population to be much

less broad than without presonication of PS-CdS1 (σ = 18% compared to 30%) with a smaller mean particle size (65 ± 2 nm compared to 77 ± 2 nm). These results suggest the presence of PS-CdS1 aggregates prior to water addition results in a broadening of the population of LCMs obtained by self assembly during water addition. As discussed earlier, this can be understood in terms of a distribution of CWCs for various blend components (PS-CdS1 and PS-CdS1 aggregates) of different molar mass. We have shown that the aggregates can be broken down by sonication of PS-CdS1 in DMF, resulting in a more narrow distribution of LCMs from SA2 self-assembly.

2.4. Conclusions

Various blends of stabilizing chains of PS(665)-*b*-PAA(68) and block copolymer-stabilized PS-CdS1 nanoparticles underwent self-assembly in DMF/water mixtures. After kinetic freezing of the colloids with further water addition and subsequent removal of DMF by dialysis, the colloids showed various relative amounts of small crew-cut micelles of stabilizing chains, and LCMs consisting of aggregated PS-CdS1 with stabilizing chains at the surface. It was discovered that there is an optimum blend composition (f = 0.5) for which a single population of LCMs can be achieved without crew-cut micelles. Other blend compositions led to mixtures of crew-cut micelles and LCMs. In addition, it was apparent that the molar mass distribution of PS-CdS1 in DMF prior to water addition has a great effect on the formation of LCMs. When PS-CdS1 aggregates were present, the LCMs formed in the f = 0.5 case were relatively polydisperse (d_c = 77 ± 2 nm with σ = 29% nm). However, if the PS-CdS1 aggregates were broken via pre-sonication of PS-CdS1 in DMF, the LCMs formed were less

polydisperse and smaller in size (d_c = 65 ± 2 nm with σ = 18% nm). These results therefore provide new insights into the importance of molar mass distributions of polymer-stabilized nanoparticles on their subsequent self-assembly via water addition.

References

1. Shenhar, R.; Norsten, T. B.; Rotello, V. M. *Adv. Mater.* **2005,** 17, (6), 657-669.

2. Shenhar, R.; Rotello, V. M. *Acc. Chem. Res.* **2003,** 36, 549-561.

3. Niemz, A.; Rotello, V. M. *Acc. Chem. Res.* **1999,** 32, 44-52.

4. Boal, A. K.; Gray, M.; Ilhan, F.; Clavier, G. M.; Kapitzky, L.; Rotello, V. M. *Tetrahedron* **2002,** 58, 765-770.

5. Boal, A. K.; Ilhan, F.; DeRouchey, J. E.; Thurn-Albrecht, T.; Russell, T. P.; Rotello, V. M. *Nature* **2000,** 404, 746-748.

6. Wang, Z.; Cook, M. J.; Nygrd, A.-M.; Russell, D. A. *Langmuir* **2003,** 19, (9), 3779-3784.

7. Kumar, C. V.; Raju, B. B. *Molecular and Supramolecular Photochemistry* **2001,** 8, 505-576.

8. Deng, F.; Chen, S. *Physical Chemistry Chemical Physics* **2005,** 7, (18), 3375-3381.

9. Carrillo, A.; Swartz, J. A.; Gamba, J. M.; Kane, R. S.; Chakrapani, N.; Wei, B.; Ajayan, P. M. *Nano Lett.* **2003,** 3, (10), 1437-1440.

10. Zirbs, R.; Kienberger, F.; Hinterdorfer, P.; Binder, W. H. *Langmuir* **2005,** 21, (18), 8414-8421.

11. chneider, G.; Decher, G. *Nano Lett.* **2004,** 4, (10), 1833-1839.

12. Maury, P.; Escalante, M.; Reinhoudt, D. N.; Huskens, J. *Adv. Mater.* **2005,** 17, (22), 2718-2723.

13. Lee, W.; Chan, A.; Bevan, M. A.; Lewis, J. A.; Braun, P. V. *Langmuir* **2004,** 20, (13), 5262-5270.

14. Sommer, A. P.; Ben-Moshe, M.; Magdassi, S. *J. Phys. Chem. B* **2004,** 108, (1), 8-10.

15. Zhang, L.; Eisenberg, A. *J. Am. Chem. Soc.* **1996,** 118, 3168-3181.

16. Zhang, L.; Eisenberg, A. *Journal of Polymer Science: Part B: Polymer Physics* **1999,** 37, 1469-1484.

17. Yu, Y.; Zhang, L.; Eisenberg, A. *Macromolecules* **1998,** 31, 1144-1154.

18. Zhang, L.; Eisenberg, A. *Macromolecules* **1999,** 32, 2239-2249.

19. Zhang, L.; Barlow, R. J.; Eisenberg, A. *Macromolecules* **1995,** 28, 6055-6066.

20. Moffitt, M.; Eisenberg, A. *Macromolecules* **1997,** 30, 4363-4373.

21. Moffitt, M.; Eisenberg, A. *Chem. Mater.* **1995,** 7, 1178-1184.

22. Moffitt, M.; McMahon, L.; Pessel, V.; Eisenberg, A. *Chem. Mater.* **1995,** 7, 1185-1192.

23. Zhang, L.; Shen, H.; Eisenberg, A. *Macromolecules* **1997,** 30, 1001-1011.

24. Zhang, W.; Shi, L.; An, Y.; Gao, L.; Wu, K.; Ma, R. *Macromolecules* **2004,** 37, 2551-2555.

CHAPTER 3

Spherical Nanoparticle Assemblies in Water via Self-Assembly of Block Copolymer-Stabilized Cadmium Sulfide Nanoparticles
Part II: Kinetic Size Control of Nanoparticle Assemblies

3.1. Introduction

As mentioned in previous chapters, the unique, size-dependent properties of metallic and semiconducting nanoparticles (quantum dots) make them ideal candidates for structural elements in photonic devices, inspiring a growing amount of research into the control of nanoparticle ordering on multiple length scales. Such spatial control will be essential for real device applications since the overall properties of a photonic device are dependent on a combination of effects operating on different length scales.

The work described in this thesis employs a new "multi-step" self-assembly approach to form photonic structures, based on hybrid building blocks of CdS nanoparticles encapsulated in the cores of stable block ionomer micelles. Briefly, each self-assembly step can be described as follows: 1) SA1: self-assembly of PS-*b*-PAA to form block ionomer reverse micelles, followed by synthesis of a single CdS semiconducting nanoparticle in each core, forming the hybrid building blocks PS-CdS; 2) SA2: self-assembly of blends of PS-CdS and PS-*b*-PAA stabilizing chains (a different copolymer composition than was used to assemble PS-CdS) in DMF/water mixtures by addition of water to form large compound micelles (LCMs); 3) SA3: self-assembly of LCMs into ordered close-packed arrays by slow water evaporation.

Chapter 2 and Chapter 3 of this thesis both focus on our investigations to develop control over LCM size and polydispersity in the SA2 step. Both of these issues are critical for the subsequent SA3 self-assembly: the size of LCMs formed in the SA2 step will determine the periodicity of the close-packed array of LCMs resulting from the SA3 step, and periodicities on the order of the wavelength of visible light will be desirable for photonic applications. Low polydispersity of LCMs is also essential since polydisperse

spheres will not form close-packed arrays with long-range order. In the previous chapter, we demonstrated that the polydispersity of LCMs is affected by the polydispersity of the PS-CdS sample before water addition, with a broader distribution of LCMs obtained from PS-CdS1 in a partially aggregated state than was obtained from PS-CdS1 without aggregates (following sonication). We also showed that for blends of PS-CdS1 and PS(665)-*b*-PS(68), only one of the investigated blend compositions, containing 50 wt% of both components ($f = 0.5$), resulted in a single population of stable LCMs without the presence of crew-cut micelles formed from the self-assembly of excess stabilizing chains. In this chapter, we again focus on SA2 self-assembly by looking at strategies for LCM size control. This work begins with the recognition that any size control of LCMs must be kinetic in origin, since LCM formation is a macrophase separation process governed entirely by interfacial energy, such that there is no thermodynamic minimum particle size. However, we demonstrate here the first examples of LCM size control using two kinetics-based strategies, one involving variation in the total initial polymer concentration, C_0, and the other involving variation in the rate of water addition, $rate_{water}$.

To underline the relative roles of thermodynamics and kinetics which are the basis of size control in the present chapter, it is worth reviewing the important aspects of LCM formation (SA2 self-assembly) described in the previous chapters. LCM formation is initiated by the slow addition of water to blends of two components in DMF: "free" PS-*b*-PAA chains and PS-CdS particles consisting of a PS-*b*-PAA-stabilized CdS core. Above a critical water content (CWC), the higher-molar mass PS-CdS component of the blend will phase separate, forming a polymer-rich phase via spinodal decomposition which will eventually break into spherical clusters of PS-CdS particles (LCMs), which will then

continue to grow in order to decrease interfacial energy[1]. Without the presence of stabilizing chains, this process would occur quickly, ultimately leading to precipitation of the PS-CdS particles. However, above the CWC, the PS-*b*-PAA chains will distribute themselves at the interface of the polymer-rich phase and the solvent mixture, lowering the interfacial free energy and stabilizing the LCMs against agglomeration due to repulsive interactions between charged PAA chains at the LCM surface. Thus the stabilizing chains slow the process of phase separation and LCM growth to a time scale in which continued water addition can be used to "freeze in" colloidally stable LCM particles. This "freezing in" is a result of the fact that continued water addition above the CWC not only increases the driving force for self-assembly, but also simultaneously "applies the brakes" to the process, since increased water content progressively forces DMF from the polymer-rich phase, thus lowering the mobility of chains within the LCMs and hindering their further growth. It was been previously shown that for analogous systems PS-*b*-PAA and blends of PS-*b*-PAA and PS homopolymer in DMF/water mixtures, aggregates become "frozen" on the experimental time scale at the water content between 8 and 11 wt%[2]. Therefore, we typically continued to add water above the CWC to a total water content of 25 wt%, at which point the aggregates are kinetically frozen. According to this procedure, LCM formation and growth can be regarded as occurring in a window of time between the CWC and the point of water addition where no further growth can occur on a reasonable time scale.

The two strategies for LCM size control demonstrated here are based on tuning the width of the kinetic window in which LCM growth can occur. In the first case, we vary the initial polymer concentration in DMF; higher polymer concentrations are known

to result in lower CWCs[2-7], which should result in an earlier onset of LCM formation and a wider window for LCM growth given a constant rate of water addition. In the second case, we vary the rate of water addition for a constant polymer concentration. As in the previous chapter, we also investigated the effect of blend composition of LCM formation, since a different PS-CdS sample is employed here than in the previous chapter. Finally, after demonstrating some size control, we investigate the hydrodynamic sizes of various LCM samples in pure water using dynamic light scattering (DLS), in order to determine the degree of PAA chain stretching on the LCM surface.

In this chapter, the hybrid building blocks used to prepare LCMs are designated PS-CdS2, which were formed by the same method described for PS-CdS1 in the previous chapter, but using a different constituent copolymer PS(300)-*b*-PAA(12), which we synthesized using anionic polymerization and subsequent hydrolysis. For the stabilizing chains, we used the same copolymer PS(665)-*b*-PAA(68) that was employed in the previous chapter.

3.2. Experimental

3.2.1. Synthesis of Polystyrene-b-Poly(acrylic acid) (PS-b-PAA) Diblock Copolymer

Anionic polymerization of PS-*b*-PtBA and subsequent hydrolysis to PS-*b*-PAA was used to synthesize both of the polystyrene-*b*-poly(acrylic acid) (PS-*b*-PAA) diblock copolymers used for this chapter; PS(665)-*b*-PAA(68) (stabilizing chains) was described previously in Chapter 2. The second diblock copolymer, PS(300)-*b*-PAA(12), used to prepare the PS-CdS2 sample, was synthesized using the same methodology. A similar fractionation procedure used to remove PS homopolymer impurity from PS(665)-*b*-PAA(68) (described in Chapter 2) was also used to purify PS(300)-*b*-PAA(12), resulting in a PS homopolymer content of ~8 wt% in this sample after fractionation compared to ~14 wt% prior to fractionation.

3.2.2. Preparation of Block Copolymer-Stabilized CdS Nanoparticles (PS-CdS2)

After fractionating the diblock copolymer PS(300)-*b*-PAA(12), it was converted to PS-CdS2 hybrid nanoparticles using the same procedure as described in Chapter 2. The resulting block copolymer-stabilized CdS nanoparticles, consisting of a CdS core, a poly(cadmium acrylate) surface layer and a polystyrene corona (see Figure 1.8 in Chapter 1), is designated PS-CdS2. Compared to PS-CdS1 prepared in the previous chapter, the PS coronal chains surrounding PS-CdS2 are twice as long (300 compared 145 repeat units), which should minimize the anomalous presence of PS-CdS aggregates in DMF described in Chapter 2. The characterization of PS-CdS2 nanoparticles will be described in the Results and Discussion section.

3.2.3. Preparation of Large Compound Micelles in DMF

The large compound micelles (LCMs) in this chapter were prepared using the same general procedure as described in the previous chapter: PS(665)-*b*-PAA(68) and PS-CdS2 were each dissolved in separate DMF solutions with the same initial polymer concentration, C_0, and stirred overnight at room temperature. These solutions were then mixed in various ratios to obtain different blend solutions with initial polymer concentration, C_0, and different compositions designated by the weight fraction of PS-CdS2 (f) relative to the total polymer content. Water was then added dropwise with rapid stirring to ~5 g of each blend solution at a constant rate, $rate_{water}$, to a total water content of 25 wt%, noting the point at which an increase in turbidity indicated the CWC. The samples were finally dialyzed against de-ionized water to remove all DMF for characterization by TEM and DLS. Specific parameters for various series of experiments using this general methodology are described in the sections below. Each series of experiments involved several LCM preparations with a single experimental parameter varied. All experiments in a series were carried out consecutively on the same day. The lab temperature was monitored over the course of all the experiments was found to be 22.5 ± 1°C.

3.2.3.1. Effect of Composition, f

In this series of experiments, the initial total polymer concentration was kept constant at C_0 = 0.5 wt% for the following compositions of blends (f = weight fraction PS-CdS2): f = 0, 0.1, 0.3 or 0.5. For each blend, the rate of water addition was constant at 20 μL every 20 seconds ($rate_{water}$ = 1.2 wt% / min for 5 g solution).

3.2.3.2. Effect of Concentration, C_0

In two series of experiments, the blend composition, f, was kept constant at either $f = 0$ (pure stabilizing chains) or 0.5, with various initial total polymer concentrations for each composition: $C_0 = 0.5$, 1, 2, 3, 4 wt%. For each blend, the rate of water addition was constant at 20 μL every 20 seconds ($rate_{water}$ = 1.2 wt% / min for 5 g solution).

3.2.3.3. Effect of the Speed of Water Addition, $rate_{water}$

In this series of experiments, the initial total polymer and the blend composition were constant for all preparations: $C_0 = 0.5$ wt% and $f = 0.5$. However, the speed of water addition was varied by adding a 20 μL drop every 5, 10, 20, 40 or 60 seconds for different preparations. This translated into $rate_{water}$ = 4.8, 2.4, 1.2, 0.6, or 0.4 wt% / min for an initial mass of 5 g solution.

3.2.4. Static Light Scattering

SLS of PS-CdS2 in DMF was carried out to characterize the block copolymer-stabilized CdS nanoparticles before secondary self-assembly to form LCMs. The SLS experiments were carried out on a Brookhaven Instruments multi-angle system equipped with a BI-200SM goniometer, a BI-9000AT digital autocorrelator, and a Melles Griot He-Ne Laser (632.8 nm) with maximum power output of 75 mW. To ensure the accuracy of SLS measurement, great care was taken to eliminate dust from the samples. Spectroscopic grade DMF was filtered through two membrane filters with 0.20 μm nominal pore size connected in series, and stock solutions of PS-CdS2 colloid dispersed

in DMF was filtered through two membrane filters with 0.45 μm nominal pore size connected in series. All scintillation vials were thoroughly cleaned with filtered DMF, and stock solutions of the PS-CdS2 were filtered into the dust-free scintillation vials. Successive dilutions of the colloids were carried out by adding known quantities of filtered DMF.

The stock solutions of PS-CdS2 with concentrations of ca. 10 mg/mL were prepared the night before SLS measurements to ensure equilibration. SLS measurements were carried out in a concentration range from 1 - 0.1 mg/mL and the angles of detection ranged from 15-155° with 5 degree increments between measurements. Ten repeat measurements of scattered light intensity were taken at each angle and concentration. The reported aggregation number and radius of gyration were determined for the average results of two separate Zimm plots obtained from different stock solutions. All SLS measurements were conducted at 23°C.

3.2.5. Dynamic Light Scattering

All DLS experiments were carried out on a Brookhaven Instruments photon correlation spectrometer equipped with a BI-200SM goniometer, a BI-900AT digital autocorrelator, and a Melles Griot He-Ne Laser (632.8 nm) with maximum power output of 75 mW. To ensure the accuracy of DLS measurements, great care was taken to eliminate dust from the samples.

For the measurements of PS-CdS2, spectroscopic grade DMF was filtered through 2 membrane filters connected in series with 0.20 μm nominal pore size; stock solutions of PS-CdS2 colloids dispersed in DMF with concentration of ca. 5 mg/mL were filtered

through 2 membrane filters connected in series with 0.45 μm nominal pore size. All scintillation vials were thoroughly cleaned with filtered DMF, and the stock solution of the PS-CdS2 colloids was filtered into the dust-free scintillation vials. Successive dilutions of the colloids were carried out by adding known quantities of filtered DMF. DLS measurements were conducted at these angles to determine the true hydrodynamic diameter: 35°, 50°, 70°, 90°, and 120° and at five different concentrations in the range of 1.0 - 0.1 mg/mL. For each experiment, 3 repeat measurements of the autocorrelation function were obtained. All DLS measurements were conducted at 23°C. The equations described in the Experimental section in Chapter 2 will be utilized in this chapter as well.

For the DLS measurements of LCMs with initial polymer concentration C_0 = 0.5 wt%, 1 wt%, 2 wt%, 3 wt% and composition of f = 0.5: deionized water was filtered through 2 membrane filters connected in series with 0.20 μm nominal pore size; the stock solutions of the LCMs dispersed in aqueous solutions were not filtered. All scintillation vials were thoroughly cleaned with filtered deionized water, and the stock solutions of LCMs were added to the dust-free scintillation vials. DLS measurements were conducted at one angle: 90° and for each LCM solution a certain concentration was chosen that yielded a scattering of ~ 500 kilo counts per second for a constant pinhole (100 μm), the concentration ranged from 0.1 – 0.01 mg/mL. To ensure that each concentration gave a true, concentration independent particle size, the C_0 = 0.5 wt%, f = 0.5, was diluted to the lowest concentration used (0.01 mg/mL) and the particle size remained constant. For each experiment, 3 repeat measurements of the autocorrelation function were obtained. All DLS measurements were conducted at 23°C.

3.2.6. UV-Vis Absorption and Photoluminescence Measurements

Absorption spectra of PS-CdS2 were recorded on a Cary 50-scan UV-Vis spectrophotometer using samples dissolved in spectroscopic grade toluene with pure spectroscopic grade toluene subtracted as the background. Static fluorescence measurements were recorded on an Edinburgh Instruments FLS 920 instruments equipped with a Xe 450 W arc lamp and a red sensitive PMT (R928-P). For typical measurements of fluorescence, the PS-CdS2 samples were dispersed in spectroscopic grade toluene at concentrations such that the measured absorbance at 400 nm was less than 0.1; this is to keep the concentration low enough so that the auto-absorption effects were minimized. To obtain the final fluorescence spectrum of PS-CdS2, the spectrum of the solvent (spectroscopic grade toluene) was subtracted. The fluorescence spectra was recorded at 1 nm spectra resolution, λ_{ex} = 350, 375, 400, 425 nm using a 425 nm filter for the first three excitations and a 515 nm for the last excitation.

3.2.7. Transmission Electron Microscopy

Transmission electron microscopy (TEM) of various aqueous LCM colloids was performed on a Hitachi H-700 electron microscope, operating at an accelerating voltage of 75 kV. LCMs in water were diluted to a concentration of 0.5 mg/mL and then a 10 μL drop was deposited on a carbon coated formvar 300 mesh copper grid and then shadowed with Pt/Pd wire for imaging. Also, images were taken of the same solutions without Pt/Pd shadowing, in order to characterize the LCM internal structure.

3.3. Results and Discussion

3.3.1. Characterization of Block Copolymer-Stabilized CdS Nanoparticles (PS-CdS2): SEC, UV-Vis, and Photoluminescence.

The diblock copolymer PS(300)-*b*-PAA(12) was used to prepare the block copolymer-stabilized CdS nanoparticles, PS-CdS2, using the procedure described in Chapter 2. Figure 3.1 shows SEC chromatograms of the PS-CdS2 sample in THF: one from the refractive index detector, RI, and the other from the low-angle light scattering detector, LALS. They both show broad peaks attributed to the block copolymer-stabilized quantum dots. The RI also shows a low molecular-weight shoulder, which may be due to unmicellized copolymer or PS homopolymer impurity not removed in the fractionation step. The RI and LALS signals were integrated and the results used to estimate the number-average molar mass of PS-CdS2 (again assuming that *dn/dc* was equivalent to PS in THF = 0.185). This gave M_n = 1.040 10^6 g/mol for PS-CdS2, from which an aggregation number of ~30 PS(300)-*b*-PAA(12) chains surrounding each CdS nanoparticle was calculated. This result will be compared to the molar mass and aggregation number of PS-CdS2 in DMF from multi-angle SLS in a later section.

The optical properties of PS-CdS2 were also characterized using UV-Vis absorption and photoluminescence spectroscopy as shown in Figure 3.2. The UV-Vis absorption spectrum shows an exciton ~ 430 nm with an absorption threshold of λ_{thresh} = 465 nm, from which the size of the CdS core was calculated to be 4.0 nm using the following formula: $d_{CdS} = 1 / (0.1338 - 0.0002345\lambda_{thresh})$[8, 9]. For photoluminescence the solutions were prepared in spectroscopic grade toluene

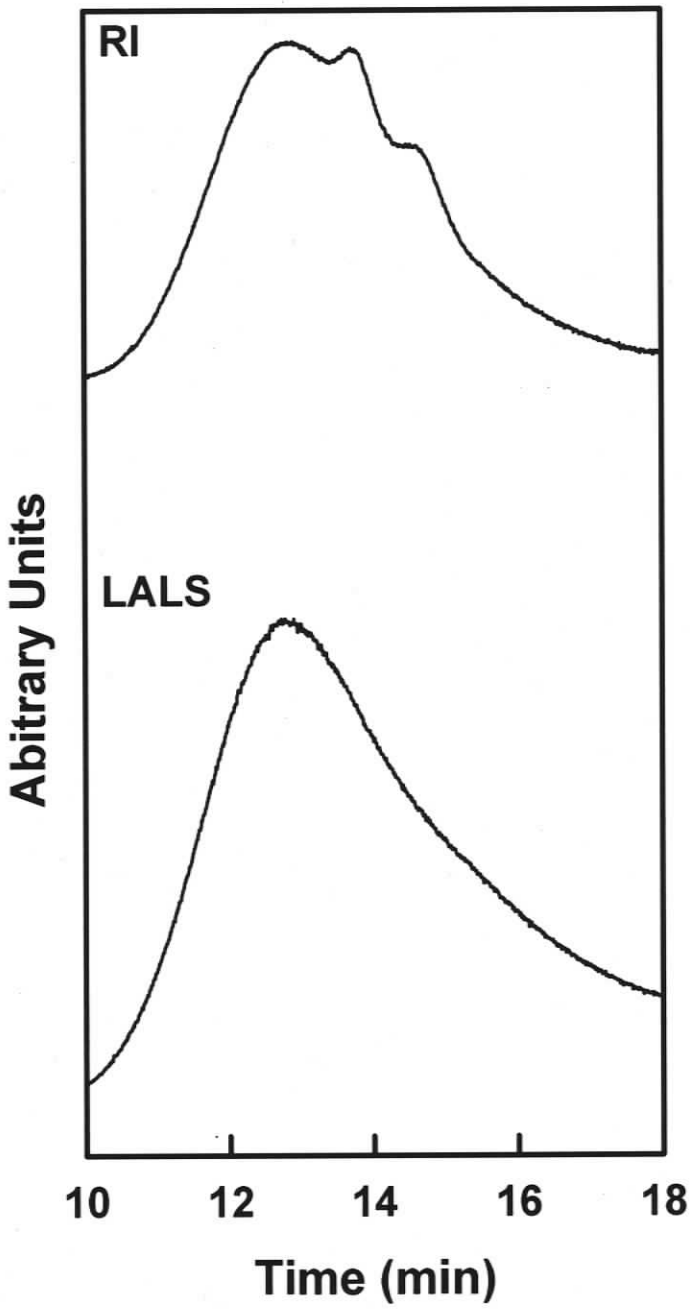

Figure 3.1. SEC of block copolymer-stabilized CdS nanoparticles, PS-CdS2 dissolved in THF. The top chromatogram shows the refractive index (RI) detector signal and the bottom chromatogram shows the low-angle light scattering (LALS) detector signal.

with optical densities < 0.1 at 400 nm to avoid auto-absorption effects. For excitation at λ_{ex} = 350, 375, 400, and 425 nm, Figure 3.2 shows a broad red-shifted emission band, which is attributed to recombination from a distribution of deep trap states localized at the quantum dot surface. A very weak band-edge emission is also visible which is attributed to recombination from band-edge or near band-edge states. The low intensity of band-edge emission compared to trap state emission suggests a high density of surface trap states in PS-CdS2 and a correspondingly high probability of crossover to these trap states once an exciton is created by light absorption.

3.3.2. Dynamic and Static Light Scattering of PS-CdS2

We characterized PS-CdS2 in DMF by dynamic light scattering (DLS) to determine the hydrodynamic diameter and to ascertain whether supermicellar aggregates were present as were found in PS-CdS1. Solutions of various concentrations of PS-CdS2 in DMF were prepared by successive dilutions by adding various known quantities of filtered DMF to a filtered stock solution. The measurements were conducted at five different angles: 35°, 50°, 70°, 90°, and 120°, and at five different concentrations in the range of 0.10 – 1.0 mg/mL.

As described in Chapter 2, the cumulant method was used to analyze the normalized electric field autocorrelation function (Equation 2.8), in order to determine a mean relaxation rate, $\bar{\Gamma}$, for each scattering angle. Figure 3.3A shows plots of $\bar{\Gamma}$ vs. the

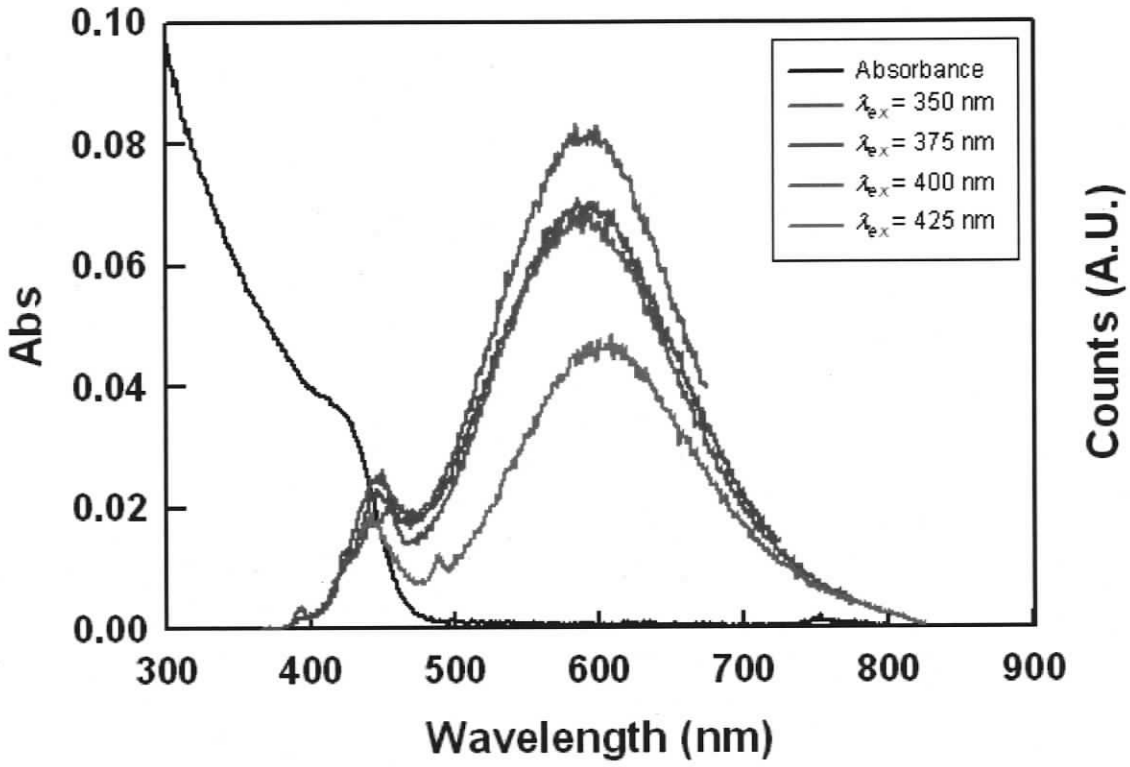

Figure 3.2. Absorbance and photoluminescence (PL) spectra of PS-CdS2 dissolved in spectroscopic grade toluene (λ_{ex} = 350, 375, 400, and 425 nm). The core size of the CdS was determined to be d_{CdS} = 4.0 nm from λ_{thresh} = 465 nm. The PL spectrum was recorded at 1 nm spectral resolution using a 425 nm filter for the first three excitations and 515 nm for the last excitation and was solvent-subtracted.

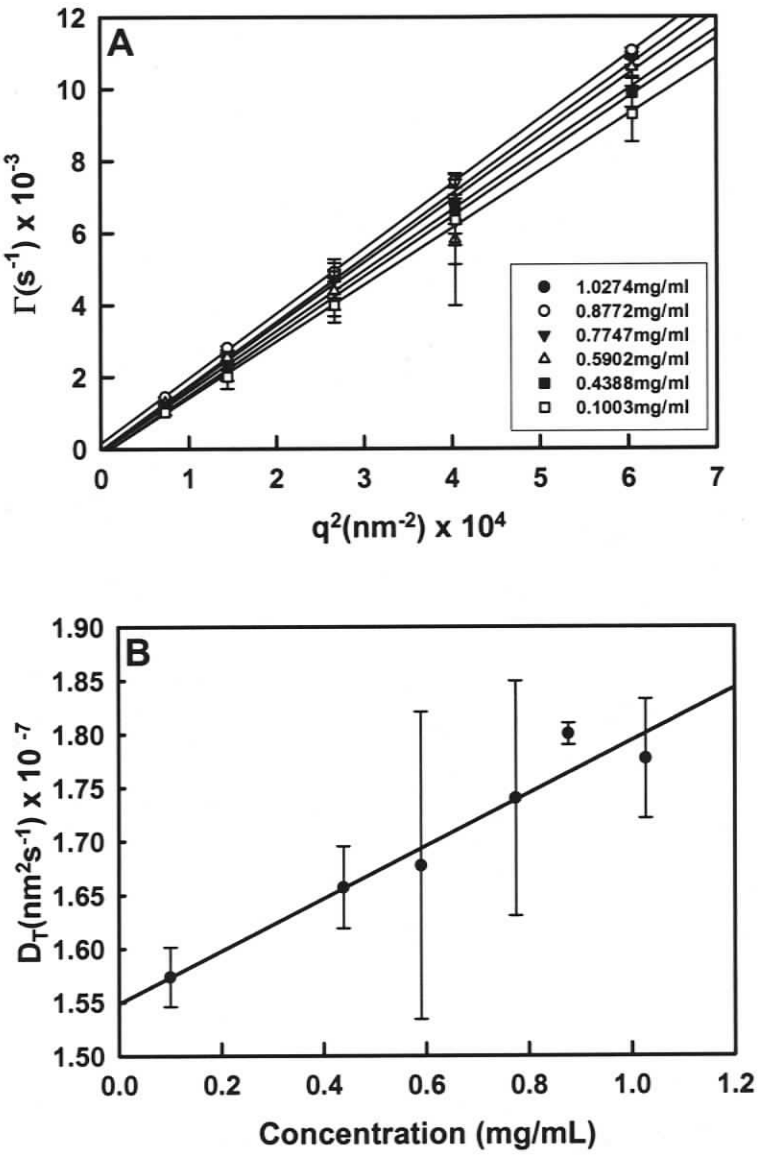

Figure 3.3. Dynamic light scattering (DLS) data for PS-CdS2 sample dissolved in DMF: A) $\bar{\Gamma}$ vs q^2 for various concentrations of PS-CdS2 in DMF, B) plot of the effective diffusion coefficient D_T vs concentration.

square of the scattering vector q^2 for various concentrations. Each of these plots is linear, which means that there was a diffusive relaxation mode from the free translational diffusion of particles. From the slope of each line, the effective diffusion coefficient D_T was determined for each concentration (Eq. 2.10). Figure 3.3B shows D_T plotted against concentration and the resulting extrapolation to infinite dilution (c = 0) with diffusion coefficient at infinite dilution D_0 = 1.55 ± 0.02 x 10^{-7} nm^2 s^{-1} determined from the intercept. We can see that there is a linear relationship between D_T and c with a positive slope giving k_d = 1.6 ± 0.2 x 10^{-4} cm^3 g^{-1} ($D_T = D_0 (1 + k_d c)$). A positive k_d value indicates that there are repulsive interactions between PS-CdS2 particles in DMF. From the diffusion coefficient D_0, the hydrodynamic diameter at infinite dilution, d_0, was calculated using the Stokes-Einstein relation (Eq. 2.13) and a value of 36 nm was obtained compared to 32.5 nm given by the software. This value is consistent with individual PS-CdS2 particles, compared to literature values for reverse micelles in organic solvent with comparable PS coronal chain lengths[10]. This suggests that unlike PS-CdS1, no aggregates of PS-CdS2 are present in DMF. The CONTIN of PS-CdS2 did not consistently show two populations of particle size (1% showed two populations). Therefore, this led us to conclude that there are no aggregates present.

Static light scattering of PS-CdS2 in DMF was also performed for scattering angles from θ = 25° to 145° or from θ = 45° to 145° for two repeat runs, using concentrations from c = 1.18 mg/mL to c = 0.158 mg/mL or c = 1.02 mg/mL to c = 0.100 mg/mL, respectively. For both runs, the resulting data were compiled into a Zimm plot,

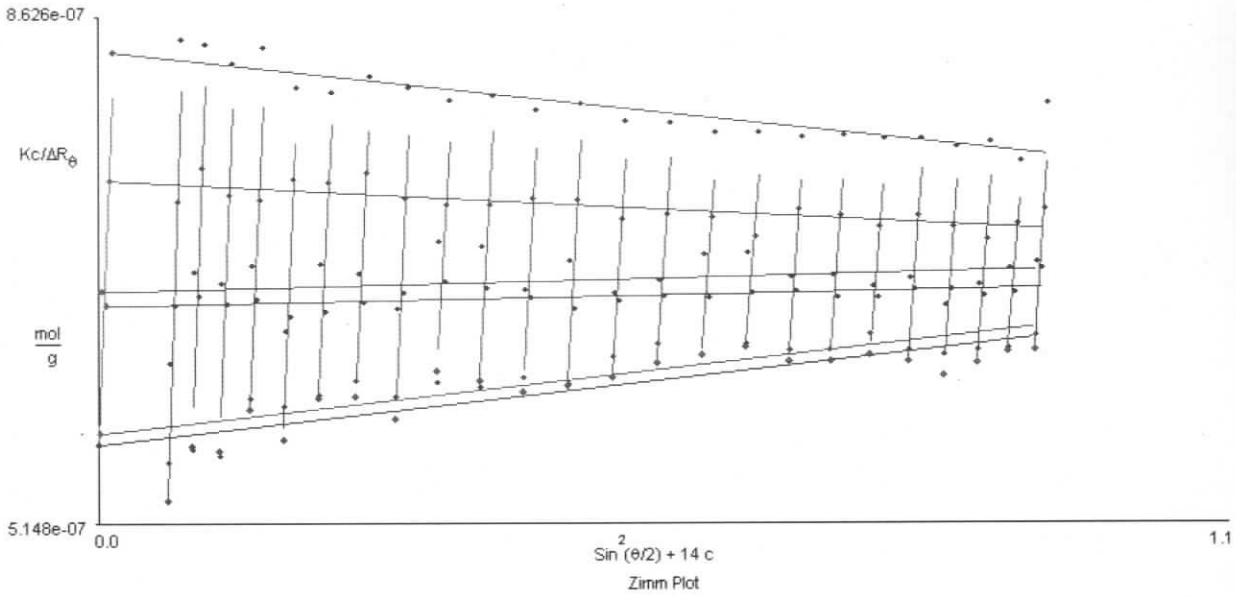

Figure 3.4. Static light scattering (SLS) of PS-CdS2 in DMF. The angles used in these measurements were from 5° to 155° in 5° increments, with concentrations between 0.1 to 1.0 mg/mL.

one of which is shown in Figure 3.4; this plot is based on the Zimm equation given in Chapter 2 (Eq. 2.7). From the intercept and slope of data extrapolated to infinite dilution and zero scattering angle, Zimm plots were used to determine a weight-average molar mass, M_w and a radius of gyration, r_g. Based on the average of both runs, we determined $M_w = 1.78 \pm 0.06 \times 10^6$ g/mol, from which an aggregation number of *54 ± 2* PS-*b*-PAA chains surrounding each CdS nanoparticle was determined. Also from Zimm plots, the radius of gyration, r_g, of PS-CdS2 in DMF was determined to be 21 ± 8 nm. The ratio of r_g/r_h from a combination of SLS and DLS results is known to provide structural information on particles in solution, with $r_g/r_h = 0.775$ indicating hard spheres and $r_g/r_h \sim 1.1$ being found for spherical star-like particles[11]. Using the hydrodynamic radius r_h (18 ± 1 nm) determined from DLS, and the radius of gyration r_g (21 ± 8 nm) determined from SLS we obtain a ratio of $r_g/r_h \sim 1.2 \pm 0.4$, which is consistent with non-aggregated spherical star-like particles.

3.3.3. Control of Large Compound Micelle (LCM) Formation: Effect of PS-CdS2 / PS(665)-b-PAA(68) Blend Composition, f.

To determine the effect of the relative amount of stabilizing chains on LCM formation for this system, we prepared a series of blend solutions in DMF with constant total initial polymer concentration $C_0 = 0.5$ wt% and various weight fractions of PS-CdS2 in the blends: $f = 0$, 0.1, 0.3, and 0.5 ($f = 0.7$ and 0.9 were not prepared for this study because the colloids formed from these compositions for the blend system described in Chapter 2 were unstable and underwent macroscopic precipitation). To these four solutions, water was added drop-wise at a rate of 20 μL every 20 seconds ($rate_{water} = 1.2$

wt% / min). For each clear yellow blend solution, the onset of turbidity with water addition indicated the critical water content (CWC) and the start of SA2 self-assembly. The CWCs of the four C_0 = 0.5 wt% solutions, determined from the number of added water drops at which turbidity was first observed, were as follows: f = 0, CWC = 3.8 wt%; f = 0.1, CWC = 3.1 wt%; f = 0.3, CWC = 3.1 wt%; f = 0.5, CWC = 2.3 wt%. For a constant total polymer concentration, the CWCs were found to decrease as the PS-CdS2 content increased. This is not surprising because, as previously discussed, the CWC decreases with both concentration and molar mass of the precipitating polymer, and an increase in f represents an increase in the concentration of the higher molar mass PS-CdS2 component. After the CWC was reached for each solution, water was added at the same rate to a total water content of 25 wt% then the aggregates were dialyzed for five days against pure water to remove all remaining DMF. All four blend compositions resulted in stable aqueous colloids which were characterized by TEM.

TEM of the self-assembled blend solutions C_0 = 0.5 wt%, f = 0, 0.1, 0.3, and 0.5, deposited from aqueous colloids onto carbon/formvar substrates on copper TEM grids are shown in Figure 3.5A, B, C and D, respectively. After being deposited onto TEM grids, the samples were shadowed with Pt/Pd using high temperature vacuum sputtering. This shadowing assists in increasing the contrast between the particles and the substrate and results in the teardrop-shaped shadow oriented along the direction of sputtering in each of

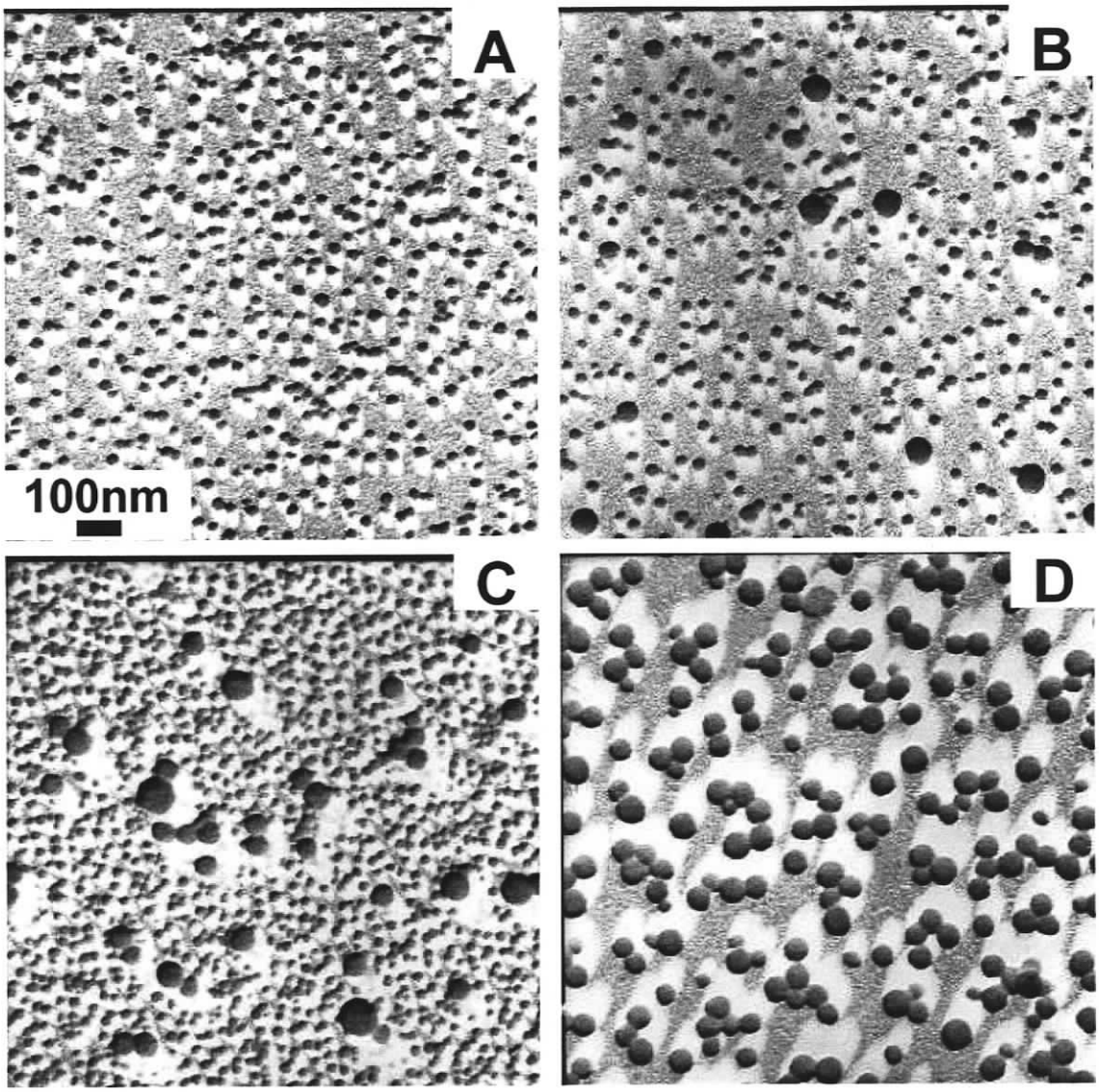

Figure 3.5. TEM images of colloids obtained from SA2 self-assembly of blends of PS-CdS2 and PS(665)-*b*-PAA(68). For all blends, C_0 = 0.5 wt%, $rate_{water}$ = 1.2 wt% / min: A) f = 0, B) f = 0.1, C) f = 0.3, D) f = 0.5.

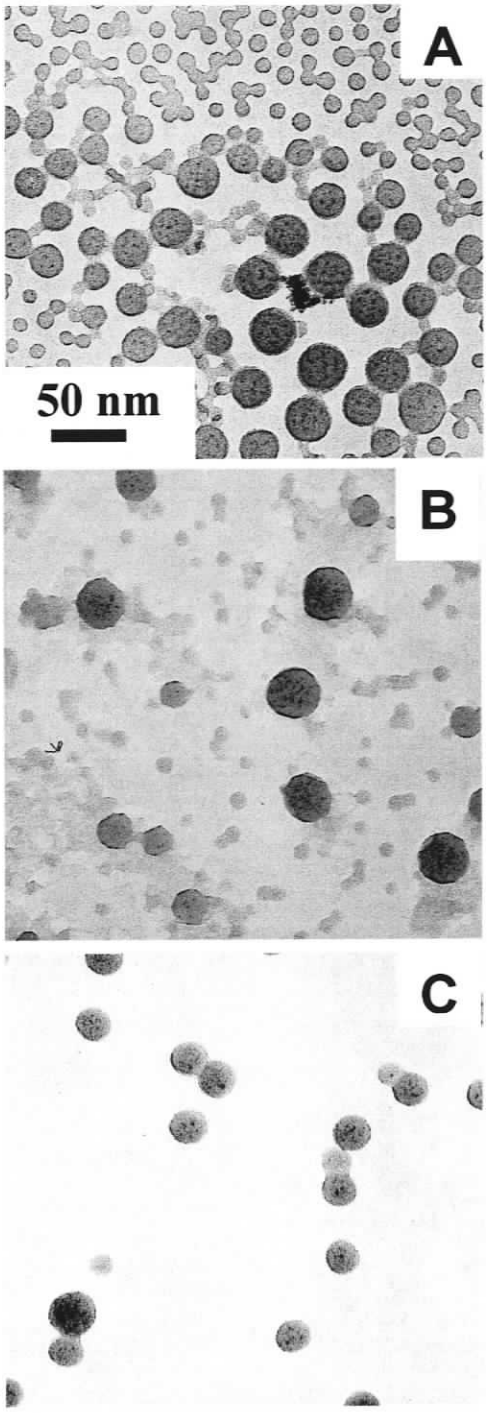

Figure 3.6. TEM images (without Pt/Pd shadowing) of colloids obtained from SA2 self-assembly of blends of PS-CdS2 and PS(665)-*b*-PAA(68). For all blends, C_0 = 0.5 wt%, $rate_{water}$ = 1.2 wt% / min: A) f = 0.1, B) f = 0.3, C) f = 0.5. The larger particles are LCMs and the dark spots inside the LCMs are CdS nanoparticles.

the images. TEM images for the $f = 0$ sample (Figure 3.5A), which contained only PS(665)-*b*-PAA(68) chains and no PS-CdS2, shows a single population of small particles which must be crew-cut micelles formed from self-assembly of the block copolymer. For the $f = 0.1$ sample (Figure 3.5B), a similar population of small particles to that found for $f = 0$ is observed; in addition, a small number of larger particles can also be seen. For the $f = 0.3$ (Figure 3.5C), the same two particle populations are present, though the relative number of larger particles appears to have increased. Finally, for the $f = 0.5$ sample (Figure 3.5D), a single population of the larger particles is obtained, and none of the smaller particles are observed. TEM of the various samples without Pt/Pd shadowing (Figure 3.6) allowed the internal structures of the various aggregates to be imaged, so that the nature of the different particle populations could be assessed. For the $f = 0.1$ and 0.3 samples (Figure 3.6A and B), the smaller particles appear as homogenous circles without internal structure, while the larger particles clearly show internal structures with a distribution of electron-dense spots throughout the spherical polymer matrix. Unshadowed images of the single population of larger particles obtained for $f = 0.5$ (Figure 3.6C) indicates that they possess similar internal structure to the larger particles at $f = 0.1$ and $f = 0.3$. The structure of these larger particles shows that they are LCMs, arising from self-assembly of PS-CdS2 with PS(665)-*b*-PAA(68) stabilizing chains distributed at the particle surface, similar to LCMs described in the previous chapter from self assembly of PS-CdS1 with PS(665)-*b*-PAA(68) stabilizing chains (Scheme 2.3). The lack of internal structure for the smaller particle populations in the $f = 0.1$ and $f = 0.3$ samples, and their similar size to the particles observed when no PS-CdS2 is present ($f = 0$), indicates that they are crew-cut micelles arising from the self-assembly of PS(665)-*b*-

PAA(68) stabilizing chains alone. Therefore, similar to the results described in the previous chapter for PS-CdS1 and PS(665)-*b*-PAA(68) stabilizing chains, we find that there is an excess of stabilizing chains in the $f = 0.1$ and $f = 0.3$ blends as the LCMs are formed; this results in the formation of a separate crew-cut micelle population from residual PS(665)-*b*-PAA(68) chains with continued water addition above the CWC. However, we find that a single population of LCMs, without crew-cut micelle formation, could be obtained when the relative amount of stabilizing chains was decreased ($f = 0.5$) (Figure 3.5D). This indicates that a critical ratio of PS-CdS2 to stabilizing chains ($f \approx 0.5$) is required to obtain a stable LCM population without an excess of stabilizing chains, just as was found for blends containing PS-CdS1.

Particle size distribution analysis was carried out from the shadowed TEM images of the $f = 0$, 0.1, 0.3, and 0.5 blends. For each blend, various regions of the TEM grid were randomly sampled and a minimum of 325 and a maximum 541 particles were measured and included in the analysis. The results of the distribution analysis are shown in Figure 3.7, confirming the consistent presence of a population at ~25 nm for $f = 0$, and 0.3 which is attributed to the crew-cut micelles (Figure 3.7A and B). For the $f = 0.1$ and 0.3 samples, the appearance of a much less numerous population of larger particles, which we have shown to be LCMs, are also apparent in the distribution. Finally, the $f = 0.5$ sample distribution confirms the presence of a single population of larger particles (LCMs), without the presence of a crew-cut micelles peak at ~25 nm. For $f = 0.5$, the

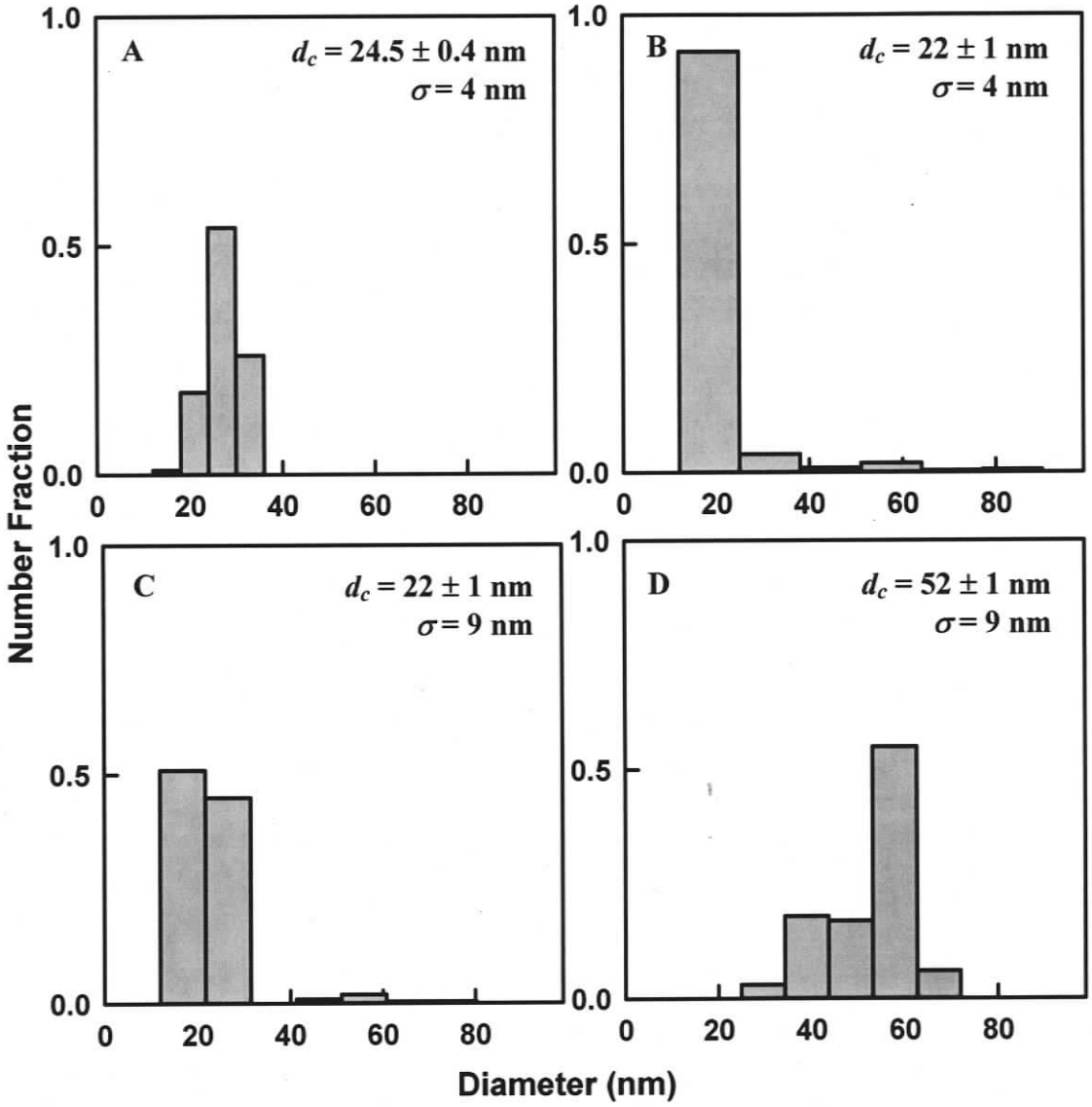

Figure 3.7. Particle size distributions for different blend compositions determined from analysis of several TEM images for blends represented in Figure 3.5 (C_0 = 0.5 wt%, $rate_{water}$ = 1.2 wt% / min): A) $f = 0$, B) $f = 0.1$, C) $f = 0.3$, D) $f = 0.5$.

mean LCM size from TEM size distribution analysis is $d_c = 52 \pm 1$ nm with a standard deviation of 9 nm. The error on the mean particle size was calculated from the standard deviation and number of particles sampled, using Eq. 2.15 for the 95% confidence interval. The standard distribution of the LCM population for $f = 0.5$ represents ~17% of the mean value, indicating that a distribution of LCM particle sizes is still present, even when a separate crew-cut micelle population does not form. The width of this distribution is comparable to that observed from LCM formation in the $f = 0.5$ blend after sonication of PS-CdS1 in the previous chapter (~18%), where no aggregates were present prior to water addition. DLS of the PS-CdS2 also suggests that the present sample is not aggregated before the secondary self-assembly step. We concluded in the last chapter that the presence of PS-CdS aggregates can result in a broader LCM distribution than when aggregates are not present. However, it appears that a size distribution of LCMs will be present even in the "best case". We believe this to be the result of the kinetic nature of size control in the process of LCM formation, growth, and freezing—following directly from the fact that there is no thermodynamically-determined optimum particle size in these samples. However, given the kinetic nature and inherent polydispersity of this process, we can still gain insight into the parameters which tend to broaden the distribution, and hopefully use this knowledge to obtain narrower LCM distributions in the SA2 self-assembly step. In the following sections, we investigate the potential for kinetic size control of LCMs, focusing now on the $f = 0.5$ blends, which give rise to a single LCM population without crew-cut micelle formation.

3.3.4. Control of Crew-Cut Micelle and Large Compound Micelle (LCM) Formation: Effect of Initial Polymer Concentration, C_0.

We attempted to control the sizes of LCMs via variation in the total initial polymer concentration. For LCM preparation, we used the blend composition $f = 0.5$; as well, we wished to investigate the effect of polymer concentration on crew-cut micelle formation from PS(665)-*b*-PAA(68) without PS-CdS2 present, which is the $f = 0$ case. This section therefore describes two series of experiments, one in which the constant blend composition is $f = 0$ and one in which the constant blend composition is $f = 0.5$. For each series, five different initial polymer concentrations were investigated: $C_0 = 0.5$, 1, 2, 3, and 4 wt%. To induce self-assembly for all experiments, water addition was carried out at a constant rate of 20 μL every 20 seconds ($rate_{water}$ = 1.2 wt% / min) and the CWC was noted by an increase in turbidity.

For the $f = 0$ blend (no PS-CdS2), the following CWCs were noted for the various initial polymer concentrations: $C_0 = 0.5$ wt%, CWC = 3.8 wt%; $C_0 = 1$ wt.%, CWC = 3.5 wt%; $C_0 = 2$ wt%, CWC = 3.5 wt%; $C_0 = 3$ wt%, CWC = 3.1 wt%; $C_0 = 4$ wt%, CWC = 2.3 wt%. These data show an increase in the CWC with polymer concentration as has been previously reported[2-7]. We note that the decrease in CWC with increasing polymer concentration is simply the direct result of block copolymers having a lower CMC (critical micelle concentration) in solvent mixtures containing more water; this arises due to unfavourable interactions between water and the hydrophobic PS chains, which increase the driving force for micellization as the water content increases. TEM of the dialyzed self-assembled $f = 0$ samples with initial polymer concentrations $C_0 = 0.5$, 2, 3, 4 wt% are shown in Figure 3.8A, 3.8B, 3.8C, and 3.8D, respectively. (The $C_0 = 1$ wt%

sample is not shown for convenience, but followed the observed trend) Again, the samples were shadowed with Pt/Pd prior to the images being taken. In all samples, a single distribution of small particles is observed, as expected for crew-cut micelle formation from the self-assembly of PS(665)-*b*-PAA(68) above the CWC. The TEM images appear to show a slight increase in the size of crew-cut micelles with initial polymer concentration, and this is confirmed by particle size distribution analysis of samples represented by the TEM images in Figure 3.8. The resulting distributions show a single population of particles which shift from d_c = 25 nm (Figure 3.9A) to d_c = 34 nm (Figure 3.9B) as the polymer concentration increases from C_0 = 0.5 wt% to C_0 = 4 wt%. This same series of crew-cut micelle preparations was repeated twice under identical conditions, and distribution analysis was also performed on TEM images of the repeat run. Average particle diameters from both runs are plotted in Figure 3.10, with the resulting experimental errors. The S-shaped curve shows a clear increase in crew-cut micelle size with initial polymer concentration, with an initial slight increase between 0.5 wt% and 1 wt%, a more significant increase between 1 wt% and 3 wt%, and a leveling off with no change between 3 wt% and 4 wt%.

The shape of the curve in Figure 3.10 can be understood by the combined role of thermodynamics and kinetics in determining the size of the crew-cut micelles. Unlike LCMs, the micelles will have an equilibrium particle size at a given water content, which is shifting to larger particles with increasing water content. Similar to LCMs, the dynamics of the chains becomes slower as more water is added due to a leaching of DMF from the core, with micelles becoming frozen on experimental time scales above a certain water content. For low initial polymer concentrations, the CWC is higher and therefore

relatively close to the water content at which the micelles become frozen; for a given rate of water addition, the micelles therefore do not have sufficient time to reach their equilibrium size at the point of freezing and therefore become kinetically trapped at a smaller particle size. In contrast, for the higher polymer concentrations, the CWCs are lower, and so the micelles have a wider window of time in which to grow, and are therefore able to reach their equilibrium size. This explains the increase in size with increasing polymer concentration, and also the fact that the increase shows a plateau above 3 wt%, indicating an equilibrium crew-cut micelle size (~ 33 nm) that can be attained given a sufficient window of growth. We stress that this "equilibrium size" represents the equilibrium that exists between micelle and single chains at the water content at which the micelles become frozen: as water is continually added above this point, and certainly in the purely aqueous dispersions that are represented by the TEM images, the micelles are no longer in equilibrium.

We now consider the effect of the initial polymer concentration on LCM formation in $f = 0$ blends of PS-CdS2 and stabilizing chains. The following CWCs were noted for the various initial polymer concentrations: $C_0 = 0.5$ wt%, CWC = 2.3 wt%; $C_0 =$ 1 wt%, CWC = 2.0 wt%; $C_0 = 2$ wt%, CWC = 1.6 wt%; $C_0 = 3$ wt%, CWC = 1.6 wt%; C_0 = 4 wt%, CWC = 1.2 wt%. Again, the expected decrease in the CWC with the initial polymer concentration is observed[2-7]. TEM of the dialyzed self-assembled $f = 0.5$ blends with initial polymer concentrations C_0 = 0.5, 1, 2, 3 wt% are shown in Figure 3.11A, 3.11B, 3.11C, and 3.11D, respectively. The C_0 = 4 wt% sample is not shown for convenience, but will be discussed in the following text. In all TEM images in Figure 3.11, a single distribution of particles is observed, which are known to be LCMs based on

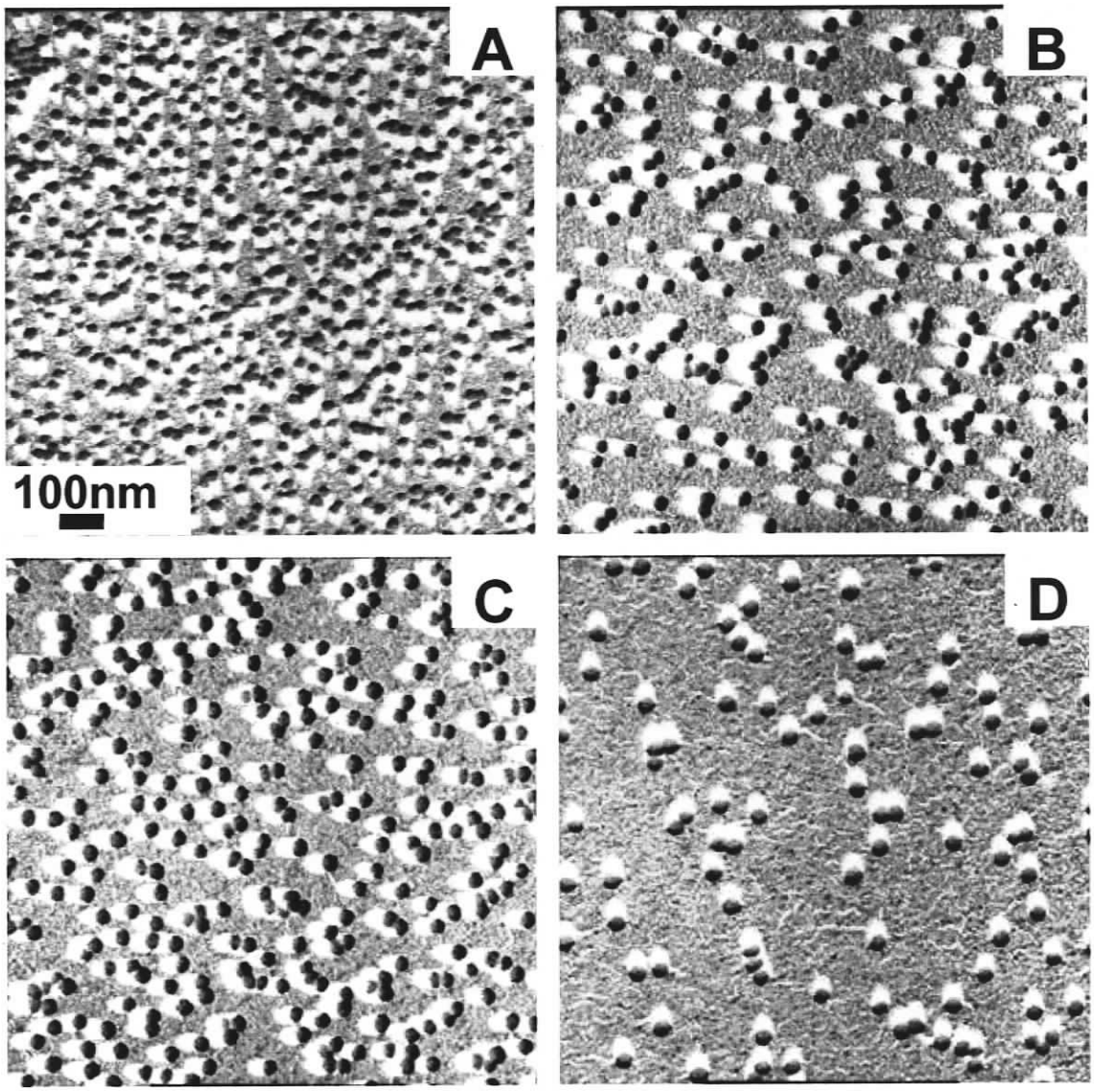

Figure 3.8. TEM images of colloids obtained from self-assembly of pure PS(665)-*b*-PAA(68) ($f = 0$) for various initial polymer concentrations: A) $C_0 = 0.5$ wt%, B) $C_0 = 2$ wt%, C) $C_0 = 3$ wt%, D) $C_0 = 4$ wt%. The rate of water addition was $rate_{water} = 1.2$ wt% / min.

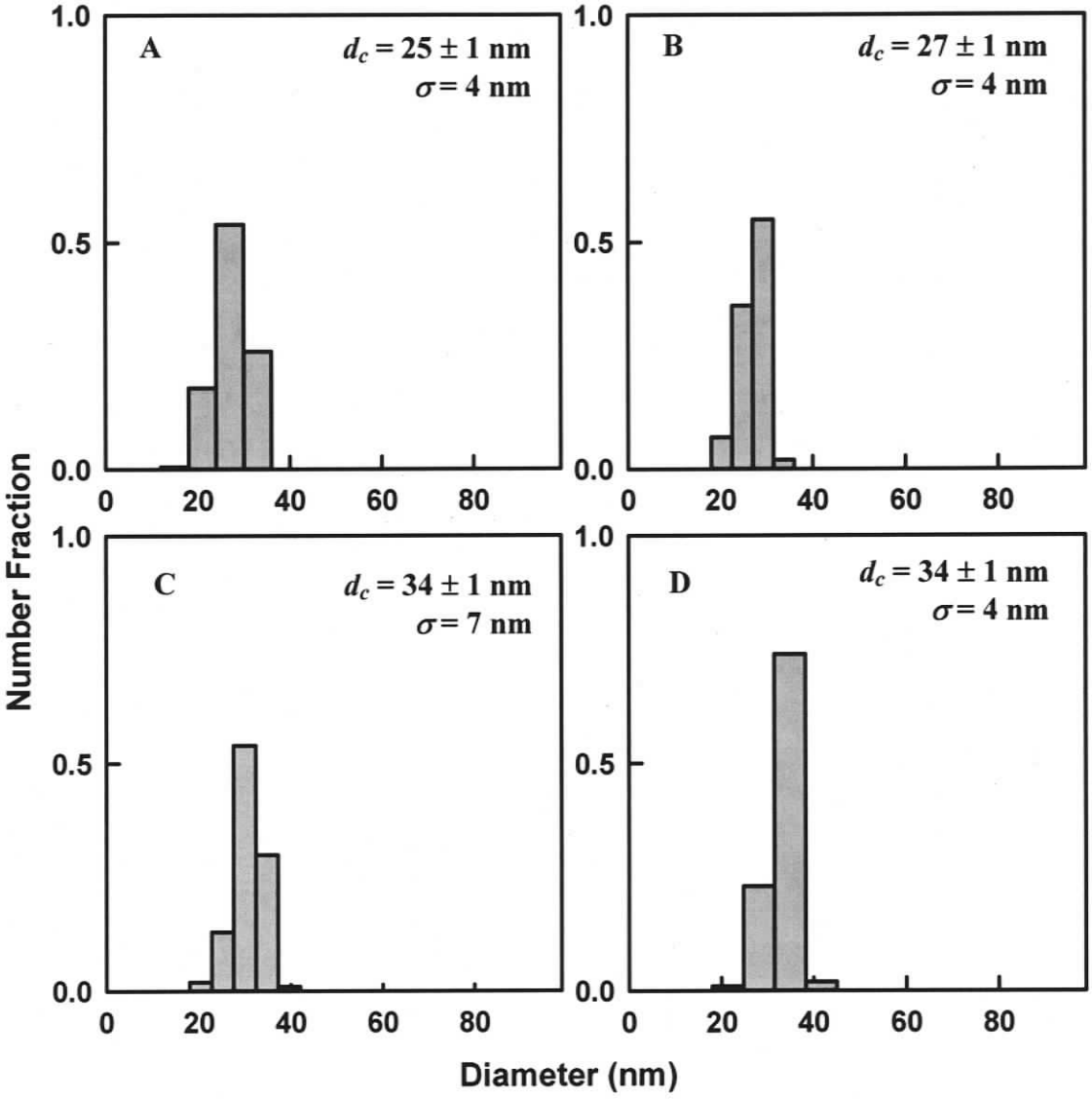

Figure 3.9. Particle size distributions for different initial polymer concentrations determined from analysis of several TEM images for crew-cut micelles represented in Figure 3.8 ($f = 0$, $rate_{water} = 1.2$ wt% / min): A) $C_0 = 0.5$ wt%, B) $C_0 = 2$ wt%, C) $C_0 = 3$ wt%, D) $C_0 = 4$ wt%.

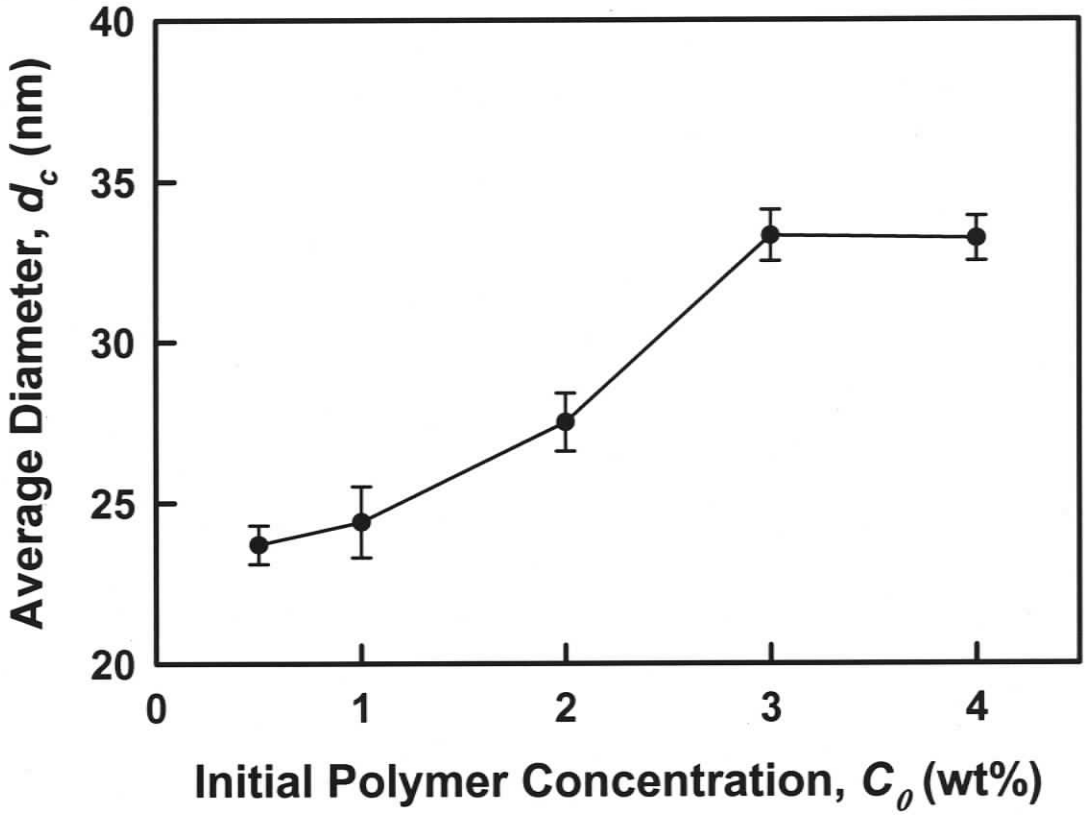

Figure 3.10. Plot of average of crew-cut micelle sizes ($f = 0$, $rate_{water} = 1.2$ wt% / min) from TEM size distribution analysis vs. initial polymer concentration, C_0. Errors are determined from two repeat experiments under identical conditions.

the discussion in the previous section. (Unshadowed TEM images of selected samples also confirmed that they possessed internal structure characteristic of CdS-containing assemblies, not shown). These images indicate a dramatic increase in LCM particle size as the initial polymer concentration increases; this is shown more quantitatively in the size distribution analysis in Figure 3.12. Figure 3.12 indicates an increase in the LCM diameter from d_c = 50 nm for C_0 = 0.5 wt% to d_c = 210 nm for C_0 = 3 wt%. It is also found that the width of the size distribution increases with C_0, from ~18% for C_0 = 0.5 to ~30% for C_0 = 3 wt%. The C_0 = 4 wt% sample, which is not represented in Figures 3.11 and 3.12, was also characterized by TEM, and found to contain extremely large and polydisperse particles which were agglomerated on the TEM grid and therefore impossible to characterize by particle size analysis.

Average particle diameters from two separate series of LCM preparations under identical conditions are plotted vs. the initial polymer concentration in Figure 3.13, with errors determined from half the difference of the two runs. This plot clearly shows the very reproducible trend of increasing LCM size with increasing initial polymer concentration. Unlike the crew-cut micelle case discussed earlier (f = 0, Figure 3.10), this plot does not appear to plateau and continues to sharply increase with C_0. (We note that the average particle sizes for C_0 = 4 wt% appeared to be much larger than those obtained for C_0 = 3 wt%, although they could not be properly characterized due to agglomeration on the TEM grid.)

The explanation for the observed increase in particle size is essentially the same as that given for the crew-cut micelle case, but with an important difference. Similar to crew-cut micelles, as the polymer concentration increases, the CWC is lowered, so that

LCM formation begins at an earlier point in the process of drop-wise water addition; the LCMs therefore have more time to reach a larger size before the particles are "frozen in". However, unlike the crew-cut micelle case, there is no equilibrium particle size for LCMs at any water content: the entropic penalty for chain stretching that exists in crew-cut micelles and regulates the particle size does not exist in LCMs, since the copolymer chains at the surface of LCMs do not have to stretch to maintain constant density within the particle (because the particle is "filled" by the aggregated PS-CdS2 particles). Therefore the only thermodynamic factor determining LCM size is interfacial energy, which will always favour larger particles. The particle sizes represented in the TEM images (Figure 3.11) and plotted in Figure 3.13 are therefore entirely determined by kinetics. The increase in polydispersity with increasing particle size can also be explained by the nonequilibrium nature of LCM particle growth, and suggests an agglomeration mechanism (rather than Ostwald ripening) for LCM growth. This demonstrates that LCM particle sizes obtained from secondary self-assembly of PS-CdS hybrid building blocks can indeed be tuned in a controlled and predictable manner via an increase in the initial polymer concentration, albeit at the expense of increased size polydispersity with increased average particle size.

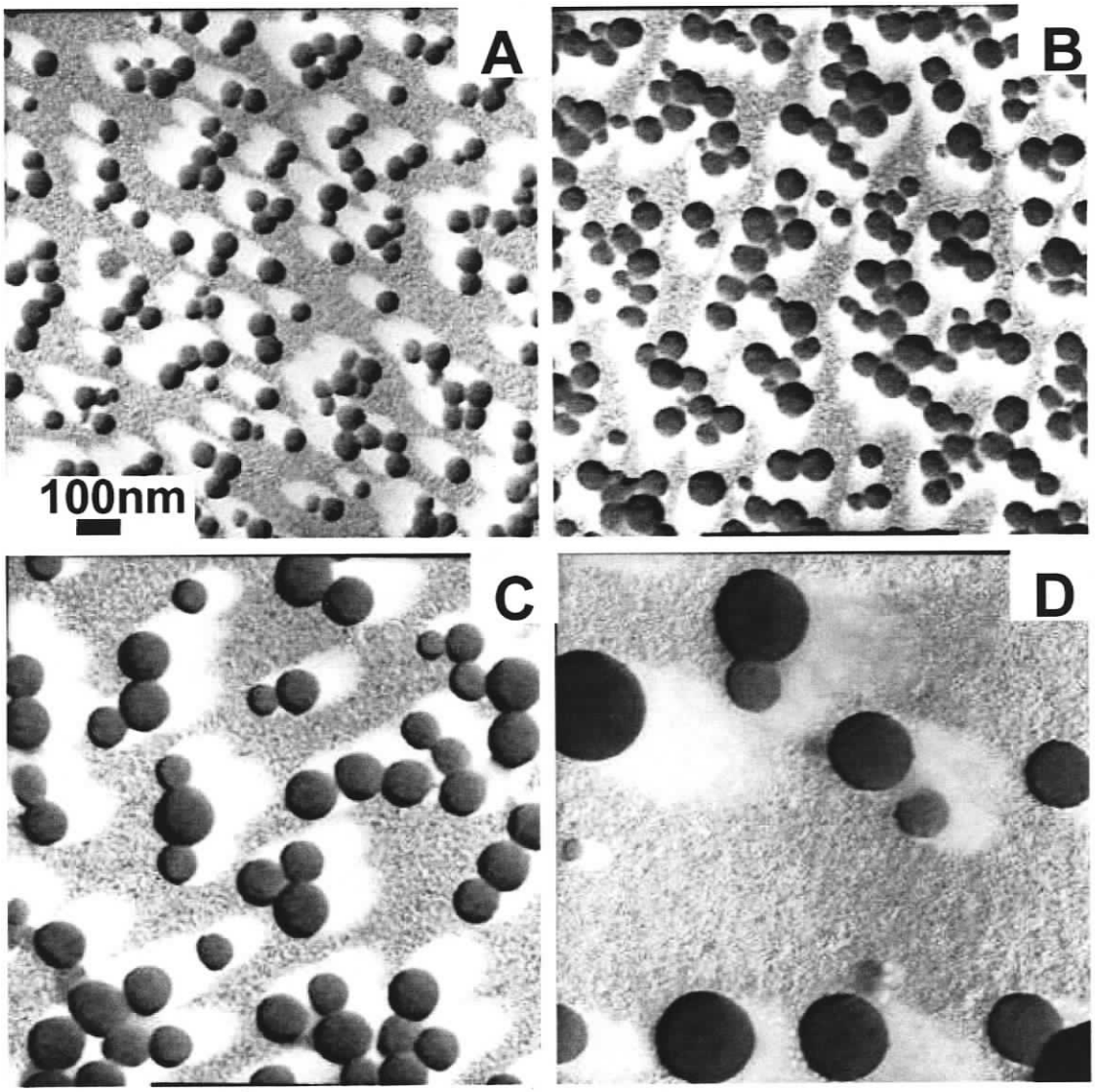

Figure 3.11. TEM images of colloids obtained from self-assembly of blends of PS-CdS2 and PS(665)-*b*-PAA(68) (f = 0.5, $rate_{water}$ = 1.2 wt% / min) for various initial polymer concentrations: A) C_0 = 0.5 wt%, B) C_0 = 1 wt%, C) C_0 = 2 wt%, D) C_0 = 3 wt%.

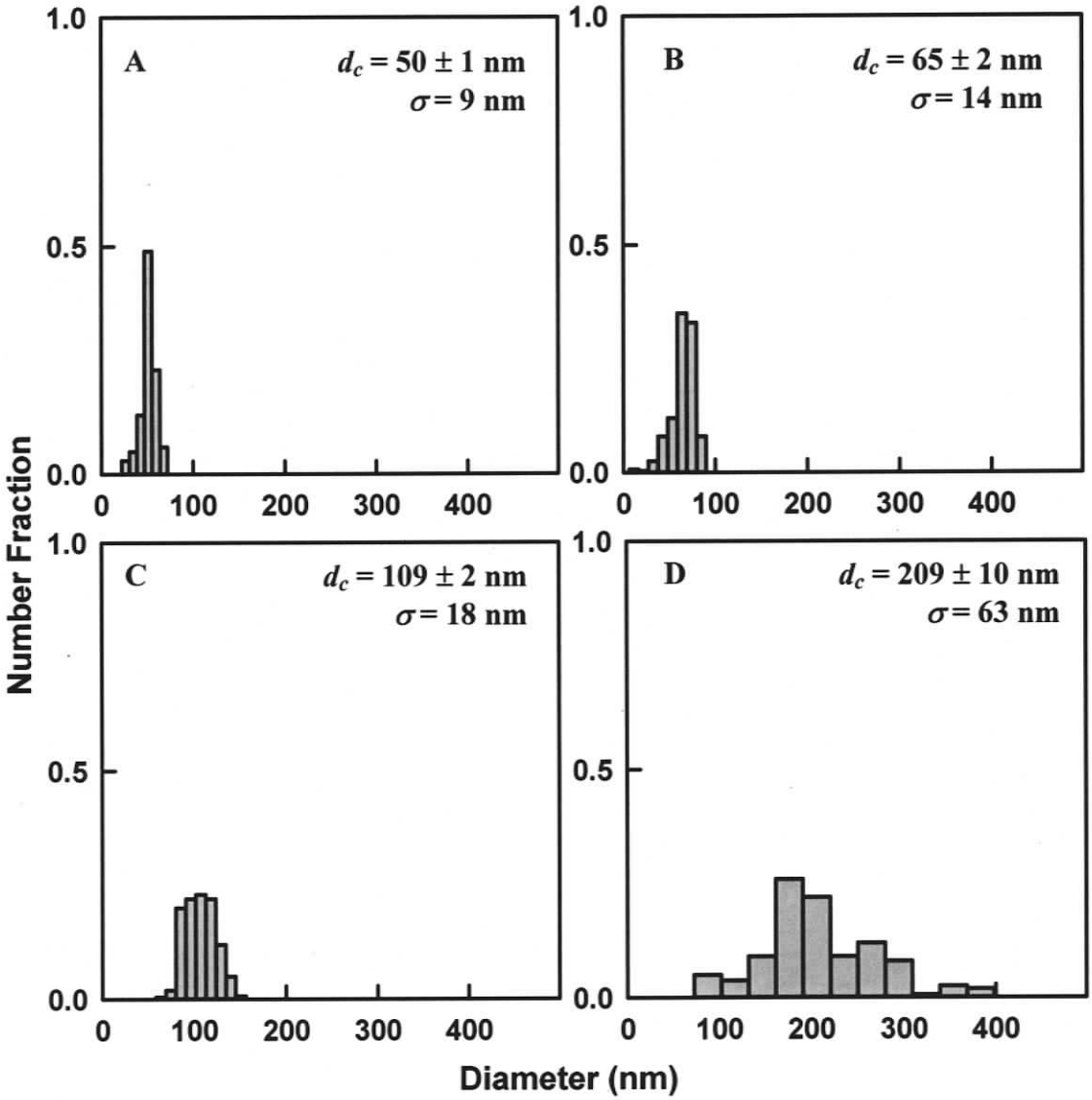

Figure 3.12. Particle size distributions for different initial polymer concentrations determined from analysis of several TEM images for blends represented in Figure 3.11 (f = 0.5, $rate_{water}$ = 1.2 wt% / min): A) C_0 = 0.5 wt%, B) C_0 = 1 wt%, C) C_0 = 2 wt%, D) C_0 = 3wt%.

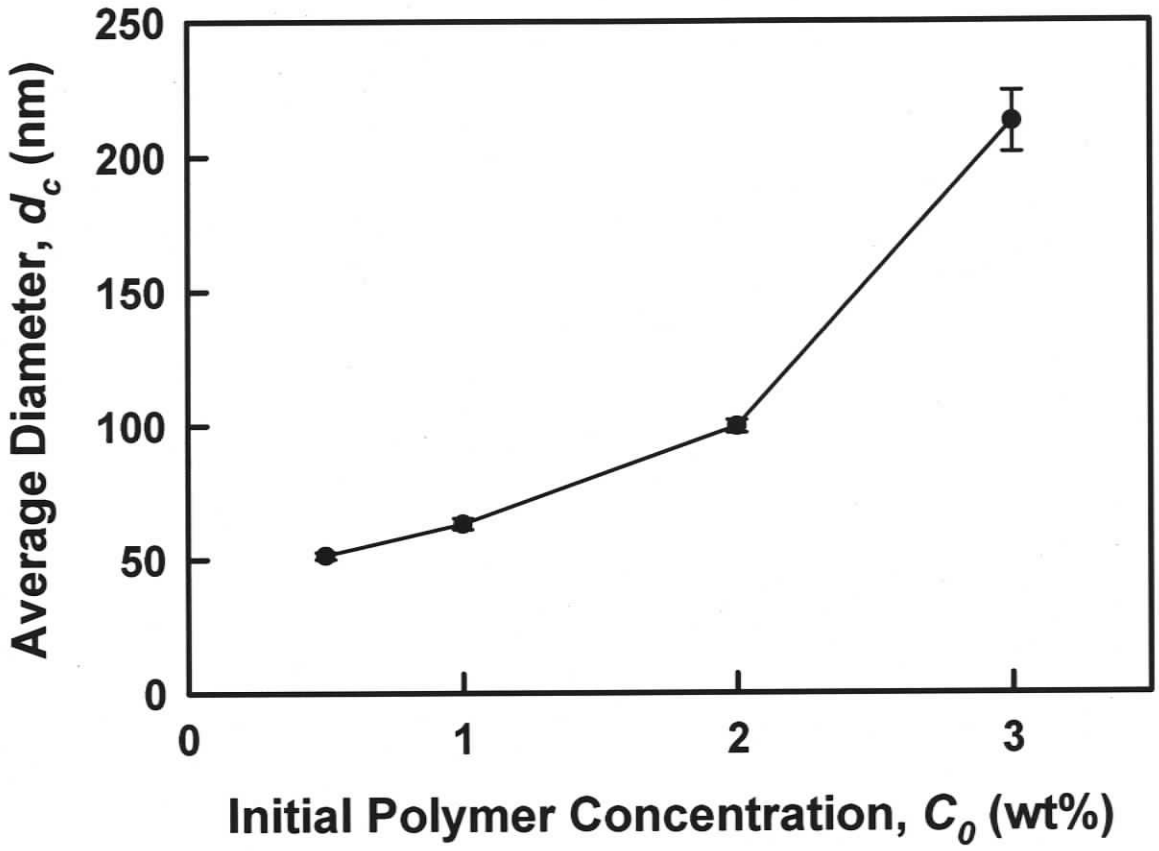

Figure 3.13. Plot of average of LCM sizes ($f = 0.5$, $rate_{water} = 1.2$ wt% / min) from TEM size distribution analysis vs. initial polymer concentration, C_0. Errors are determined from two repeat experiments under identical conditions.

From the tunable LCM particle sizes determined from TEM, we were also able to calculate the average number of PS-CdS2 particles, $n_{PS\text{-}CdS}$ within each LCM assembly. Since each PS-CdS2 is assumed to contain a single CdS nanoparticle, $n_{PS\text{-}CdS}$ is simply the number of CdS nanoparticles assembled within an LCM. The value of $n_{PS\text{-}CdS}$ for the various LCM samples obtained for C_0 = 0.5 wt%, 1 wt%, 2 wt% and 3 wt% were calculated directly from d_c, by first calculating the average volume of an LCM central core (i.e. excluding the PAA chains on the surface), V_c:

$$V_c = \frac{4}{3}\pi r_c^{\,3} \qquad (3.2)$$

where $r_c = d_c/2$ is the LCM core radius. From the volume, the mass of an LCM core is directly obtained assuming a density of ~1 g/mL (close to the bulk density of PS). The total LCM core mass is the sum of two components: 1) the mass of PS blocks from the PS(665)-*b*-PAA(68) stabilizing chains, and 2) the mass of aggregated PS-CdS2. To determine the mass contribution of PS-CdS2, the total LCM core mass is multiplied by 0.52, which is the weight fraction of PS-CdS2 within the core given that the total weight fraction of PS-CdS2 within each blend is f = 0.50 (the small difference is related to the fact that only the PS blocks of stabilizing chains are included in the mass of the LCM core). The resulting mass of PS-CdS2 within each LCM is then divided by the mass of a single PS-CdS2 particle, which is determined using the SLS-determined aggregation number of 54 ± 2. This gives the following $n_{PS\text{-}CdS}$ values for LCMs obtained for each of the initial polymer concentrations, with errors determined from a combination of

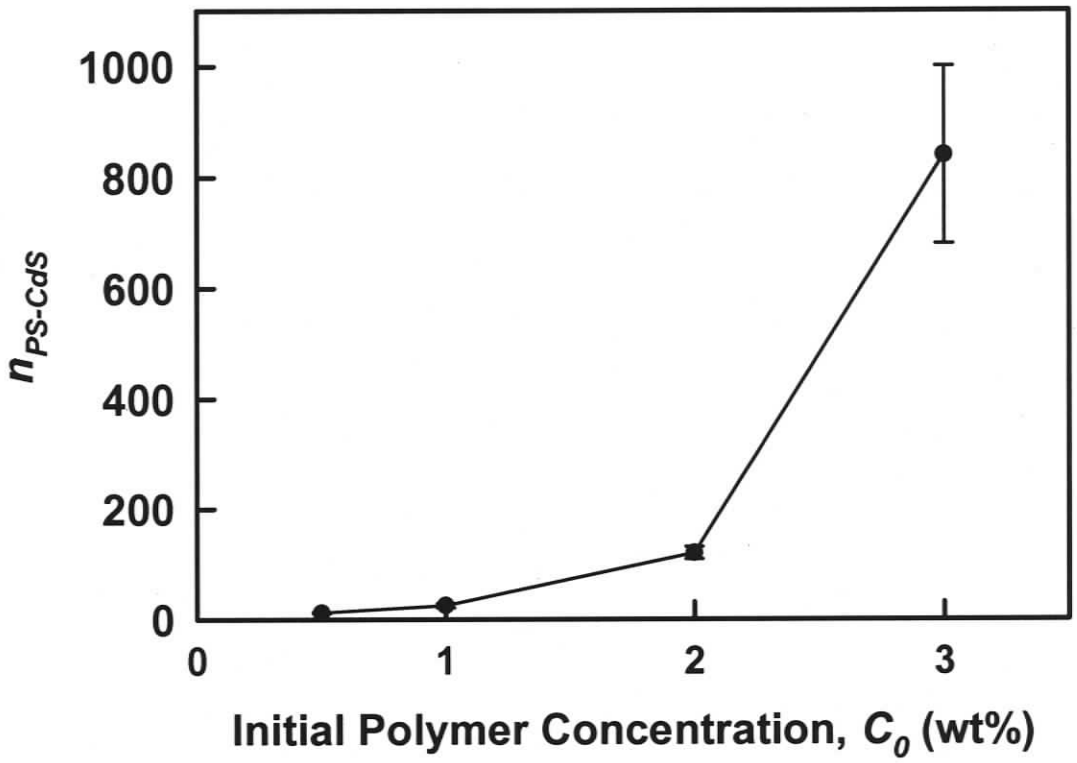

Figure 3.14. Average number of PS-CdS2 particles, $n_{PS\text{-}CdS}$ within each LCM assembly at different initial polymer concentration, C_0 (for all LCM preparation, $f = 0.5$, $rate_{water}$ = 1.2 wt% / min)

experimental errors on d_c (from TEM) and the aggregation number (from SLS): C_0 = 0.5 wt%, $n_{PS\text{-}CdS}$ = 12 ± 1; C_0 = 1 wt%, $n_{PS\text{-}CdS}$ = 25 ± 4; C_0 = 2 wt%, $n_{PS\text{-}CdS}$ = 120 ± 11; C_0 = 3 wt%, $n_{PS\text{-}CdS}$ = 840 ± 160. These values are plotted in Figure 3.14, highlighting the dramatic kinetic control over the average number of PS-CdS2 which self-assemble in the SA2 step. We note that a factor of 70 increase in $n_{PS\text{-}CdS}$ is obtained between C_0 = 0.5 wt% ($n_{PS\text{-}CdS}$ ~ 12) and C_0 = 2 wt% ($n_{PS\text{-}CdS}$ ~ 840), compared to only a factor of 4 increase in d_c within the same range of C_0. This is due to the d_c^3 scaling relation in the calculation of $n_{PS\text{-}CdS}$.

3.3.5. *Control of Large Compound Micelle (LCM) Formation: Effect of Speed of Water Addition, $rate_{water}$.*

We now demonstrate another strategy for kinetic control of LCMs, by varying the speed of drop-wise water addition, $rate_{water}$. For this series of experiments, the initial polymer concentration was constant at C_0 = 0.5 wt% and the composition was also constant at f = 0.5. The initial blend solutions in DMF were therefore identical for the five experiments in this series, with the speed of water addition being the only variable: $rate_{water}$ = 4.8, 2.4, 1.2, 0.6, or 0.4 wt% / min. TEM images of these experiments following dialysis were again obtained and all revealed a single distribution of LCM particles (not shown). Size distribution analysis was performed as shown in Figure 3.15A, 3.15B, 3.15C, and 3.15D for $rate_{water}$ = 4.8, 2.4, 1.2, and 0.4 wt% / min ($rate_{water}$ = 0.6 wt% / min is not shown for convenience and follows the observed trend). The four distributions show a gradual shift in the peak position to larger particles with decreasing rate of water addition, a trend which is also reflected in the average sizes, which shift

from d_c = 45 nm to d_c = 57 nm as the rate of water addition decreases from $rate_{water}$ = 4.8 to 0.4 wt% / min. However, compared to the dramatic effect of initial polymer concentration, the total shift in the average LCM size is small, ~12 nm, which is similar to the standard deviation of each distribution.

The shift in LCM particle size with the speed of water addition, like the effect of initial polymer concentration, is a kinetic effect related to the width of the window between the CWC and the point of water addition at which the particles are kinetically trapped. In this case, the CWC is the same for all solutions (since the initial blends are identical), so that the temporal window is controlled, not by the starting point of LCM formation, but by the rate of added water after the LCMs start to form: faster water addition gives the LCMs less time to grow before the "freezing" water content is reached, so that a smaller average size is obtained.

When this series of experiments was repeated under the same conditions, the same trend was observed (decreasing LCM size with increasing rate of water addition), and the average sizes from the two runs are plotted vs. $rate_{water}$, with the error on each point determined from half the difference between values for the repeat experiments (Figure 3.16). The large errors on these points indicate some variation between sizes obtained for the two runs; temperature variation between the different days on which each series of LCMs was prepared could explain the large experimental error. However, the clear trend indicates that the rate of water addition can indeed be used to control LCM sizes in secondary self-assembly of PS-CdS hybrid nanoparticles.

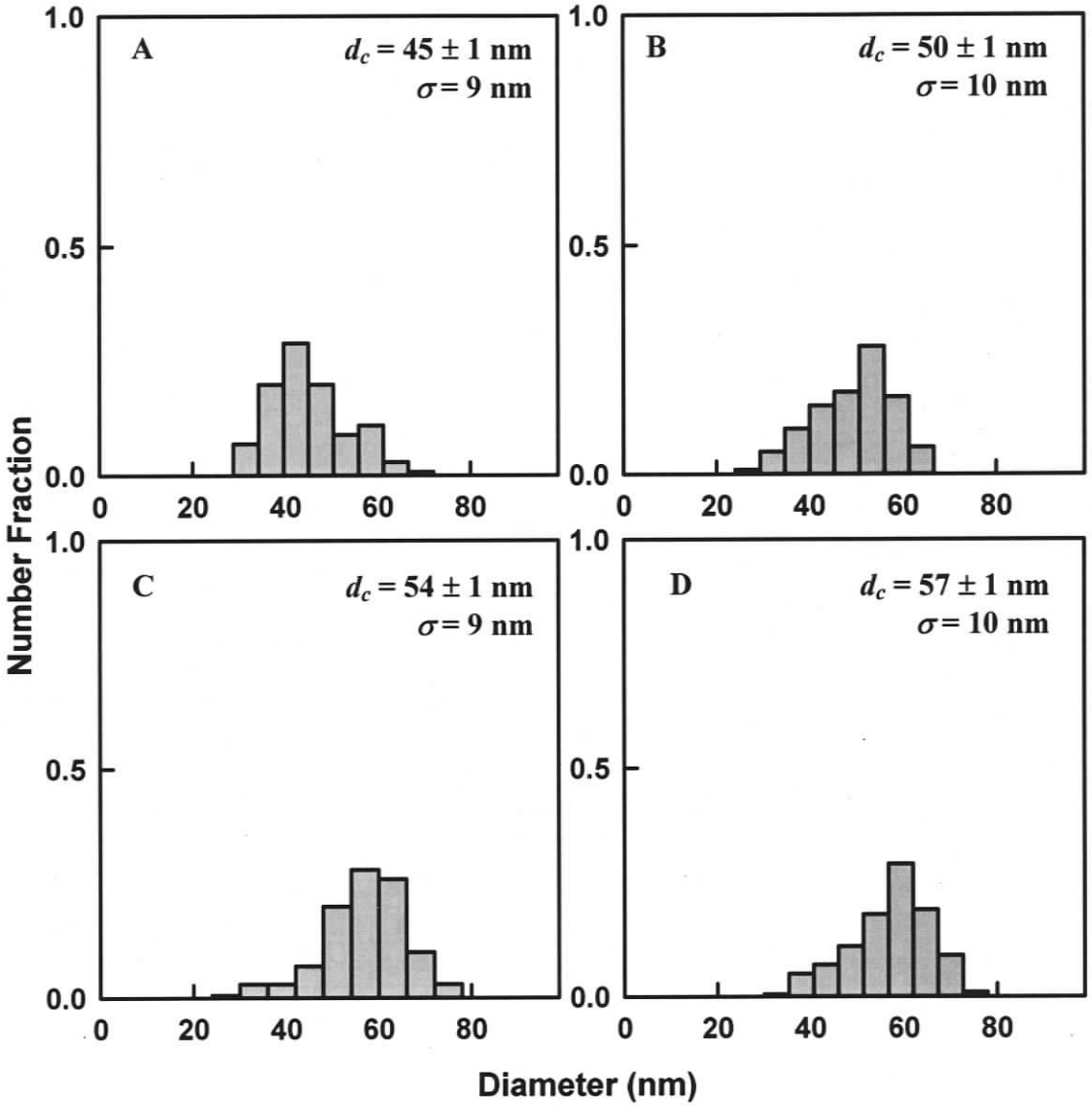

Figure 3.15. Particle size distributions determined from TEM images of colloids obtained from self-assembly of blends of PS-CdS2 and PS(665)-*b*-PAA(68) ($f = 0.5$, $C_0 = 0.5$ wt%) for different speeds of water addition: $rate_{water}$ = A) 4.8 wt% / min, B) 2.4 wt% / min, C) 1.2 wt% / min, and D) 0.4 wt% / min.

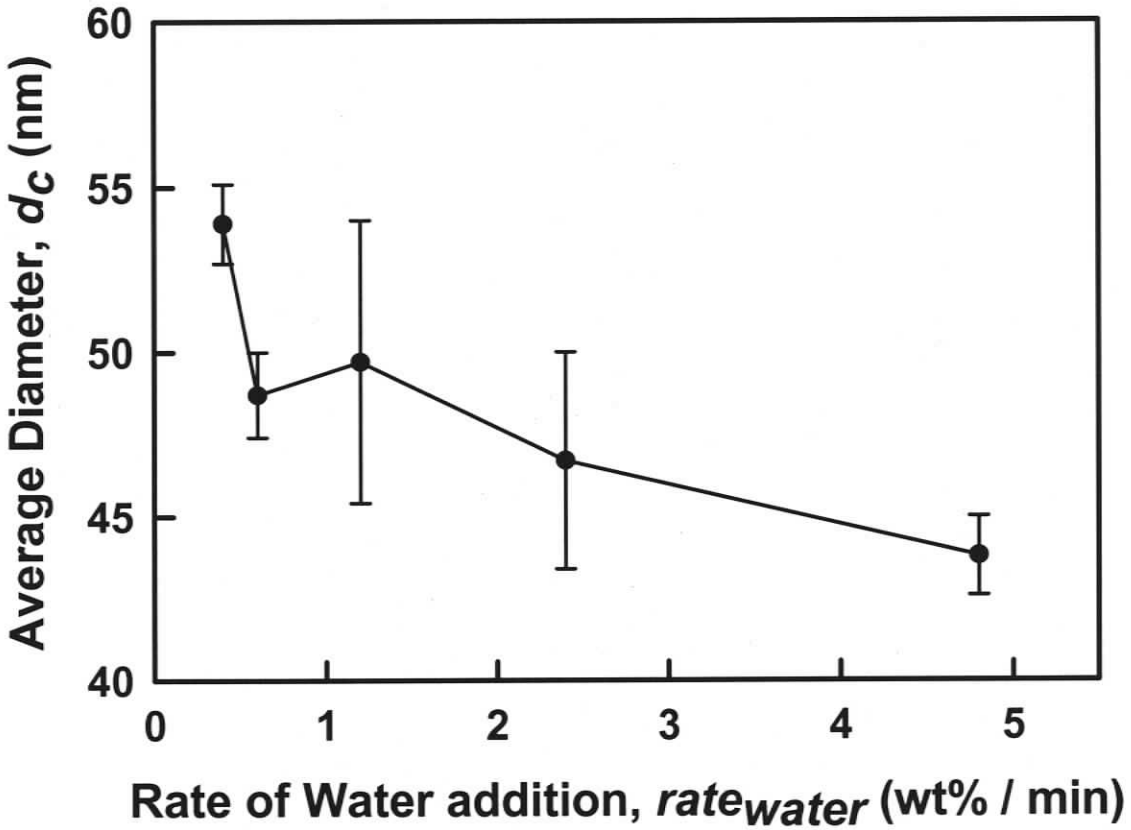

Figure 3.16. Plot of average LCM sizes (f = 0.5, C_0 = 0.5 wt%) from TEM size distribution analysis vs. rate of water addition, $rate_{water}$. Errors are determined from two repeat experiments under identical conditions.

3.3.6. Characterization of Large Compound Micelles via Dynamic Light Scattering (DLS).

LCM diameters determined by TEM, d_c, and reported in the previous sections are the sizes of the aggregated PS-CdS cores of the LCM (Scheme 3.1), and do not reflect the layer of PAA blocks from the PS(665)-*b*-PAA(68) stabilizing chains at the LCM surface. These PAA chains will be collapsed on the LCM surface under vacuum conditions during TEM imaging and will therefore not contribute significantly to the size of the particles as measured by TEM. However, the thickness of the solubilized PAA brush layer will significantly affect the size of the LCM particles in aqueous medium, and also the interactions between LCM particles during SA3 self-assembly to form a close-packed array. It was therefore of interest to determine the hydrodynamic diameters of various LCM particles, d_h, which will include both the core and the solvated PAA brush layer. By comparing these values with the LCM core sizes as determined by TEM, d_c, the thickness of the solubilized PAA brush can be determined. As well, based on the number of PAA repeat units in the stabilizing chains (68 repeat units), the percent extension of the PAA chains can be determined.

The LCM samples investigated for this analysis were those described previously in section 3.3.4, prepared from the blends f = 0.5, and various initial polymer concentrations, C_0 = 0.1 wt%, 1 wt%, 2 wt%, and 3 wt%, with a rate of water addition $rate_{water}$ = 1.2 wt% / min. The same series of samples described in the TEM images of Figure 3.11 and the size distributions of Figure 3.12 were investigated by DLS, which was one of two repeat series for this set of experimental parameters described in the earlier section. This set of samples was chosen due to the clear variation in particle size,

along with the fact each sample contained only one particle population (no crew-cut micelles).

Table 3.1 shows effective hydrodynamic diameters, d_h, of the LCMs prepared at various initial polymer concentrations, determined from cumulant analysis of the autocorrelation function at the single angle of 90° and a single dilute concentration in deionized water in the range 0.1 – 0.01 mg/mL. The sizes observed by DLS are consistently larger than those obtained by TEM for the same sample, as expected due to the contribution of the PAA brush layer in solution. As well, the hydrodynamic diameters are found to increase with C_0, which is the same trend observed for the particle size d_c from TEM (Table 3.1). Also shown in the table is the average thickness of the PAA layer, t_{PAA}, for each population of particles, calculated from the difference $t_{PAA} = r_h - r_c$ using the combination of DLS and TEM results; where r_h and r_c are the radii represented by one half the diameters d_h and d_c, respectively.

According to the diagram in Scheme 3.1, the thickness of the PAA layer is related to the degree to which the PAA blocks, attached at one end to the LCM surface, extend into solution. This extension involves a change in the conformation of PAA chains (≈ 0.03 in pure water[12]), which can be expected to be perturbed from their random coil configuration by a combination of steric and electrostatic interactions between charged PAA chains[3]. The pH the LCM solutions prepared with C_0 = 2 wt% and 3 wt% following dialysis against deionized water were measured and found to be pH = 6 for both LCM colloids. In aqueous media at pH > 4, linear PAA is partially ionized, with the degree of ionization increasing with pH[12]. Therefore the PAA chains in the LCM brush layer are expected to be negatively charged, resulting in electrostatic repulsion and extension of

neighboring chains within the brush. Since the brush thickness is equal to the average end-to-distance of PAA chains within the brush (Scheme 3.1), the degree of PAA chain extension was calculated as a fraction of the fully stretched PAA chain using the following formula:

$$\% \text{ extension} = 100 \times (t_{PAA}/[aN_{PAA}]) \qquad (3.1)$$

where t_{PAA} is the PAA brush thickness (calculated as describe above), N_{PAA} is the number of acrylic acid repeat units in the chains (N_{PAA} = 68) and a is the length of one fully extended acrylic acid repeat unit (a = 0.25 nm)[3]. The resulting percentage extension values are plotted for the various LCM samples of different average particle sizes (prepared at different. initial polymer concentration, C_0). This plot shows that for the larger LCM particles prepared from higher C_0, the PAA chains are close to 100% extended, indicating large repulsion between chains within the brush. The smallest LCMs prepared at C_0 = 0.5 wt% show the lowest percentage of extension, ~50%. It is not clear why smaller LCMs show less PAA chain extension, since the degree of ionization is expected to be similar in all cases. One possible explanation is that the smaller particles result in an LCM surface of higher curvature, which increases the free volume of PAA chains attached to the surface and therefore decreases inter-chain repulsion.

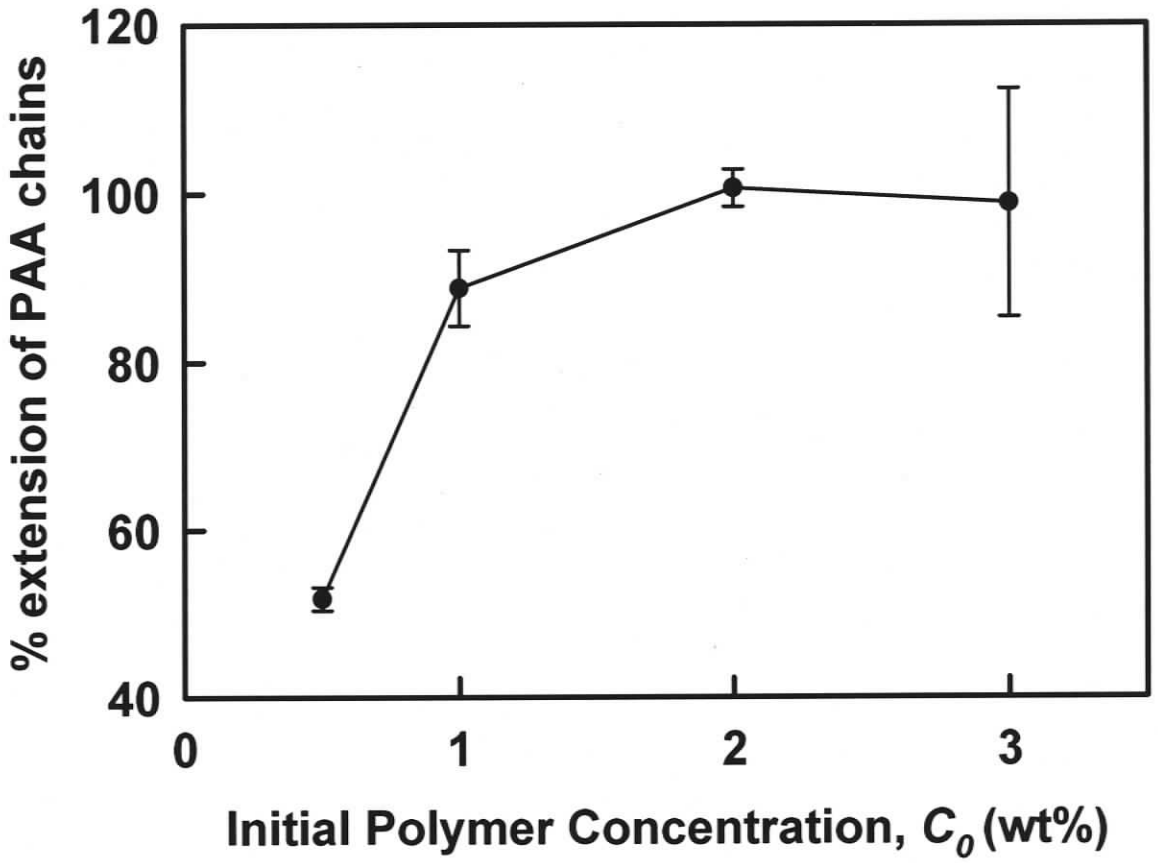

Figure 3.17. Percentage extension of PAA chains in the brush layer of LCMs prepared at different initial polymer concentrations C_0 (for all LCM preparations, $f = 0.5$, $rate_{water}$ = 1.2 wt% / min).

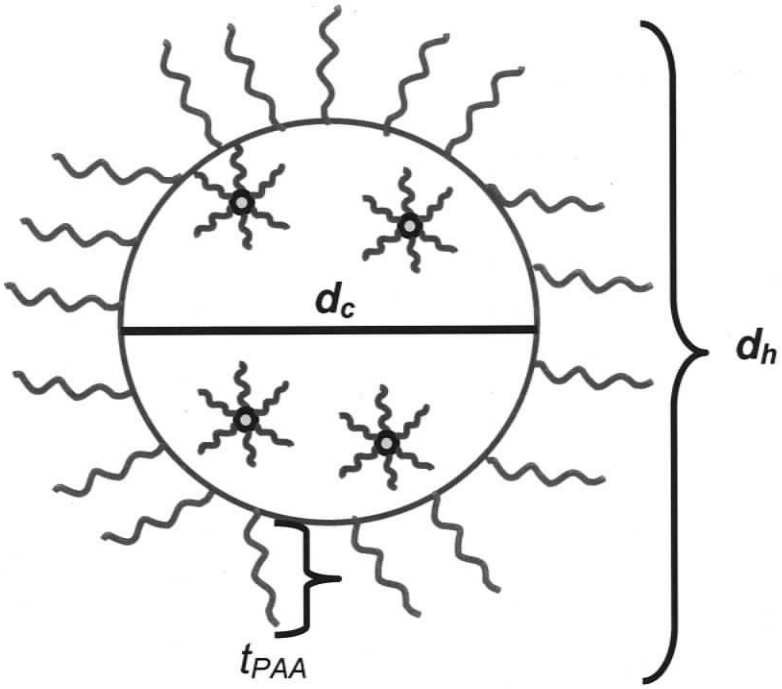

Scheme 3.1. Diagram of an LCM showing the diameter of the PS-CdS core region ($d_c = 2r_c$, as measured by TEM) and the overall hydrodynamic diameter ($d_h = 2r_h$, as measured by DLS). The difference $r_h - r_c = t_{PAA}$ gives the thickness of the PAA brush layer.

Table 3.1: DLS and TEM Results Summarizing the Structure of LCMs Prepared from PS-CdS2/PS(665)-*b*-PAA(68) Blends (f = 0.5, $rate_{water}$ = 0.12 wt% / min, various C_0 concentrations)

C_0	0.5 wt%	1 wt%	2 wt%	3 wt%
d_h (nm) (DLS)	68 ± 1	95 ± 4	143 ± 1	243 ± 9
d_c (nm) (TEM)	50 ± 1	65 ± 2	109 ± 2	209 ± 10
$t_{PAA} = r_h - r_c$	9 ± 1	15 ± 4	17 ± 2	17 ± 13

3.4. Conclusions

In this chapter, factors affecting the secondary self-assembly of hybrid PS-CdS nanoparticles (SA2) were investigated using the same PS(665)-*b*-PAA(68) stabilizing chains as in Chapter 2 but using a different sample of hybrid nanoparticles, PS-CdS2, prepared from the block copolymer PS(300)-*b*-PAA(12). Unlike the PS-CdS1 nanoparticles described in Chapter 2, static and dynamic light scattering results revealed that PS-CdS2 particles existed as free star-like particles in DMF, and no aggregates were detected prior to water addition.

The formation of LCMs by slow addition of water to various blends of PS-CdS2 and stabilizing chains in DMF was then investigated. We first studied the effect of blend composition while keeping the initial polymer concentration constant, and found that there was a critical weight fraction of PS-CdS2 ($f = 0.5$) which resulted in a single stable population of LCMs without crew-cut micelle formation from an excess of stabilizing chains. In addition, we demonstrated two effective strategies of kinetic LCM size control for the $f = 0.5$ blend systems: 1) average LCM sizes were increased by increasing the initial polymer concentration and 2) average LCM sizes were increased by decreasing the rate of water addition. Both of these strategies were based on tuning the width of the temporal window between the onset of LCM formation and LCM freezing.

Finally, single LCM populations of various sizes were investigated in aqueous media by DLS, in order to characterize the percent extension of PAA chains within the brush layer. For the larger LCM particles, the PAA chains were found to be nearly 100% fully extended, suggested stronger repulsive interactions between neighboring chains. The structure of the PAA brush will have important consequences in interparticle

interactions during self-assembly of LCMs into close-packed arrays in the SA3 step, to be described in the following chapter. There is a second population of a larger-sized particles present, which is due to the LCMs and at a certain composition (f = 0.5) there is only one population present which is the LCMs. Armed with this information, the effect of the initial polymer concentration of the system was studied by keeping the composition constant at f = 0.5 and varying the C_0 = 0.5 wt%, 1 wt%, 2 wt%, and 3 wt%. It was found that as the initial polymer concentration increases the sizes of the LCMs drastically increase and the distribution becomes much broader. It was also found that as the initial polymer concentration is increased the stretching of the coronal chains increases as well. Finally, the speed at which the water was being added was studied to see if it has an effect on the size of the LCMs and it was found that as the $rate_{water}$ is decreased the sizes of the LCMs increase which is not surprising due to the window of the LCM formation and being kinetically frozen increasing as the speed of water decreases.

References

1. Termonia, Y. *Macromolecules* **1997,** 30, 5367-5371.

2. Zhang, L.; Shen, H.; Eisenberg, A. *Macromolecules* **1997,** 30, 1001-1011.

3. Zhang, L.; Barlow, R. J.; Eisenberg, A. *Macromolecules* **1995,** 28, 6055-6066.

4. Zhang, L.; Eisenberg, A. *Journal of Polymer Science: Part B: Polymer Physics* **1999,** 37, 1469-1484.

5. Zhang, L.; Eisenberg, A. *J. Am. Chem. Soc.* **1996,** 118, 3168-3181.

6. Zhang, L.; Eisenberg, A. *Macromolecules* **1999,** 32, 2239-2249.

7. Zhang, W.; Shi, L.; An, Y.; Gao, L.; Wu, K.; Ma, R. *Macromolecules* **2004,** 37, 2551-2555.

8. Moffitt, M.; Eisenberg, A. *Chem. Mater.* **1995,** 7, 1178-1184.

9. Moffitt, M.; McMahon, L.; Pessel, V.; Eisenberg, A. *Chem. Mater.* **1995,** 7, 1185-1192.

10. Moffitt, M.; Eisenberg, A. *Macromolecules* **1997,** 30, 4363-4373.

11. Burchard, W. *Adv. Mater.* **1983,** 48, 1.

12. Philippova, O. E.; Hourdet, D. A., R.; Khokhlov, A. R. *Macromolecules* **1997,** 30, 8278-8285.

CHAPTER 4

Hierarchical Block Copolymer-Semiconducting Nanoparticle Arrays via a Tertiary Self-Assembly Step

4.1. Introduction

The organization of metallic and semiconducting nanoparticles (NPs) on multiple length scales is a critical step toward the application of these interesting building blocks in photonic devices[1-29]. The multi-step self-assembly strategy described in this work targets complex hierarchical structures in which organization of CdS nanoparticles on progressively longer length scales is introduced via a series of three self-assembly steps, each involving building blocks of increasing structural complexity (Scheme 4.1). A critical aspect of this strategy is that the first and second self-assembly steps (SA1 and SA2) each result in kinetically-trapped structures: this enables the structure and optical properties of the products of these two steps (block copolymer-stabilized CdS and large compound micelles, respectively) to be fully characterized before the external conditions for the subsequent self-assembly step are introduced. As well, the kinetic freezing of building blocks at each stage offers the potential for unique control of nanoparticle self-assembly within hierarchical materials, since organization introduced in each self-assembly step is "locked in", allowing structural features determined by the subsequent step to be independently tuned through a new set of experimental variables. Along with independent control of multiple length scales, an important feature of the current strategy is that the first self-assembly step (SA1) results in CdS nanoparticles coated with a stable block copolymer layer, so that the size and surface environment of the nanoparticles remains constant during subsequent steps. This will allow collective optical properties attributed to the spatial organization of nanoparticles (e.g. dipole-dipole interactions, interactions with photonic states with a bandgap structure)[30] to be unambiguously characterized, since changes in optical properties related to changes in the nanoparticle

surface environment, or to nanoparticle growth due to Ostwald ripening, will be prevented.

Chapters 2 and 3 of this thesis described the full characterization of block copolymer-stabilized CdS nanoparticles (PS-CdS) produced in the primary self-assembly step (SA1), along with the characterization of spherical assemblies of PS-CdS, termed large compound micelles (LCMs), produced in the secondary self assembly step. A key issue described in these earlier chapters was kinetic control of self-assembly of PS-CdS nanoparticles and PS-*b*-PAA stabilizing chains to form LCMs of controlled size and polydispersity. Chapter 2 demonstrated the effect of aggregation of PS-CdS nanoparticles prior to SA2 self-assembly on the polydispersity of LCMs. Chapter 3 presented two successful strategies for controlling the size of LCMs (and therefore the number of CdS nanoparticles within the assembly) formed by secondary self-assembly: It was found that larger LCMs could be obtained by increasing the initial polymer concentration or decreasing the rate of water addition. LCM dispersions of various average particle sizes were also characterized by dynamic light scattering (DLS) (Chapter 3), in order to determine the thickness of the stabilizing PAA brush layer surrounding each LCM. From these measurements, it was determined that PAA chains at the LCM surface were highly extended following dialysis against deionized water; this was attributed to ionization of acrylic acid groups and consequential electrostatic repulsion within and between PAA chains in the brush layer[29].

In this chapter, we demonstrate for the first time the feasibility of self-assembly of LCMs in a tertiary self-assembly step (SA3) to form a close-packed array of structurally-complex polymer/nanoparticle spheres with periodicities on the order of ~100 nm.

Tertiary self-assembly is induced by the slow evaporation of aqueous dispersions of kinetically-frozen LCM particles. Two LCM samples described in Chapter 3, with two different average LCM particle sizes are employed; both samples were produced from a 50/50 (w/w) blend PS-CdS2 nanoparticles and PS(665)-*b*-PAA(68) stabilizing chains by adding water at a constant rate of 1.2 wt% / min to blend solutions in DMF. The first sample, designated LCM2, was prepared using an initial polymer concentration of $C_0 = 2$ wt%, resulting in an average LCM particle size of $d_c = 109 \pm 2$ nm with a population standard deviation of $\sigma = 18$ nm. The second sample, designated LCM3, was prepared using an initial polymer concentration of $C_0 = 3$ wt%, resulting in an average LCM particle size of $d_c = 209 \pm 10$ nm with a population standard deviation of $\sigma = 63$ nm. DLS results described in the previous chapter suggested extensive electrostatic repulsive interactions within the PAA brush layer of both LCM samples following dialysis against deionized water; this suggests charging of the PAA brush following dialysis (at a measured pH ~6 for both samples), which will introduce repulsive electrostatic interactions between LCMs during SA3 self-assembly. We therefore investigated the effect of pH on the self-assembly of LCMs, comparing the results of tertiary self-assembly of LCM2 under conditions of acidic and near-neutral pH. Since both of the LCM dispersions obtained from secondary self-assembly have a significant polydispersity, we also investigated the effect of a pre-fractionation step to narrow the LCM size distribution.

This chapter will summarize structural characterization of the progressively more complex structures obtained from each stage of the multi-step self-assembly process, including SEM characterization of the final tertiary assemblies of LCMs. As well, the

fluorescence of CdS nanoparticles after each stage of self-assembly will be characterized. With demonstrated control on multiple length scales, the final hierarchical assemblies of periodic polymer spheres with CdS nanoparticles point the way to a new and interesting route to periodic bandgap structures with fluorescent nanoparticle inclusions, of interest for a range of photonic applications, including quantum dot lasers and all-optical switching[31, 32].

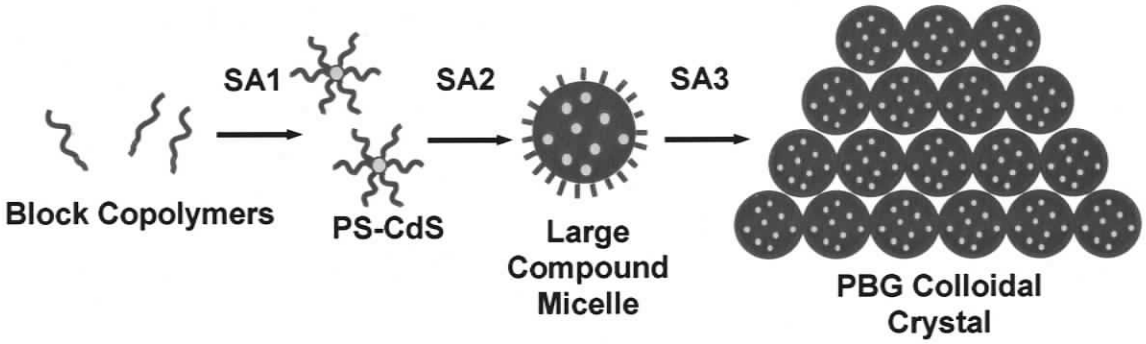

Scheme 4.1. Strategy to materials with multiple length scales.

4.2. Experimental

4.2.1. Preparation of Block Copolymer-Stabilized CdS Nanoparticles (SA1 Self-Assembly Step)

The preparation of PS-CdS2 nanoparticles from the self-assembly of PS(300)-*b*-PAA(12) block copolymer was described previously in Chapter 3. The resulting block copolymer-stabilized CdS nanoparticles consist of a CdS core, a poly(cadmium acrylate) surface layer and a polystyrene corona. Following SA1 self-assembly and synthesis of a CdS in each reverse micelle template, PS-CdS2 particles were characterized by static and dynamic light scattering (SLS and DLS), transmission electron microscopy (TEM), and UV-Vis and photoluminescence spectroscopy, as described in Chapter 3.

4.2.2. Preparation of Large Compound Micelles (LCMs) (SA2 Self-Assembly Step)

The preparation of the large compound micelles (LCMs) by SA2 self-assembly of PS-CdS2 was described in detail in Chapter 3. Two LCM samples described previously in Chapter 3 were employed in the study described in this chapter. Both samples were produced from a 50/50 (w/w) blend PS-CdS2 nanoparticles and PS(665)-*b*-PAA(68) stabilizing chains by adding water at a constant rate of 1.2 wt% / min with rapid stirring to blend solutions in DMF. The first sample was prepared using an initial polymer concentration of C_0 = 2 wt% (designated LCM2 in this chapter) and the second sample was prepared using an initial polymer concentration of C_0 = 3 wt% (designated LCM3 in this chapter). In both cases, water addition with stirring was continued above the CWC to a solution water content of 25 wt%, after which the LCM dispersions were dialyzed

against deionized water. The pH of the resulting aqueous dispersions of LCMs were measured and determined to be pH = 6 for both samples (using either a pH meter or pH paper). The LCMs thus obtained via SA2 self-assembly of PS-CdS2 were characterized by TEM and dynamic light scattering, as described previously in Chapter 3.

Following initial dialysis against deionized water, part of the LCM2 sample was then dialyzed against a pH = 4 buffer solution for 5 days, changing the buffer solution every day. The pH of the resulting LCM dispersion was measured and determined to be pH = 4 (using pH paper). Both LCM2 dispersions (pH = 6 and pH = 4) were used in SA3 self-assembly. For the LCM3 sample, only the dispersion after dialysis against deionized water (pH = 6) was used in subsequent self-assembly of LCMs.

Prior to SA3 self-assembly by slow water evaporation, all LCM samples were concentrated from the original dispersions following dialysis (7.11 mg/mL for LCM2 and 9.85 mg/mL for LCM3) to a solids content of ~10 wt%. One of two methods was used to concentrate the LCM dispersions: 1) in the first method, the LCM sample was roto-evaporated from its original solids content directly to a concentration of ~10 wt%; 2) in the second method, the LCM sample was roto-evaporated to dryness, followed by addition of deionized water or pH = 4 buffer to a final concentration of ~10 wt%. In the second case, it was found that some of the LCM sample could not be re-suspended following evaporation to dryness and remained as a precipitate in the vial. It is suspected that this remaining fraction was made up of LCM particles at the high end of the particle size distribution which agglomerated during evaporation to dryness. The evaporation-to-dryness step thus constituted a particle size-selection process, resulting in narrower LCM size distributions for SA3 self-assembly.

4.2.3. Preparation of Close-Packed Assemblies of LCMs (SA3 Self-Assembly Step)

The glass slides which would serve as substrates for self-assembly of LCMs were cleaned by sonication in 95% ethanol for 10 min, followed by sonication in deionized water for another 10 min. The glass slides were then submerged directly into a piranha solution for 10 min (piranha solution consisted of a 3:1 v/v mixture of H_2SO_4 and 30% H_2O_2). The glass slides were then washed repeatedly with deionized water and methanol, dried with UHP N_2, placed in a glass Petri dish, and finally dried overnight at 50°C under active vacuum.

Various LCM dispersions (10 wt% solids content) were used to prepare tertiary assemblies in the following manner: two drops of the LCM dispersion, each with a volume of 20 μL, were deposited onto the cleaned glass slides arranged in a Petri dish and spread evenly over the slide. In the same Petri dish on another glass slide, a few drops of concentrated KNO_3 solution were deposited; this solution served as a source of water vapour to maintain high humidity in the Petri dish for slow water evaporation. The Petri dish was then covered and placed in a dark cupboard for one week allowing the drops to dry slowly.

4.2.4. UV-Vis Absorption and Photoluminescence Measurements

All absorption spectra were recorded on a Cary 50-scan UV-Vis spectrophotometer. Absorption spectra of the PS-CdS2 sample in toluene solution were obtained using spectroscopic grade toluene with pure spectroscopic grade toluene subtracted as the background. For the LCM dispersions, deionized water was subtracted as the background. UV-vis spectra of the tertiary LCM assemblies on glass could not be

obtained due to large scattering (thick films) or insufficient signal (thin films) from the deposited films.

Static fluorescence measurements were recorded on an Edinburgh Instruments FLS 920 instrument equipped with a Xe 450 W arc lamp and a red sensitive PMT (R928-P). All spectra were recorded at an excitation wavelength of λ_{ex} = 400 nm at 1 nm spectra resolution using a 425 nm filter. For measurement of fluorescence following SA1 self-assembly, the PS-CdS2 sample was dispersed in spectroscopic grade toluene at a concentration such that the measured absorbance at 400 nm was less than 0.1; this was to keep the concentration low enough so that the auto-absorption effects were minimized. The resulting fluorescence spectrum was then solvent-subtracted using a background measurement of pure spectroscopic grade toluene. For measurement of fluorescence following SA2 self-assembly, the LCM dispersions were diluted by a factor of 2 following dialysis with deionized water; to obtain the final spectrum, a background of deionized water was subtracted. Finally, for measurement of fluorescence following SA3 self-assembly, the tertiary assembly films were excited from the sample side of the glass substrate at an angle of ~45° to the film, with fluorescence detected at an angle of 45° to the excitation beam. A spectrum of the glass slide using the same excitation and detection angles was collected and subtracted from the final spectra.

4.2.5. Transmission Electron Microscopy

TEM of PS-CdS2 particles were obtained by depositing dilute solutions (5 mg/mL) of PS-CdS2 in benzene onto carbon substrates (without formvar) on a copper

TEM grid. The particles were then imaged on a FEI Tecanai STEM, operating at an accelerating voltage of 200 keV.

For TEM imaging of LCM colloids, LCM2 and LCM3 dispersions were diluted to a concentration of 0.5 mg/mL and then a 10 μL drop was deposited on carbon-coated formvar on a 300 mesh copper grid. To characterize LCM internal structure, the samples were imaged without Pt/Pd shadowing using the TEM instrument described above. The same LCM colloids were also imaged with Pt/Pd shadowing to obtain optimum contrast between the particles and the substrate for particle size and distribution analysis. LCM samples with Pt/Pd shadowing were imaged using on a Hitachi H-700 electron microscope, operating at an accelerating voltage of 75 kV.

4.2.6. Scanning Electron Microscopy

Scanning electron microscopy (SEM) was performed using a Hitachi S-3500N instrument. Before imaging, tertiary LCM assemblies (following the SA3 step) on glass were coated with gold using an Edwards S150B Sputter Coater.

4.3. Results and Discussion

4.3.1. Characterization of Block Copolymer-Stabilized CdS Nanoparticles (PS-CdS2) Following SA1 Self-Assembly.

The first step in our multi-step self-assembly process (primary self-assembly, SA1) was the formation of block ionomer micelles from PS(300)-*b*-PAA(12) block copolymers in a benzene/methanol solvent mixture. Self-assembly was induced by the addition of cadmium acetate, which deprotonated the acrylic acid groups, resulting in negatively charged blocks which spontaneously self-assembled to form the core of a reverse micelle. A single cadmium sulfide nanoparticle was then synthesized in the core of each micelle, followed by re-neutralization of the PAA blocks with cadmium acetate; this re-neutralization stabilizes the micelle by decreasing the solubility of the core-forming blocks and is also known to improve the quantum yield of the nanoparticles[33]. The resulting hybrid nanoparticle is designated PS-CdS2, with a structure represented in Scheme 4.2. The detailed characterization of PS-CdS2 was described previously in Chapter 3, and the resulting structural characteristics are summarized in Table 4.1. This combination of results indicates various length scales and structural characteristics determined by SA1 self-assembly. Some of these features, including the size of the CdS nanoparticles (r_{CdS} = 2.0 nm) and the number of PS(300)-*b*-PACd(12) chains surrounding each nanoparticle (Z = 54), will remain constant in subsequent self-assembly steps, since the PS-CdS2 nanoparticle is "frozen" in the sense that single chains cannot escape from

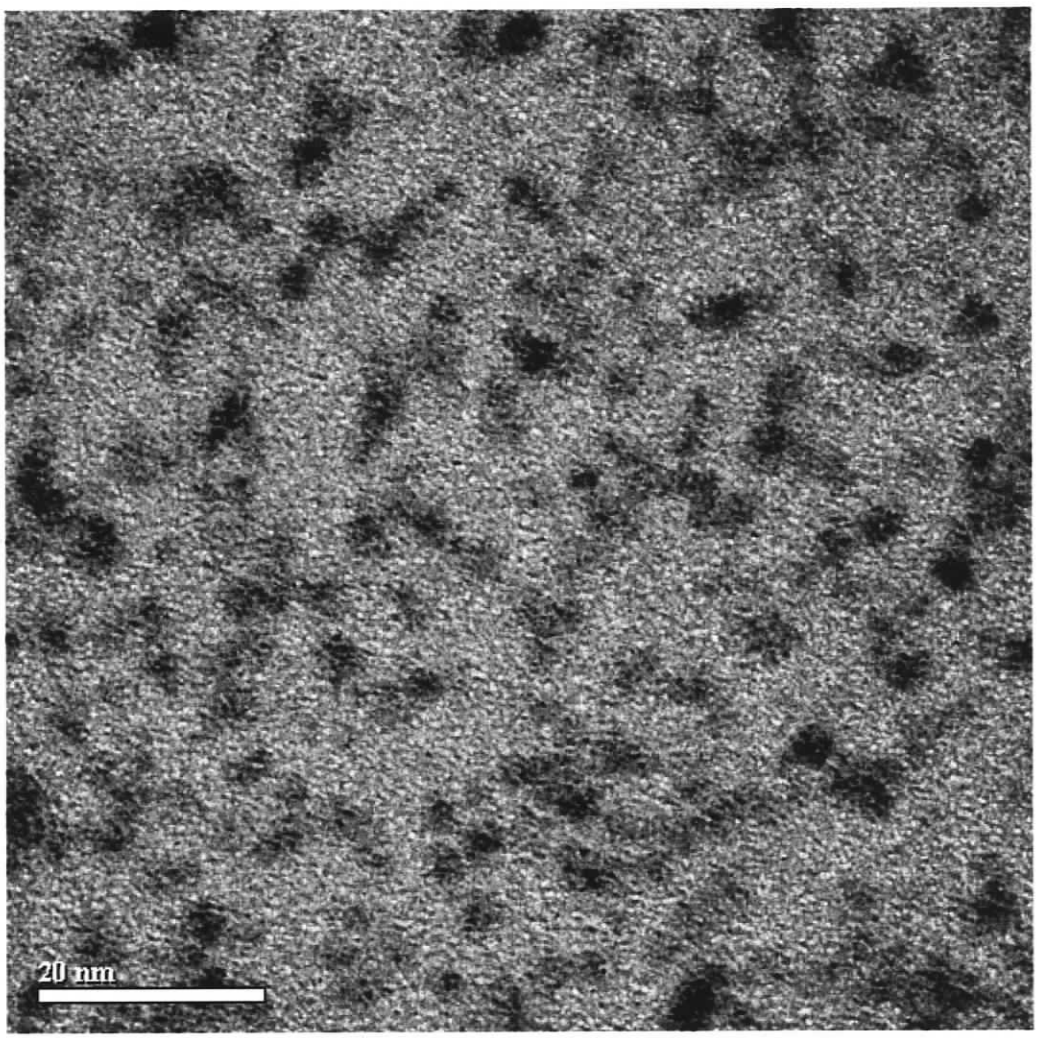

Figure 4.1. TEM image of PS-CdS2 nanoparticles cast from benzene solvent.

the micelle on a reasonable time scale, irrespective of changes in the external environment; this is attributed to the high glass transition temperature of the PACd layer and strong ionic interactions between the CdS nanoparticle and cadmium carboxylate groups at the surface[33]. However, we note that other structural characteristics described in Table 4.1 (r_g and r_h) depend on the chain conformation of the PS blocks, which will vary depending on the quality of the surrounding solvent (reported for PS-CdS2 in DMF). For example, subsequent self-assembly of PS-CdS2 to form LCM particles by water addition will begin with the collapse of PS chains surrounding each nanoparticle in order to minimize interactions with the increasingly hydrophilic solvent mixture; despite this conformational change and the subsequent aggregation of PS-CdS2 particles, the structural integrity of PS-CdS2, and as a result the average size of the CdS nanoparticles,

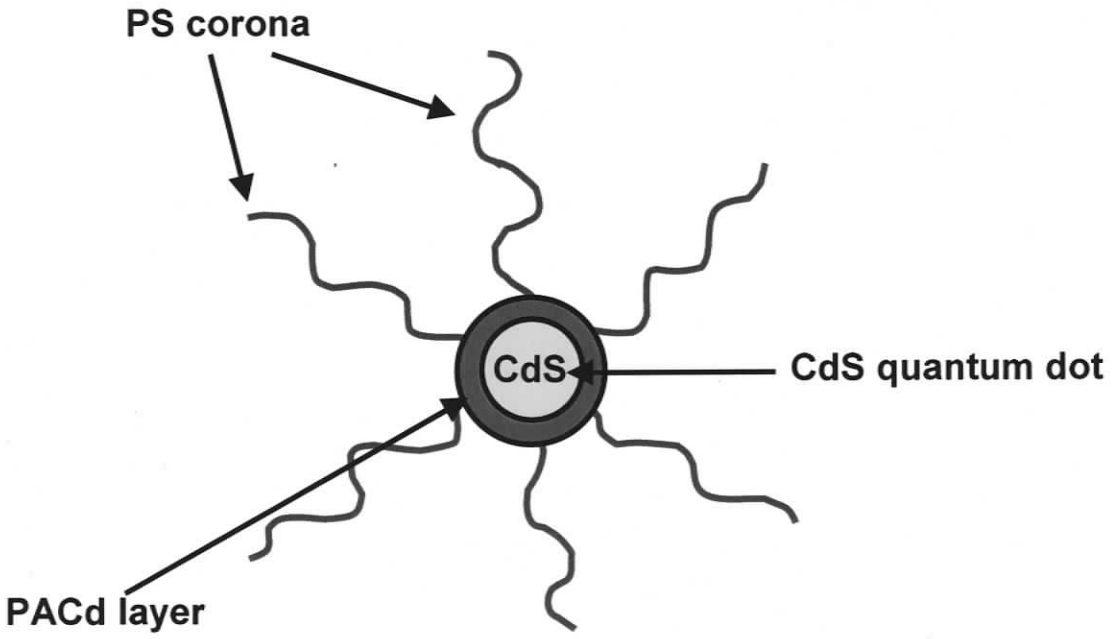

Scheme 4.2. Representation of the hybrid PS-CdS2 particles produced in the primary self-assembly step.

will remain constant. Figure 4.1 shows a TEM image of individual PS-CdS2 nanoparticles deposited onto a carbon substrate from a dilute benzene solution. Each of the electron-dense dark spots represents the CdS core of a single PS-CdS2 nanoparticle. From the TEM image, the average diameter of the CdS nanoparticles is ~2.9 nm, in reasonable agreement with the size reported in Table 4.1, which was determined from the UV-Vis spectra of PS-CdS2 dispersed in toluene.

Table 4.1: Structural Characteristics of PS-CdS2

N_{PS}[a]	N_{PAA}[b]	M_w[c] (g/mol)	Z[d]	r_g[e] (nm)	r_h[f] (nm)	r_g/r_h	r_{CdS}[g] (nm)
300	12	$1.78 \pm 0.06 \times 10^6$	54 ± 2	21 ± 8	18 ± 1	1.2 ± 0.4	2.0

a. **number-average degree of polymerization of PS coronal chains (SEC)**
b. **number-average degree of polymerization of PAA chains at CdS surface (FTIR)**
c. **weight-average molar mass of PS-CdS2 in DMF (SLS)**
d. **chain aggregation number of PS-CdS2 (SLS)**
e. **average radius of gyration of PS-CdS2 in DMF (SLS)**
f. **z-average hydrodynamic radius of PS-CdS2 (DLS)**
g. **average radius of CdS nanoparticles in PS-CdS2 core (UV-vis)**

4.3.2. Characterization of Large Compound Micelles (LCM2 and LCM3) Following SA2 Self-Assembly.

The second step in the multi-step self-assembly process (secondary self-assembly, SA2) was the formation of spherical assemblies of PS-CdS2 nanoparticles via the slow addition of water to blend solutions of PS-CdS2 and PS(665)-*b*-PAA(68) stabilizing chains in DMF. The increasingly unfavourable interactions between PS chains and the surrounding solvent drives the self-assembly, which is a phase separation process

mediated by the stabilizing chains which localize at the polymer/solvent interface. The general structure of the resulting secondary assemblies is shown in Scheme 4.3, which

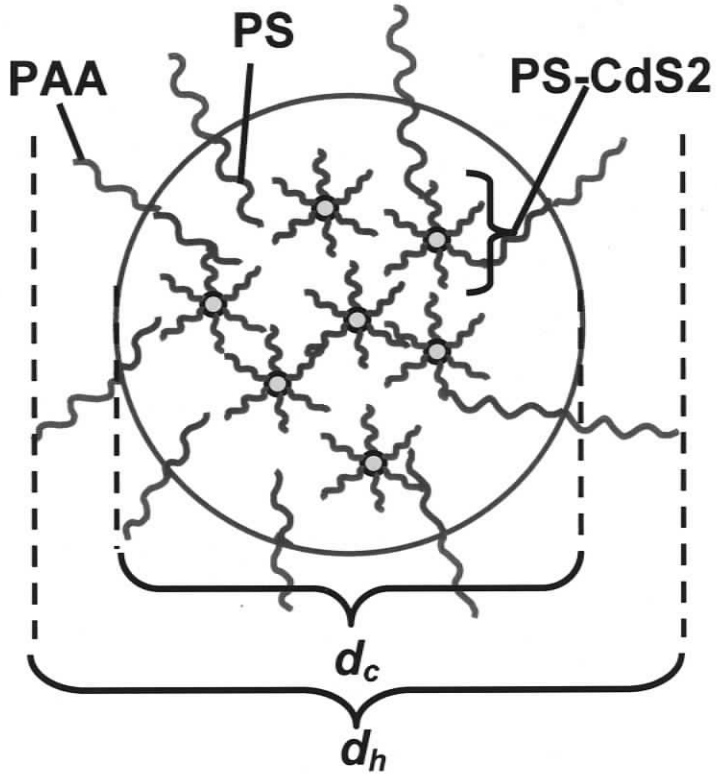

Scheme 4.3. Representation of a large compound micelle (LCM) produced in the secondary self-assembly step.

shows that LCMs are hierarchical structures with structural features on multiple length scales: the interior of each spherical LCM consists of multiple assembled PS-CdS2 particles, which form a PS matrix made up of the PS blocks of PS-CdS2 in which CdS nanoparticles contained within hydrophilic compartments are dispersed. The average nearest-neighbor CdS-CdS interparticle spacing within the LCM spheres is determined

solely by the length of the PS hair surrounding each PS-CdS2 component and the chain aggregation number of each PS-CdS2 particle; assuming a body-centered cubic arrangement of CdS nanoparticles and an LCM internal density of 1 mg/mL, and using the molar mass per PS-CdS2 determined from SLS (Table 4.1), the nearest neighbor spacing between CdS nanoparticles within secondary assemblies of PS-CdS2 is calculated to be 12 nm. This number is independent of the LCM size and the number of particles within the assembly.

Figure 4.2 shows shadowed and unshadowed TEM images of the two LCM samples employed in this study, prepared under different conditions of SA2 self-assembly. Both samples were prepared from a 50/50 (w/w) blend PS-CdS2 nanoparticles and PS(665)-*b*-PAA(68) stabilizing chains dispersed in DMF, with self-assembly induced via a constant rate of water addition of 1.2 wt% / min. To remove DMF from the samples, they were dialyzed for several days against deionized water once water had been added drop-wise to 25 wt%. The first sample (Figure 4.2A and C, LCM2) was prepared using an initial polymer concentration of C_0 = 2 wt%, and has a measured average LCM core diameter of 109 ± 2 nm (with $\sigma \sim 17\%$) from TEM, from which the average number PS-CdS2 particles within the assembly is determined to be 120 ± 11. The second sample (Figure 4.2B and D, LCM3) was prepared using an initial polymer concentration of C_0 = 3 wt%, and has a measured average LCM core diameter of 209 ± 2 nm (with $\sigma \sim 30\%$) from TEM, from which the average number of PS-CdS2 particles within the assembly is determined to be 840 ± 160. TEM images of both particle samples without Pt/Pd

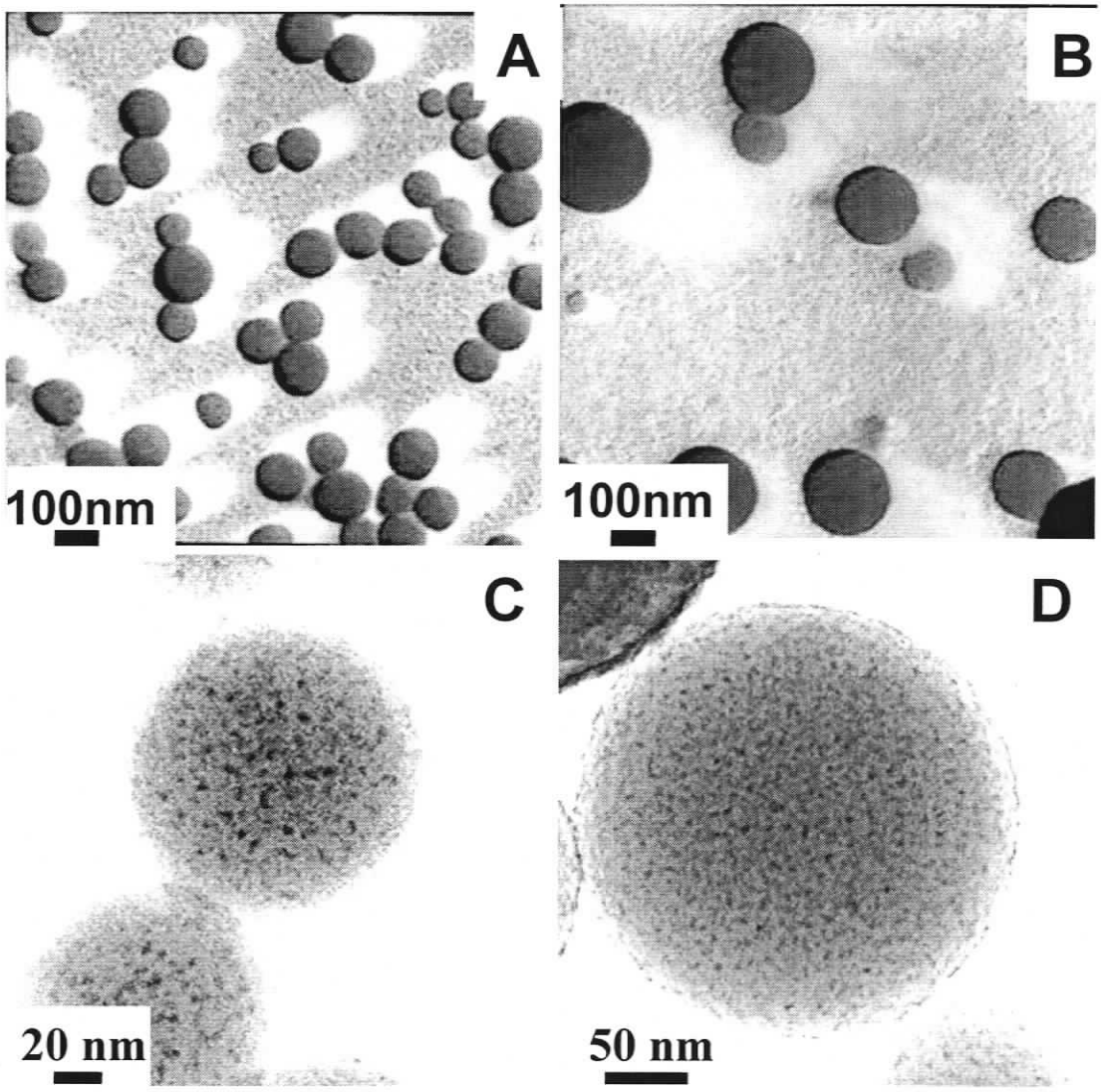

Figure 4.2. TEM images of colloids obtained from self-assembly of blends of PS-CdS2 and PS(665)-*b*-PAA(68) (f = 0.5, $rate_{water}$ = 1.2 wt% / min) for LCM2 and LCM3: A) Shadowed image of LCM2, B) Shadowed image of LCM3, C) Unshadowed image of LCM2, D) Unshadowed image of LCM3.

shadowing (Figure 4.2C, D) reveal their hierarchical internal structure as suggested in Scheme 4.3. DLS of both particle samples at pH = 6 (following dialysis against deionized water) was used in combination with TEM sizes to determine the thickness of the PAA brush layer, which was ~17 nm for both particles, suggesting highly extended negatively-charged PAA chains. Table 4.2 summaries structural aspects for both LCM particle sizes prepared. We stress that the LCM particles become kinetically frozen above a certain water content, so they will not undergo structural rearrangement (changes in d_c, n_{CdS}) in the subsequent SA3 step described below; this kinetic freezing is simple a result of the T_g of PS (~ 100 °C) effecting a glassy LCM matrix with no mobility at room temperature. We also note that the thickness of the PAA brush is a conformational parameter that will change in different solvent environments, and is presented in Table 4.2 only for aqueous pH = 6 media. The d_h values in pH = 4 buffer could not be obtained as the LCMs aggregated upon dilution at this pH, suggesting a lack of sufficient repulsive interactions to stabilize the LCM colloid.

Table 4.2: Structural Characteristics of LCM2 and LCM3.

LCM Sample	d_c[a] (nm)	$\sigma(d_c)$[b] (nm)	$n_{PS\text{-}CdS}$[c]	d_h[d] (nm)	t_{PAA}[e] (nm)
LCM2	109 ± 2	18	120 ± 11	143 ± 1	17 ± 2
LCM3	209 ± 10	63	840 ± 160	243 ± 9	17 ± 13

a. **average LCM core diameter (TEM)**
b. **standard deviation of size distribution of LCM core diameters (TEM)**
c. **average number of PS-CdS2 particles per LCM particle (TEM)**
d. **z-average hydrodynamic diameter of LCM particles in water at pH = 6 (DLS)**
e. **thickness of PAA layer surrounding LCM particles in water at pH = 6 (DLS, TEM)**

4.3.3. *Preparation and Characterization of Tertiary Large Compound Micelle Assemblies (SA3 Self-Assembly).*

The third and final step in the multi-step route to hierarchical structures was tertiary self-assembly of the two selected LCM samples, LCM2 and LCM3. This was carried out by the slow evaporation of 10 wt% aqueous dispersions of each sample on a clean glass substrate. Evaporation of the deposited sessile droplets of colloid solution on glass will effect self-assembly of LCM spheres on the substrate via a combination of forces. In the center of the water drop, gravitational sedimentation of LCMs is expected to play a role, resulting in self-assembly at the substrate due to the local increase in the volume fraction of spheres. Convective flow within an evaporating sessile drop from the top center to the contact line is known to occur as a result of evaporation being faster at the contact line, due to faster diffusion of water vapour away from the air/liquid interface[34]. These flow lines should push LCMs toward the contact line, with shear-mediated self-assembly then occurring at the evaporating contact line as a result of capillary forces between particles; this is similar to "coffee ring" formation from an evaporating coffee drop on a kitchen counter. Both mechanisms of self-assembly within the droplet (sedimentation and convection) will be mediated by the steric and electrostatic repulsive interactions between spheres within the colloid, with electrostatic repulsion acting on larger length scales than steric (hard-sphere) repulsion. Although the extended PAA brush layer will play a critical role in the electrostatic repulsive interactions between LCMs as self-assembly occurs, this layer will collapse on the surface of the LCM sphere in the final stages of water evaporation (which will occur at different stages in the center and at the edges of the drop). Due to this collapsed and water-swollen PAA

layer, the LCM particles are expected to become "sticky": this factor should provide structural integrity to the final hierarchical assemblies, but will also induce strong short-range attractive interactions between LCMs which could trap assemblies in disordered non-close packed states. Another more basic challenge to obtaining long-range order via LCM self-assembly is the inherent polydispersity of the average sizes of the hard PS cores (Table 4.2).

For the LCM2 sample, a variety of conditions for SA2 self-assembly were attempted. One variable we adjusted was the pH of the initial deposited colloid (which was either pH = 6 or pH = 4), with stronger long-range repulsive interactions expected at pH = 6, due to the charging of PAA blocks as suggested by DLS results described earlier. As well, we used two methods to concentrate the colloids before deposition, one involving evaporation to dryness and re-suspension of the colloid (designated "dried"), and another in which the colloid was concentrated directly to 10 wt% without drying (designated "non-dried"). Figure 4.3A shows SEM images of tertiary assemblies of LCM2 deposited from pH = 6 without initial drying of the colloid (LCM2, pH6, non-dried). It is apparent from the image that the particle polydispersity is large, with a combination a large and small particles preventing order over any range. Figure 4.3B shows SEM images of tertiary assemblies of LCM2 deposited from pH = 4 with initial drying of the colloid (LCM2, pH4, dried). This image demonstrates that with the initial drying step, the particle distribution becomes much less polydisperse, presumably since larger particles in the distribution do not become re-suspended after drying. However, with pH = 4 deposition, no ordering of particles is observed despite the lower

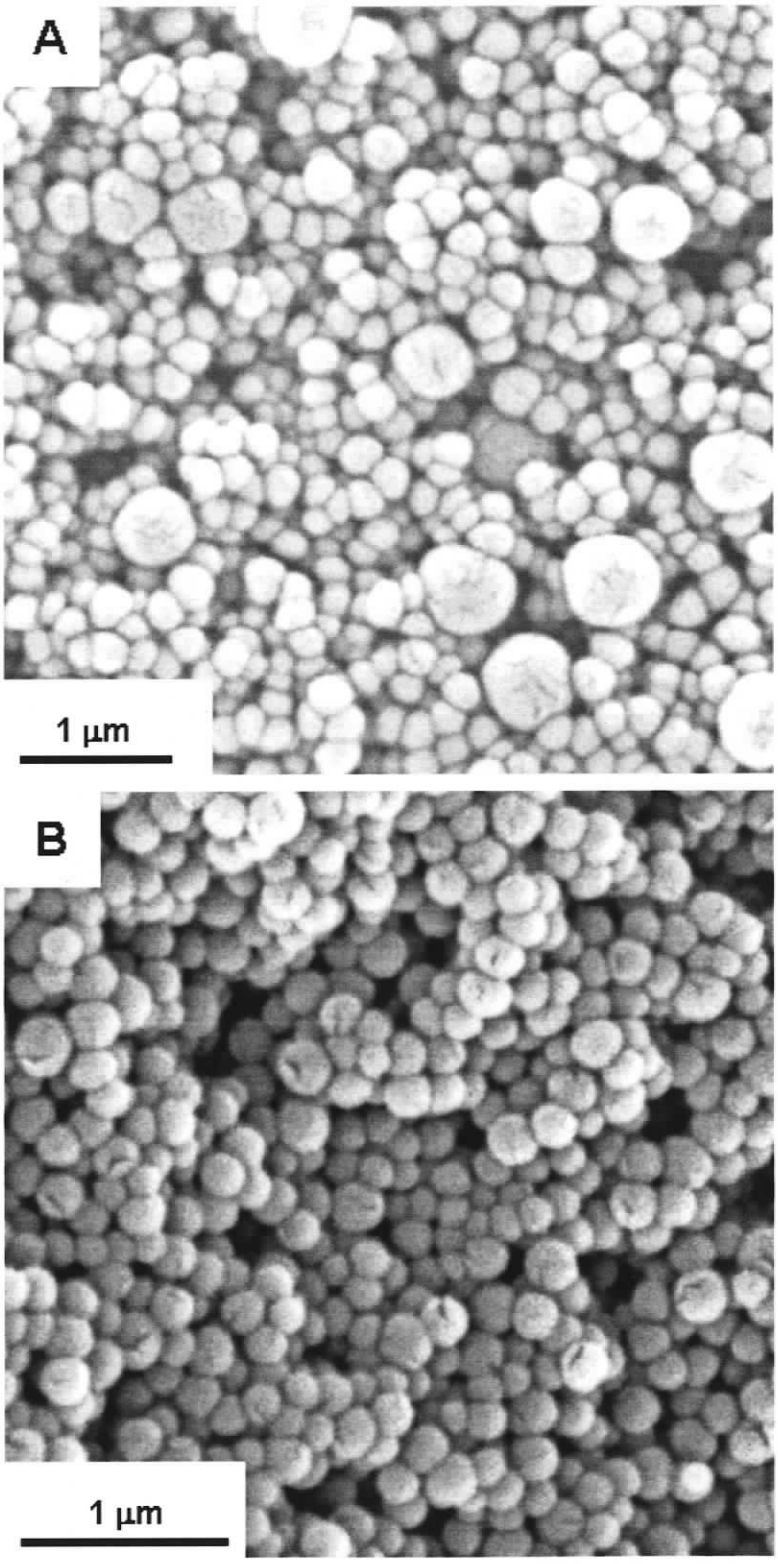

Figure 4.3. SEM images of tertiary assemblies of LCM2. A) pH = 6 (non-dried), B) pH = 4 (dried).

polydispersity; from the image, the particles appear to resist close-packing due to sticky interactions between spheres, which we attribute to a decrease in repulsive interactions at lower pH. Due to the factors discussed above, we did not observe ordered close-packing of LCMs under the conditions pH = 6, non-dried (Figure 4.3A) and pH = 4, dried (Figure 4.3B) in any regions of the deposited films.

We found that the best conditions to obtain close-packed tertiary assemblies with some long-range order for the LCM2 sample was pH = 6, with initial drying, in which case the polydispersity lowering effect was obtained and repulsive electrostatic interactions between particles were present in the evaporating colloid. In the resulting films, several regions were highly disordered, and resembled the films (LCM2, pH = 4, dried) shown in Figure 4.3B. However, we found that some regions of these films (LCM2, pH = 6, dried), in particular the film edges where lateral convective shear forces were present during self-assembly, showed close packing extending over several microns, with some hexagonal order observed within the layers (Figure 4.4). Figure 4.4D shows a side view in a region of the film where long-range order is observed in the top layer, illustrating that despite order and close-packing in two dimensions, we could not confirm that the crystallinity extended in three dimensions, although we note that defects caused by the crack in the film that was used to image the side of the lattice may obscure 3D order inside the crystal. The measured lattice periodicity (center-to-center distance between component spheres) is ~100 nm and is in reasonable agreement with the core particle sizes of LCM2 from the secondary self-assembly step (109 ± 2 nm) due to the close-packing of spheres within the tertiary assembly. We note that the average particle sizes by SEM will be somewhat affected by two factors not present during TEM imaging

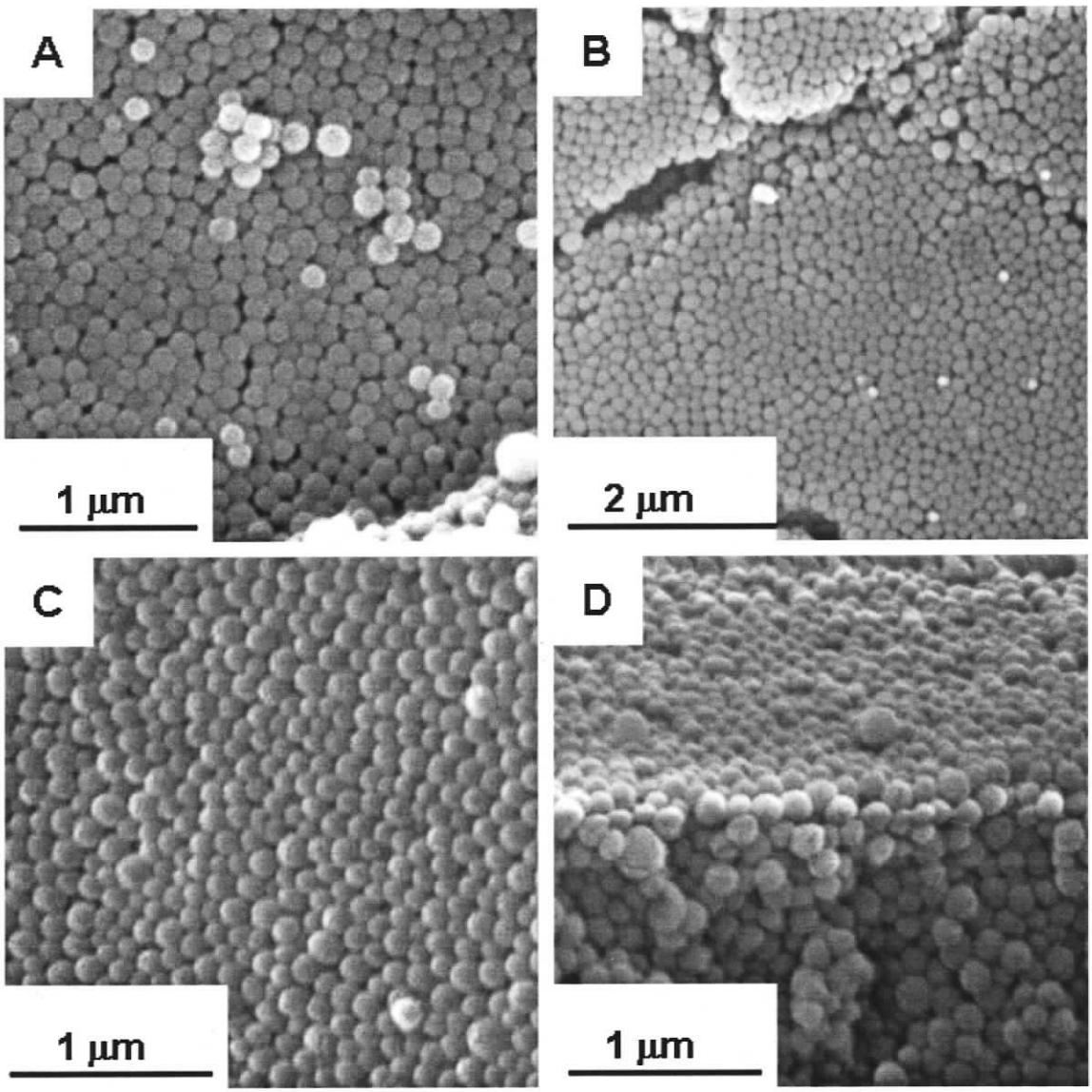

Figure 4.4. SEM images of 3D arrays of LCM2 obtained from SA3 self-assembly under conditions of: pH = 6 (dried): A, B and C) top view; and D) side view.

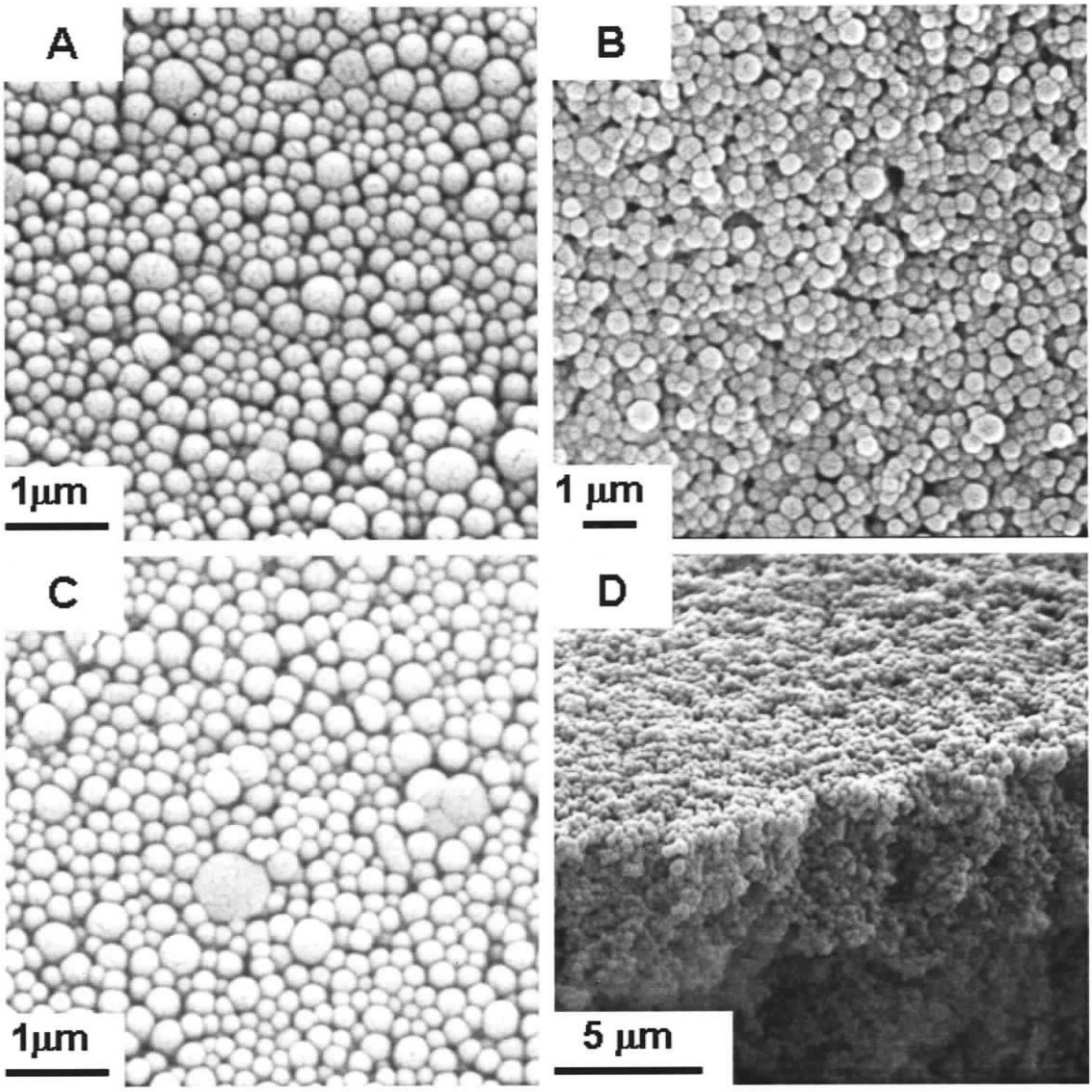

Figure 4.5. SEM images of LCM3 obtained from SA3 self-assembly from blends of PS(665)-*b*-PAA(68) and PS-CdS2, pH 6 (dried): A, B and C) top view; and D) side view.

of the original LCM2 colloid: 1) the size-selection step (drying), which will decrease average particle sizes in the assemblies relative to the original LCM2 colloid imaged by TEM and 2) the gold coating of the assemblies, which will increase the apparent particle sizes. Tertiary assemblies were also obtained for the larger LCM3 colloids (Figure 4.5), although even under optimized conditions (pH = 6, dried) no long-range order was observed in the resulting films, due to the much greater inherent size polydispersity in this sample (Table 2).

This work therefore demonstrates the feasibility of tertiary assembly of LCM colloids by water evaporation, with some long-range order achieved under conditions of optimized particle polydispersity and repulsive interactions. We note that the resulting tertiary structures are highly hierarchical, with each LCM sphere within the close-packed array possessing a complex internal structure from the assembly of PS-CdS2 particles which are themselves structurally complex; a combination of length scales is therefore present in the final assemblies, ranging from the size (~4 nm) and interparticle spacing (~12 nm) of the individual CdS nanoparticles within each sphere, to the size of the spheres (~100 nm) which determines the periodicity of the array, to the size of semi-crystalline regions of the tertiary structure, extending in some cases over several microns. We are currently pursuing several strategies to further improve the ordering of LCM spheres, including vertical deposition via a receding contact line, and application of external shear forces during self-assembly. We also note that size polydispersity of LCMs could be further improved, either kinetically at the LCM2 self-assembly step, or by further size-selection procedures (e.g. centrifugation or sedimentation).

4.3.4. *Characterization of CdS Quantum Dot Photoluminescence After Each Self-Assembly Step*

Along with the fundamental issue of controlling structure on a combination of length scales within hierarchical composite materials, our main interest in the present multi-step self assembly route is the design of composite photonic structures in which light emission from nanoparticles dispersed within the array is coupled to photonic modes of the periodic crystal. This type of structure has a number of potential applications ranging from low-threshold lasers to photonic switches, and requires a photonic band gap or stop band due to diffraction within the mesoscale crystal of spheres to spectrally overlap with emission from the quantum dots inside the spheres. We note that our strategy demonstrates the possibility of independent tuning of several structural features, including nanoparticle size, spacing, and periodicity of the array of spheres, which should allow this overlap to be controlled and optimized. The stop band of a photonic crystal will depend on both the periodicity of the array and the average refractive index according to the Bragg equation:

$$m\lambda_{min} = 2nd_{hkl}\sin\theta \qquad (4.1)$$

where m is order of the diffraction, λ_{min} is the wavelength of the stop band, n is the mean refractive index, d_{hkl} is the interplanar spacing along the [hkl] direction and θ is the angle between the incident light and the normal to the (hkl) planes[32]. From this equation, the expected stop band for $\theta = 90°$ from arrays of LCM2 and LCM3, with particle diameters 109 nm and 209 nm, are 305 nm and 585 nm respectively, using a mean refractive index

for the array of n = 1.4. The mean refractive index was calculated from the refractive indices of PS (n = 1.54) and air (n = 1.00), considering the volume fraction of PS within a closest-packed structure (0.74).

Unfortunately, we were not able to observe a stop band in preliminary UV-Vis transmission experiments of our tertiary arrays, due either to large diffuse light scattering in the thicker films investigated (LCM3), or to insufficient scattering from the thinner films (LCM2). In the thicker films (from the more polydisperse LCM3 sample) diffuse scattering is related to the lack of order in the LCM assemblies, as observed in the SEM images of Figure 4.5. Continued work on improved ordering in LCM tertiary assemblies will also involve further attempts to obtain and characterize a photonic stop band within these structures, and then to modify various length scales to achieve coupling between photoluminescence and the stop band.

Critical to achieving control of the collective optical properties via control of the various length scales of nanoparticle organization is the assumption that a constant nanoparticle size and surface environment is maintained at each stage of self-assembly. In our system, the nanoparticles are well protected inside a stable block ionomer micelle during the SA2 and SA3 self-assembly steps, with the micelle serving as a "Trojan horse" which allows the nanoparticle to be "carried" into different states of organization while maintaining a constant and protecting local environment. To test this idea, we characterized the photoluminescence of the CdS nanoparticles after each stage of self-assembly (SA1, SA2 and SA3) for both the LCM2 and LCM3 routes. Figure 4.6 and 4.7

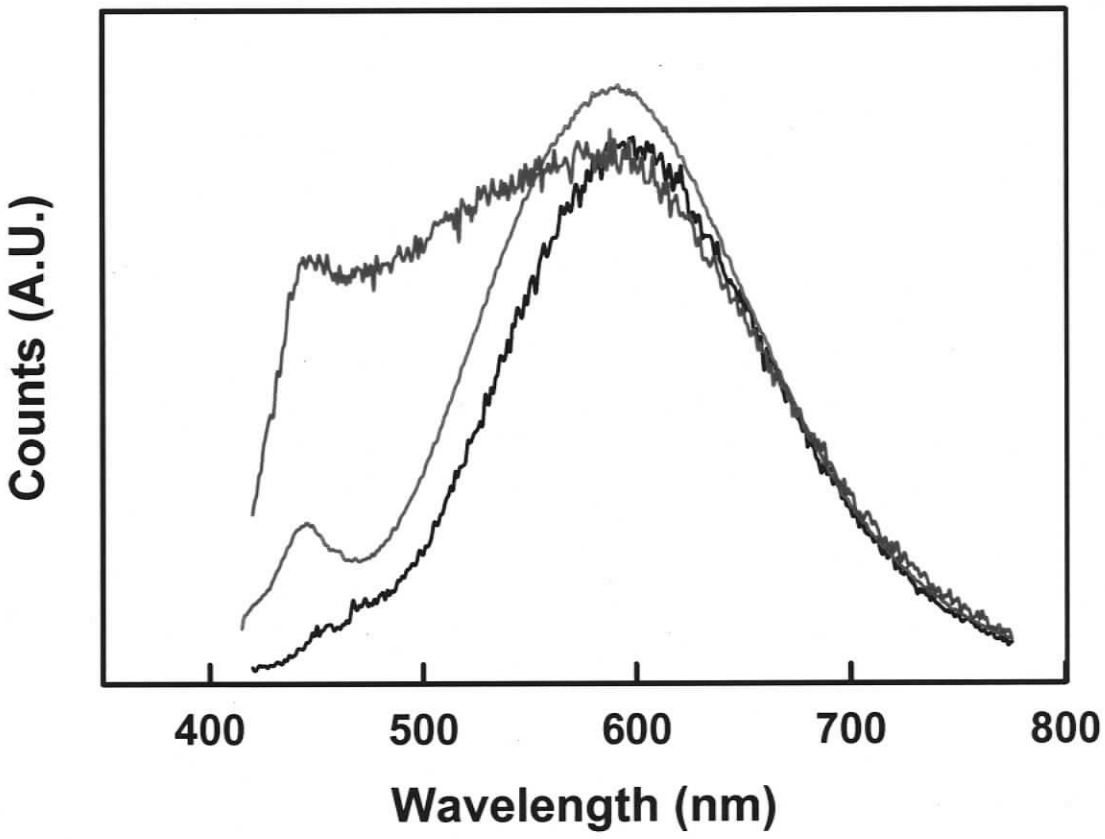

Figure 4.6. Photoluminescence of: PS-CdS2 (———), LCMs in water, LCM2 (———), and tertiary assemblies of LCMs on glass substrates, LCM2 (———). PS-CdS2 is dissolved in spectroscopic grade toluene, LCMs are dispersed in aqueous solvent, and the films have the water evaporated. The spectra are taken at λ_{ex} = 400 nm, and in each case the solvent was subtracted and recorded at 1 nm spectra resolution and a 425 nm filter.

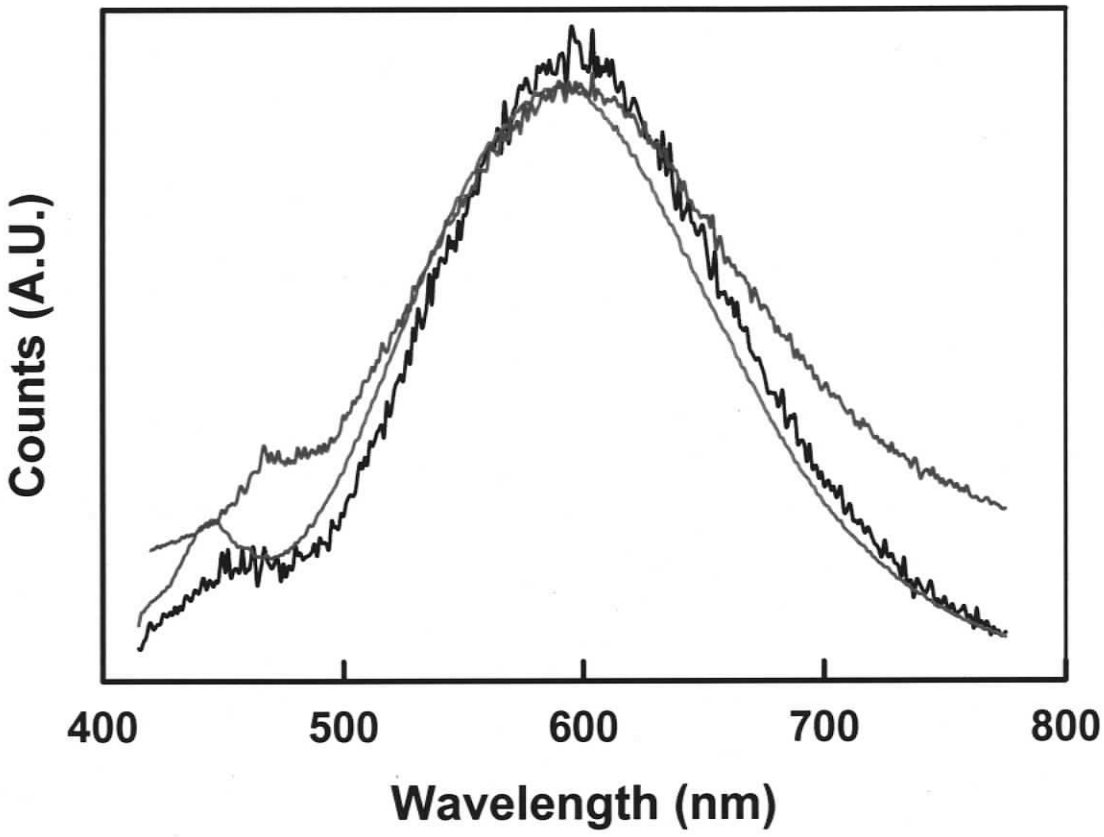

Figure 4.7. Photoluminescence of: PS-CdS2 (———), LCMs in water, LCM3 (———), and tertiary assemblies of LCMs on glass substrates, LCM3 (———). PS-CdS2 is dissolved in spectroscopic grade toluene, LCMs are dispersed in aqueous solvent, and the films have the water evaporated. The spectra are taken at λ_{ex} = 400 nm, and in each case the solvent was subtracted and recorded at 1 nm spectra resolution and a 425 nm filter.

show the photoluminescence of 1) the PS-CdS2 nanoparticles dispersed in toluene (red spectrum), 2) the LCMs in water following SA2 self-assembly and dialysis (black spectrum) and 3) the tertiary assemblies of LCMs on glass substrates (blue spectrum), for the LCM2 and LCM3 cases, respectively. In both cases, all normalized spectra show a very similar peak position characteristic of broad CdS trap-state emission, suggesting that the nanoparticles are protected from agglomeration, ripening, or local surface effects throughout the multi-step process. However, we do note a very slight red-shift in the broad emission peak position in both cases (Figure 4.6 and Figure 4.7) following SA2 self-assembly, with the peak maxima in the black and blue spectra being ~ 5 nm shifted relative to the peak maxima in the red spectra; this is attributed the dipole-dipole coupling due to the proximity of CdS nanoparticles (~12 nm) within the LCMs. The observed slight broadening of the emission peak to either the blue (LCM2, Figure 4.6) or red (LCM3, Figure 4.7) spectral region following tertiary self-assembly (blue spectra) may be due to coupling to photonic modes within the periodic array or to scattering from the air-film or film-glass interfaces, although no conclusions can be drawn without further study. We also note that the position of the weak band-edge emission peak (~450 nm) is similar in all stages of self-assembly for the LCM2 route (Figure 4.6), though it is attenuated in the LCM colloid (Figure 4.6, black spectrum) due to light scattering between the particles and the aqueous medium. For the LCM3 route (Figure 4.7) the position of the band-edge peak is similar for the dispersed PS-CdS2 nanoparticles and the LCM colloid (red and black spectra), but appears to be red-shifted in the tertiary assembly (blue spectrum), although this may be an artifact due to larger scattering of light in the blue region of the spectrum.

4.3.5. Conclusions

In this chapter, it was shown that tertiary assembly of LCMs could be achieved by slow evaporation of water, resulting in complex hierarchical structures with multiple length scales which were characterized following successive self-assembly steps. The close-packed ordering of LCMs in tertiary assemblies was optimized under conditions of lower particle polydispersity and long-range electrostatic repulsive interactions between LCM spheres (e.g. at higher pH). The photoluminescence of CdS was characterized following each self-assembly step and suggested that CdS nanoparticles were well-protected within the PS-CdS2 particles during the SA2 and SA3 steps. Possible dipole-dipole coupling between nanoparticles was detected following SA2 self-assembly, via an observed slight red-shift in the trap state emission peak.

References

1. Blomberg, E.; Poptoshev, E.; Claesson, P. M.; Caruso, F. *Langmuir* **2004,** 20, 5432-5438.

2. Boal, A. K.; Gray, M.; Ilhan, F.; Clavier, G. M.; Kapitzky, L.; Rotello, V. M. *Tetrahedron* **2002,** 58, 765-770.

3. Boal, A. K.; Ilhan, F.; DeRouchey, J. E.; Thurn-Albrecht, T.; Russell, T. P.; Rotello, V. M. *Nature* **2000,** 404, 746-748.

4. Caruso, F.; Caruso, R., A.; Mohwald, H. *Science* **1998,** 282, 1111-1114.

5. Caruso, F.; Mohwald, H. *Langmuir* **1999,** 15, 8276-8281.

6. Drechsler, U.; Thibault, R. J.; Rotello, V. M. *Macromolecules* **2002,** 35, 9621-9623.

7. Kalinina, O.; Kumacheva, E. *Macromolecules* **1999,** 32, 4122-4129.

8. Kalinina, O.; Kumacheva, E. *Macromolecules* **2002,** 35, 3675-3680.

9. Kalinina, O.; Kumacheva, E. *Chem. Mater.* **2001,** 13, 35-38.

10. Kitaev, V.; Kumacheva, E. *Langmuir* **1998,** 14, 5568-5572.

11. Kumacheva, E.; Golding, R. K.; Allard, M.; Sargent, E. H. *Adv. Mater.* **2002,** 14, (3), 221-224.

12. Kumacheva, E.; Kalinina, O.; Lilge, L. *Adv. Mater.* **1999,** 1, (3), 231-234.

13. Kumacheva, E.; Klein, J.; Pincus, P.; Fetters, L. J. *Macromolecules* **1993,** 26, 6477-6482.

14. Kumaraswamy, G.; Dibaj, A. M.; Caruso, F. *Langmuir* **2002,** 18, 4150-4154.

15. Nie, T.; Zhao, Y.; Xie, Z.; Wu, C. *Macromolecules* **2003,** 36, 8825-8829.

16. Nie, Z.; Xu, S.; Seo, M.; Lewis, P. C.; Kumacheva, E. *J. Am. Chem. Soc.* **2005,** 127, 8058-8063.

17. Niemz, A.; Rotello, V. M. *Acc. Chem. Res.* **1999,** 32, 44-52.

18. Salgeirino-Maceira, V.; Caruso, F.; Liz-Marzan, L. M. *J. Phys. Chem. B* **2003,** 107, 10990-10994.

19. Schoeler, B.; Sharpe, S.; Hatton, T. A.; Caruso, F. *Langmuir* **2004,** 20, 2730-2738.

20. Schuetz, P.; Caruso, F. *Chem. Mater.* **2004,** 16, 3066-3073.

21. Shenhar, R.; Norsten, T. B.; Rotello, V. M. *Adv. Mater.* **2005,** 17, (6), 657-669.

22. Shenhar, R.; Rotello, V. M. *Acc. Chem. Res.* **2003,** 36, 549-561.

23. Sohn, D.; Kitaev, V.; Kumacheva, E. *Langmuir* **1999,** 15, 1698-1702.

24. Wang, D.; Rogach, A. L.; Caruso, F. *Chem. Mater.* **2003,** 15, 2724-2729.

25. Yu, A.; Meiser, F.; Cassagneau, T.; Caruso, F. *Nano Lett.* **2004,** 4, (1), 177-181.

26. Yu, K.; Zhang, L.; Eisenberg, A. *Langmuir* **1996,** 12, 5980-5984.

27. Yu, Y.; Zhang, L.; Eisenberg, A. *Macromolecules* **1998,** 31, 1144-1154.

28. Zhang, J.; Coombs, N.; Kumacheva, E. *J. Am. Chem. Soc.* **2002,** 124, 14512-14513.

29. Zhang, L.; Barlow, R. J.; Eisenberg, A. *Macromolecules* **1995,** 28, 6055-6066.

30. Murray, C. B.; Keagan, C. R.; Bawendi, M. G. *Annu. Rev. Mater. Sci.* **2000,** 30, 545-610.

31. Xia, Y.; Gates, B.; Li, Z.-Y. *Adv. Mater.* **2001,** 13, 409-413.

32. Xia, Y.; Gates, B.; Ying, Y.; Lu, Y. *Adv. Mater.* **2000,** 12, (10), 693-713.

33. Wang, C.-W.; Moffitt, M. *Langmuir* **2004,** 20, 11784-11796.

34. Deegan, Robert D.; Bakajin, Olgica; Dupont, Todd F.; Huber Greb; Nagel, S. R.; Witten, T. A. *Nature* **1997,** 389, 827-829.